The Pennsylvania State University

The Graduate School

College of Engineering

COMPOSITION OF THE ENDOTHELIAL GLYCOCALYX AND ITS EFFECT ON TRANSVASCULAR EXCHANGE OF SMALL SOLUTES

A Dissertation in

Bioengineering

by

Lujia Gao

Submitted in Partial Fulfillment
of the Requirements
for the Degree of

Doctor of Philosophy

August 2010

The dissertation of Lujia Gao was reviewed and approved* by the following:

Herbert H Lipowsky
Professor of Bioengineering
Head of the Department of Bioengineering
Dissertation Advisor
Chair of Committee

Cheng Dong
Professor of Bioengineering

Peter J Butler
Associate Professor of Bioengineering

Andrew Zydney
Walter L. Robb Chair and Professor of Chemical Engineering

*Signatures are on file in the Graduate School

ABSTRACT

The endothelial cell (EC) of the circulatory system is coated with a layer of macromolecules, composed of proteins and polysaccharides. It has been suggested that the endothelial glycocalyx in postcapillary venules contributes to the control of solute permeability, anti-inflammatory and anti-thrombotic properties of the endothelium. These properties of the glycocalyx can be attributed to the glycosaminoglycans (GAGs), which is the major constituent of the endothelial glycocalyx. To elucidate the contribution of individual GAG molecules to the structural and biological functions of the glycocalyx, techniques of intravital microscopy were used to study its function in the mesenteric microcirculation of the rat.

A new technique was developed to quantitatively measure the hydraulic properties of the glycocalyx layer to small solutes in normal and inflamed states. Using a modified indicator dilution technique under control and inflammatory state induced by topically application of 10^{-7} M formyl-met-leu-phe (fMLP), the transient dispersion of a bolus of the small fluorescent molecule, fluorescein isothiocyanate (FITC), or FITC conjugated with 70 kDa dextran (FITC-Dextran70) through post-capillary venules in the mesenteric circulation was recorded and analyzed offline. The dispersion of the solute at radial positions normal to the microvessel wall was represented by a virtual transit time (VTT(r)) calculated from the first moment of the intensity-time curve of the bolus. The slope of VTT ($\Delta VTT/\Delta r$) in the near wall region was affected by the hydraulic hindrance of the glycocalyx layer. Numerical simulations of a FITC bolus flowing in a straight tube were performed and showed that the $\Delta VTT/\Delta r$ was principally determined by the

permeability, thickness and effective diffusion coefficient of the solute in the glycocalyx layer.

The removal of GAGs was quantitated by labeling with the plant lectin BS-1 conjugated with Alexa Fluor 488. Enzymatic removal was compared to the shedding of glycans induced by stimulating the endothelium by 10^{-7} M fMLP. Thickness of the glycocalyx was assessed by infiltration of the glycocalyx with circulating FITC-Dx70 and measuring the distance from the dye front to the surface of the EC, which averaged 463 nm under control conditions. Reductions in thickness were 43.3%, 34.1% and 26.1% following heparinase, chondroitinase and hyaluronidase, respectively, and 89.7% with a mixture of all three enzymes. Diffusion coefficients of FITC in the glycocalyx were determined by comparison of measured transients in radial intensity of a bolus of FITC with that of a 1-D diffusion model. Values of D were obtained corresponding to the thickness of the layer demarcated by Dx70 (D_{Dx70}), and a smaller sublayer 173 nm above the EC surface (D_{173}). The magnitude of D_{Dx70} was twice that of D_{173} suggesting that the glycocalyx is more compact near the EC surface. Chondroitinase and hyaluronidase significantly increased both D_{Dx70} and D_{173}. However, heparinase decreased D_{Dx70}, and did not change the D_{173}. These observations suggest that the three GAGs are not evenly distributed throughout the glycocalyx and that they each contribute to permeability of the glycocalyx to a differing extent. The fMLP-induced shedding caused a reduction in the barrier thickness and decreased the whole layer permeability similar in magnitude to that of heparinase. This behavior suggests that the removal of heparan sulfate may cause a collapse of the glycocalyx which counters decreases in thickness to maintain a constant resistance to filtration.

TABLE OF CONTENTS

LIST OF FIGURES

LIST OF TABLES

ACKNOWLEDGEMENTS

I would like to give my deepest appreciations to Dr. Herbert H. Lipowsky for his guidance in maturing my skills and mind as a better problem seeker and solver. His patience and instructions were most appreciated during difficult experiments. I am very grateful for the opportunity and commitment that Dr. Lipowsky has provided for me to do what I enjoy and fulfill my goals.

I would like to thank my committee members: Dr. Cheng Dong, Dr. Peter Buter, and Dr. Andrew Zydney for their time and input in my dissertation. I would also like to thank Anne Lescanic for her excellent technical expertise, friendship and priceless spiritual support all through my life as a Ph.D. student. You made State College my second hometown. My gratitude should also be extended to Chonghaw, Eun-Joo and all my fellow graduate students who have made bioengineering a family.

Finally, I would like to dedicate this dissertation to my parents, especially my mother for her unconditional love, support and encouragement. None of this would be possible without you. This dissertation is also for my wife, Xin, for her love, trust and the most beautiful son in the world. Lastly, I would thank all my friends at Penn State, who have made my past seven years so enjoyable, exciting and memorable.

Chapter 1

Introduction and Background

Endothelial cells are endowed with a layer of negatively charged protein-polysaccharide complex, named endothelial glycocalyx, or the endothelial surface layer. The endothelial glycocalyx was first observed by Luft in 1966 using electron microscopy following ruthenium red staining (Luft, 1966). But studies on this glycan-rich coating on the endothelial cell did not receive much attention until 20 years later, when its importance as a barrier to transport was identified in the cornea (Ausprunk et al., 1981a; Ausprunk et al., 1981b; Hornung and Wollensak, 1979), lymph nodes (Anderson and Anderson, 1976), intestines (Benjawatanapon et al., 1982), kidney (Monnens, 1982), lung (Romanova and Filippenko, 1975; Ryan et al., 1985), liver (Ghitescu and Fixman, 1984) and the general blood circulation system (Ryan and Ryan, 1984; Schneeberger, 1988). The increasing interest in the endothelial glycocalyx in academic research in the past decade has suggested strong ties between this layer and homeostasis of the cardiovascular system, as summarized by several reviews (Broekhuizen et al., 2009; Jacob et al., 2009; Nieuwdorp et al., 2008; Pries et al., 2000; Van Teeffelen et al., 2007).

1.1 Review of the Molecular Composition of the Endothelial Glycocalyx

The endothelial glycocalyx contains large amount of carbohydrates in association with other heterogeneous molecules. The principal carbohydrates are the glycosaminoglycans (GAGs) that give the layer its characteristic negative charges. The glycocalyx layer is anchored to the luminal surface of the endothelial cell through membrane associated GAG-carrying proteins that comprise proteoglycans (PGs) and glycoproteins. Usually the protein core of PGs and glycoproteins carries multiple GAG side chains, together forming the molecular and structural backbone for other molecules to be incorporated. Together they form the glycocalyx layer. Soluble molecules of both endothelial cell- and plasma-origin are also constitutive components of the glycocalyx. Particularly, presence of the blood plasma proteins seems necessary for maintenance of the glycocalyx layer. Studies have shown the importance of these soluble proteins to the biological function and structural integrity of the glycocalyx layer, both in vivo and in vitro (Adamson and Clough, 1992; Potter and Damiano, 2008; Schneeberger, 1988).

Proteoglycans and glycoproteins are two most prominent carbohydrates carriers of the endothelial glycocalyx layer. Proteoglycans are the basic structural support for the glycocalyx, which may be due to the fact taht PGs carry multiple long unbranched GAG chains on their core proteins. Proteoglycans can exist in either membrane-bound or soluble forms. Polypeptide backbones of membrane-bound PGs associate with the endothelial cell luminal membrane through their transmembrane domains or via glycophosphatidylinositol (GPI) linker. The molecular switch G protein is suggested to be associated with these transmembrane proteins, enabling the glycocalyx function as

part of the intercellular signaling cascade (Fitzgerald et al., 2000). The association of PGs with cytoskeleton of the endothelial cell has also been reported, which is especially important for the shear sensing capability of the glycocalyx. The two most important PGs of the endothelial glycocalyx are syndecans and glypicans.

The syndecan family belongs to the type I class of transmembrane proteins, and consists of an N-terminal cytoplasmic tail, a transmembrane domain, an ectodomain that contains polysaccharide attachment site, and a C-terminal domain (Carey, 1997). The syndecan family contains four members, syndecan-1, -2, -3 and -4, which all carry three to five GAG chains. Heparan sulfate (HS) GAG chains are universally carried by syndecans. Syndecan-1 and -4 are also capable of carrying chondroitin sulfate (CS) GAG chains. Ser-Gly is shown to be the conserved repeat on the protein core for GAG attachment, but not on all Ser-Gly, which could be affected by the folding of the newly synthesized core protein. These Ser-Gly repeats exist in clusters. Syndecan-1 and -3 each has two clusters, while syndecan-2 and -4 each only have one. The CS chains elongation can only be in the attachment cluster close to the plasma membrane on the ectodomain of the core protein (Carey, 1997).

The glypican family contains six members, Glypican-1 through -6. Glypicans lack the transmembrane domain and are anchored to the endothelial cell membrane via a GPI-linker (Tumova et al., 2000). Glypicans can be in inactive forms and active forms. In the inactive form, glypicans carry exclusive HS side chains, attached between the central domain and the C-terminal GPI-anchor on the protein core (Filmus et al., 2008; Fransson, 2003). Capability of glypicans to carry CS-GAG chains has been shown in vitro. Switch between HS-bearing or CS-bearing glypicans seems be the globular domain at the N-

terminal of the core protein (Chen and Lander, 2001). Glypicans are involved in signaling regulations of Wnts, Hedgehogs, fibroblast growth factors, and morphogenetic proteins (Filmus et al., 2008).

Besides PGs, glycoproteins are another family of important cell surface carbohydrate carriers, but differ from PGs in that their carbohydrate chains are smaller and branched. The physiological significance of the glycoproteins lies in their regulatory roles in cell-cell interaction and involvement in thrombotic/fibrolytic processes.

There are three families of cell-adhesion glycoproteins, selectins, integrins and immunoglobulin superfamily cell adhesion molecules (IgSF CAMs). Differenting from proteoglycans that carry O-linked GAG chains, these cell adhesion molecules carry N-linked oligosaccharides. Selectins can be categorized as E-, P- and L-selectin, based on their associated cells and affinity for ligands. Vascular endothelial cells express E- and P-selectin on their surface upon pro-inflammatory stimulation. During the vascular inflammatory response, selectins and ligands regulate rolling of leukocytes on the endothelial wall and to initiate the firm adhesion, which is mediated by integrins. Integrins are heterodimeric molecules composed of α- and β-subunit. CAMs are the primary ligands for intergins to regulate the cell adhesion of leukocytes and endothelial cells. Selectins are heavily decorated with N-linked oligosaccharides on their ectodomains, contributing 50% of the molecular weight for L- and E-selecin and 30% for P-selectin (Cummings and Smith, 1992; McEver, 1994). Integrins are also glycosylated with N-glycans. Additions of N-glycan to integrins control their biological funtions of being inhibitory or promotive toward cell migration. More specifically, adding N-acetylglucosamine (GlcNAc) to mannose (Man, branching end of the Man-GlcNAc-

GlcNAc-Asn linkage) via β-1,4 linkage inhibits the cell migration, but addition of GlcNAc via β-1,6 linkage will promote it (69). Common IgSF CAMs involved in the vascular cell adhesion include ICAM (Intercellular), VCAM (Vascular) and PECAM (Platelet-endothelial). Most immunoglobulin domains of IgSF CAMs have N-linked glycans. Studies have indicated these N-glycans are important in correct folding of the molecules or in recognizing their integrin receptors (Jimenez et al., 2005).

O-linked glycans GAG complexes are associated with proteoglycans which have are long unbranched polysaccharide chains and have significant structural impact on the glycocalyx layer. N-linked glycans are branched and found on the glycoproteins. They are primarily involved in receptor-ligand binding in vast varieties of biological processes. Based on the focus of these studies, detailed attentions will be paid on O-linked glycosaminoglycans.

The complexity of proteoglycans lies in the randomness and diversity of the GAG chains. GAGs of the endothelial glycocalxy can be categorized into three main forms, the heparan sulfate, chondroitin sulfate and hyaluronic acid (or hyaluronan, HA), together with dermatan sulfate, keratan sulfate and heparin. Among them, HS and CS exist in both covalently bound form and secreted or cleaved soluble form, whereas HA is exclusively soluble. The GAG chains are made of repeating disaccharides. The disaccharide unit for HS is glucuronic acid or iduronic acid linked to N-acetylglucosamine (GlcA/IdoA-GlcNAc) via α-β1→4 linkages (Lindahl and Hook, 1978). The disaccharide repeat for CS is GluA and N-acetylgalactosamine (GluA-GalNAc) via α-β1→3 linkages (Sugahara et al., 2003). HS and CS share common linkage to the peptide bone.

HA made of disaccharide unit GlcAb β1→3GlcNAc, is different from other GAGs in two major aspects. HA is not sulfated, which makes it more inert in affinity binding than other GAGs, including HS and CS. This is the reason that HA was attempted as the scaffold for slow releasing of drugs in patients. The polymerization of HA takes place on the plasma membrane and the newly formed HA strand is extruded to the extracellular space. This makes synthesis of extra long HA chains possible. By comparison, elongations of HS and CS take place in the Golgi apparatus, which spatially limits the size of these chains. There are two known HA binding receptors in the glycocalyx. The most prominent HA receptor is cell membrane rooted glycoprotein CD44 family (Aruffo et al., 1990). Chondroitin sulfate is another HA receptor (Nijenhuis et al., 2009).

The dependence of the glycocalyx layer on the soluble molecules, especially plasma-borne, has been shown and these molecules are being identified continuously. Early study using EM image by Adamson and Clough found the separation between the surface of the endothelial cell and ferritin, which labels the glycocalyx, is larger when the plasma is present (Adamson and Clough, 1992). In cultured endothelial cells, where they are deprived of complete blood serum, thickness of the glycocalyx layer was found lost by nearly 90%(Chappell et al., 2009; Potter and Damiano, 2008). Circulating soluble GAGs was found to restore the barrier function of the glycocalyx (Gouverneur et al., 2008; Gouverneur et al., 2006). Albumin is likely to be part of the glycocalyx, shown by Jacob et al. in its ability to stimulate shear-induced vasodilation compared with hydroxylethyl starch (Jacob et al., 2007). The list of plasmic components of the glycocalyx is kept growing.

1.2 Structural Review of the Endothelial Glycocalyx

Dimensions of the endothelial glycocalyx layer has been well investigated both in vivo and in culture endothelial cells. The measured thickness seems heavily dependent on the technique being used and the in situ environment. Earlier measurements primarily used direct EM observation. EM observed thickness of the glycocalyx is on the range of 50-200 nm. For example, Luft (known as the discoverer of the glycocalyx) using ruthenium red staining and Rostgaard using less damaging perfusion-fixation for EM preparation measured the thickness of the capillary glycocalyx on the order of 100 nm (Luft, 1966; Rostgaard and Qvortrup, 1997). Squire utilized rapid frozen tissue preparation and measured 100-200 nm for the capillary glycocalyx (Squire et al., 2001). However, it's well acknowledged the tissue fixation required by EM imaging induces damage to the glycocalyx structure. Indirect measurement of the layer without fixation was then developed. Thicknesses measured by these techniques are generally higher. For instance, Duling used a dye exclusion technique to estimate the thickness of the capillary glycocalyx layer on the order of 400 nm (Vink and Duling, 2000). Using micro-PIV technique, extrapolation of velocity profiles by Smith et al. revealed a thickness of 330 nm (Smith et al., 2003). Variation of the glycocalyx thickness in various vessels were estimated by the exclusion thickness of FITC conjugated Dextran 70kDa (Henry and Duling, 1999). The results indicate that larger vessel usually has thicker glycocalyx layer. Arterioles and venules with 10-15 μm in diameter, the glycocalyx can extend to 500 nm.

For arterioles and venules of 7-10 μm in diameter, the measured thickness is 400 nm, and 380 nm for capillaries. Attempts to measure the endothelial surface glycocalyx were also conducted in cultured cells. Due to the difficulty in reproducing the complete physiological environment for the endothelial cell, these measurements are usually quite small. Chappell et al. found the thickness of in vivo glycocalyx ranging from 355 to 1210 nm, but tenth remained in cultured endothelial cells between 29.4 to 117.9 nm (Chappell et al., 2009). Similar finding was reported by Potter and Damiano that 520 nm glycocalyx in vivo was reduced to nearly zero in vitro (Potter and Damiano, 2008). They also found that partial restoration can be achieved in cultured cells by adding HA and CS, suggesting extensive GAG loss when the ECs were deprived of serum conditions.

The ultrastructure of the endothelial glycocalyx was firstly investigated by Squire et al. using Fourier transforms to find regular patterns in EM images of the glycocalyx. Squire et al. proposed a quasi-periodic 3D meshwork of fibers with 10-12 nm in diameter and 20 nm apart in all directions (Squire et al., 2001). This finding disputed the notion of a randomly distributed mesh structure of the glycocalyx layer and laid a foundation for later modeling studies and analysis. Based on the quasi-periodic structure, Weinbaum et al. modeled the flow inside the layer and the force exerted on the structure and its effects on the deflection of the structure (Weinbaum et al., 2003). Sugihare-Seki et al. used the same 3D mesh model to study the relative resistance to the trans-endothelial flow from the glycocalyx layer and the intercellular cleft (Sugihara-Seki et al., 2008). This structural model has also been used to investigate the solute transport through the glycocalyx. Zhang et al. thoroughly investigated effects of different parameters of the fiber matrix model to the osmotic flow and partition coefficient in the macromolecule transport

(Zhang et al., 2006). The primary goal of these models was to associate the structure of the glycocalyx to its experimentally observed biological function, mainly as a barrier that controls the trans-endothelial flux of water and plasma molecules.

Earlier EM studies showed the filaments of the glycocalyx structure, which would likely be attributed to long GAG chains (Rostgaard and Qvortrup, 1997). It is widely accepted that these long GAG chains sustains the fibrous meshwork of the endothelial glycocalyx, based on the following characteristics of the GAG chains. (i) GAG chains are long unbranched fibers. For example, the contour length of HA chain can be as long as 10 μm, with several million Daltons in MW (Laurent and Fraser, 1992). (ii) Stable cross-linkages can be formed by receptors that bind to more than one GAGs and self-associations of HA. (iii) GAGs have the ability to immobilize large amount of water molecules. One remarkable feature of GAGs is the net negative charges, provided by the carboxylic ($-COO^-$) and sulfate ($-SO_4^-$) groups on the amino sugar of the disaccharide repeat. Water molecules of up to fifty times of the weight of GAGs can be attracted by these charges. Although HA doesn't carry sulfate groups, it has been proposed the HA chains form a helical configuration by hydrogen bonds parallel to the axis (Scott and Heatley, 1999). This configuration enables HA to take up approximately 1000-time more water than non-coiled molecular chains (Laurent and Fraser, 1992). The immobilized water molecules can hydrate and sustain the fibrous meshwork thus keeping it from collapsing. Immobilized water is also vital for the barrier function of the glycocalyx by effectively increasing the constrictivity of the porous media, i.e. the diffusion of small solutes.

1.3 Review of the Biological Functions of the Endothelial Glycocalyx

Biological significance of the endothelial glycocalyx can be roughly categorized as a selective barrier and an active participant in intracellular interactions. Barrier properties of the glycocalyx layer rely on its fibrous meshwork that provides both size and charge selectivity to the diffusion of blood-borne molecules. The glycocalyx has been shown to greatly impede the uptake of albumin and LDL by the endothelial cell (Ueda et al., 2004; Van den Berg et al., 2009). The transport barrier function of the glycocalyx layer is especially important in the glomerular capillaries to retain blood-borne proteins (Singh et al., 2007). Function of the glycocalyx as the primary shear stress-sensor and mechanotransducer for the endothelial cell has been shown and modeled. Florian et al. experimentally showed that shear stress-dependent nitric oxide production by EC is completely abolished after removal of heparan sulfate (Florian et al., 2003). In vitro cultured endothelial cells are also dependent on the glycocalyx to proper migrate and proliferate (Yao et al., 2007). The glycocalyx not only senses the shear stress, but also transduce and elicit intracellular responses via the coupling between the glycocalyx and the cytoskeleton (Tarbell and Ebong, 2008; Thi et al., 2004), which is linked to the gene transcription of the vascular endothelial cell (Vartanian et al., 2010).

The glycocalyx is also at the center in most physiological processes occurring on the luminal surface of the endothelial cell. First of all, the endothelial glycocalyx protects the endothelium against proinflammatory challenges by providing binding sites for anti-inflammatory enzymes like antithrombin III (Shimada et al., 1991), tissue factor pathway inhibitor (Ho et al., 1997; Kato, 2002), extracellular superoxide dismutase (Karlsson and

Marklund, 1988) and lipoprotein lipase (Wang et al., 1992). Glycocalyx takes part in angiogenesis and wound healing process by interacting with vascular endothelial growth factor (Dougher et al., 1997; Robinson and Stringer, 2001) and fibroblast growth factor (Fromm et al., 1997). The interaction between circulating leukocytes with ECs also involves the regulation from glycocalyx (Mulivor and Lipowsky, 2002). Lastly, the glycocalyx has been shown to be the primary sensing and part of transduction for various physiological responses of EC to blood shear stress (Florian et al., 2003; Tarbell and Ebong, 2008). GAGs are at the primary providers for these binding activities.

The sensitivity of the glycocalyx to both biological and mechanical signals and elicit intracellular responses suggest it is tightly regulated by the EC and there is a dynamic balance of synthesis of components and loss into the circulation (Lipowsky, 2005). However, the fine structure and molecular composition of the glycocalyx still largely remain elusive, particularly in terms of signaling hierarchy of components of the glycocalyx as well as their changes and impacts on the biological functions. The goal of this study is to quantitatively measure three GAGs (HS, CS and HA) of the glycocalyx and their individual contribution to the barrier function of the endothelial glycocalyx layer.

Chapter 2

Methods and Techniques

The mesenteric circulation of the rat was used as the in vivo model for all studies. Post-capillary venules with 15-60 μm in diameter and red cell velocity (V_{RBC}) equal or larger than 1 mm/sec were selected for intravital microscopic visualization.

2.1 Animal Preparation

Adequate measures were taken to minimize pain or discomfort, and all experiments were conducted with international standards on animal welfare and compliant with local and national regulations. Male Wistar rats, 200-350 grams in weight, were anesthetized with pentobarbital (45 mg/kg, i.p.) or Inactin (150mg/kg, i.p.). 20 min was given to achieve desirable level of anesthetization. A tracheotomy was followed to permit spontaneous respiration. Supplemental doses of anesthetic (16.5 mg/mL) in case of pentobarbital were administrated via indwelling PE-50 polyethylene tubing in the right internal jugular vein to maintain a surgical plane of anesthesia. Arterial blood pressure was monitored through a second cannula in the right carotid artery by PE-90 polyethylene tubing that was connected to a strain-gage type pressure transducer. The body's core temperature was maintained using a heating pad controlled by a close-loop automatic controller (FHC, Bowdoinham, ME). For indicator dispersion experiments, the ileocolic artery was cannulated with PE-10 polyethylene tubing and connected to a 1mL

syringe (SGE, Australia), as seen in Fig. **1**. If necessary, blood samples were withdrawn through the carotid catheter. Delivery of certain dye and enzymes requires direct perfusion of the post-capillary venules. In this scenario, cannulation of the post-capillary venule was performed with a solution-filled micropipette. Glass micropipettes (1 mm OD, WPI, Sarasota, FL) were pulled using a pipette puller (Model 700C, David Kopf Instruments, Tujunga, CA) and double-beveled to obtain a sharply angled 2-5 μm tip opening using a pipette beveler Fig. 2 (BV-10, Sutter Instrument Co., Novato, CA). The tip region of each micropipette was filled by capillarity with heparinized (5 U/ml) normal saline and the remainder of the lumen back filled with specific solutions, depending upon the protocol. The micropipette was held in a pipette holder, which was connected to a syringe using silicon tubing. The pipette holder and silicon tubing were filled with water and the back end connected to a pressurized reservoir to enable infusion. The pipette holder was mounted on a hydraulic micro-manipulator (MMH-1, Narishige, Japan). Depending on specific protocols, a proximal feeding branch of the venule under observation was cannulated for infusion, as depicted in the schematic of the experimental protocol shown in Fig. 2. The syringe was pressurized to obtain a flow rate comparable to the pre-intubation undisturbed flow by increasing the infusion pressure such that the dividing streamline in the confluent streams was maintained at its pre-intubation position.

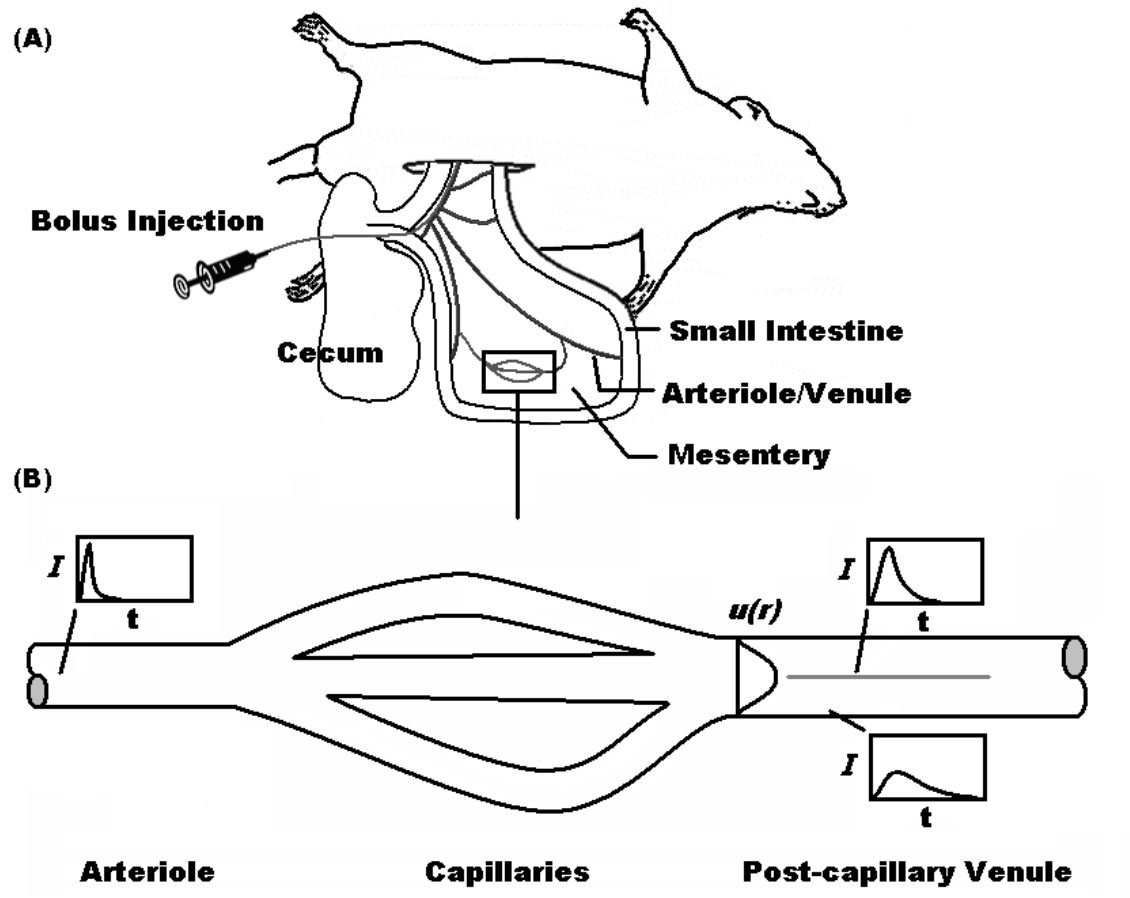

Figure 1: Schematic of indicator dispersion procedures: (a) A 20 μl bolus of fluorescent solutes (FITC or FITC-Dextran70) was injected into the ileocolic artery and its dispersion in the microvasculature was observed by intravital microscopy of the intestinal mesentery. (b) Intensity–time curves of the bolus were recorded in post-capillary venules, and digitized at each time step along a radial line while focused on the diametral plane, as illustrated for indicator-dispersion curves along the centerline and near the vessel wall.

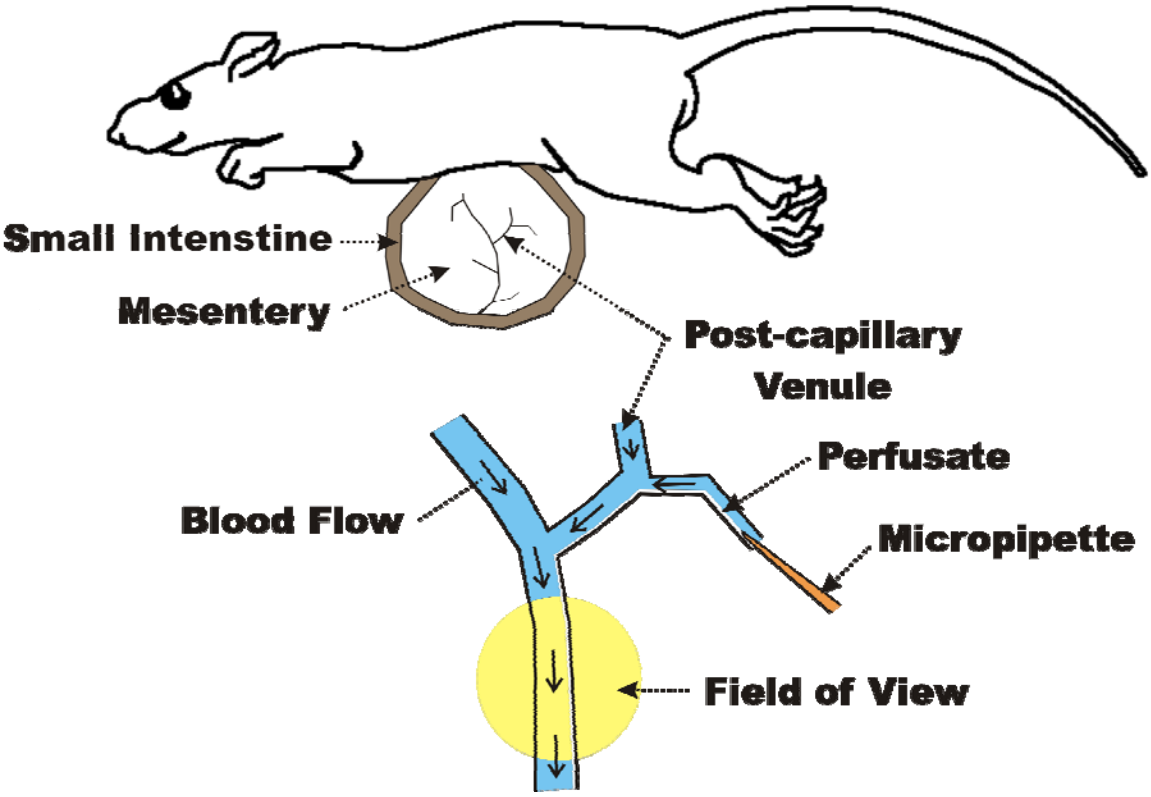

Figure 2: Schematic of the experiment protocol of direct post-capillary perfusion using micropipette. A post-capillary venule in the exteriorized rat mesentery was selected for intravital microscopic observation. An upstream branch was cannulated with a micropipette for perfusion with Alexa labeled BS-1 lectin to label the glycocalyx, or enzymes for GAG degradation. Fluorescence intensity of the endothelial surface was acquired to quantify glycan shedding.

2.2 Fluorescent Intravital Microscopy

Small intestines were exteriorized through a midline abdominal incision. A well vascularized mesentery tissue was draped over a clear glass pedestal that was under either tungsten lamp transillumination or fluorescent incident illumination by a Hg lamp and a dichotic mirror for visualization of the emission spectrum. Exteriorized tissue was superfused with 37°C HEPES-buffered ringer solution, and covered by cotton gauze. The experimental recording was through a Zeiss 40X/0.75NA water immersion objective. Diameter of the vessel was measured by video image shearing technique (image shearing monitor, Model 908, IPM, San Diego, CA). Red blood cell velocity (V_{RBC}) was measured along the centerline of each vessel using two-slit photometric technique with a self-tracking correlator (Model 204, IPM, San Diego, CA). The mean blood velocity was estimated from the VRBC by equation $V_{MEAN}=V_{RBC}/1.6$. The post-capillary venules were recorded by two sets of video systems. In experiments of indicator dispersion using FITC, a low-light silicon-intensified target (SIT) camera (Model 66, Dage-MTI, Michigan City, IN) records the filed a S-VHS tape recorder. The recorded movies were digitized at the resolution of 640x480 with a depth of 8 bits at 30 fps offline, using a Scion LG-3 frame grabber (Scion, Fredrick, MD). Digitized image stacks in TIFF format were then deinterlaced by separating odd and even fields of each frame using a linear interpolation algorithm to provide a 60 fileds/sec sampling interval. The resolution of the TIFF images is 7.53 pixels/μm. The rest of the experiments used a PCO® 1600 CCD camera that records 14-bit image stacks with 1600x1200 resolution at various exposure

time depending on protocols. The obtained spatial resolution with the Zeiss 40x/0.75NA objective is 17.32 pixels/μm.

2.3 Solutions

Five types of experimental related solutions were used:

1. FITC in PBS solution used as part of the indicator dispersion technique via ileocolic artery or diffusion coefficient measurement via micro-pipette
2. FITC-Dextran 70 kDa in PBS solution used as part of the indicator dispersion technique via ileocolica artery
3. BS-1 lectin (L2380, Sigma) conjugated with Alexa Flour 488 in PBS
4. Enzyme solutions in PBS for specific shedding of individual GAGs
5. fMLP Ringer solutions for inducing local inflammation

The preparation of solutions used in these four studies was listed as the following.

2.3.1 FITC and Dextran 70 kDa conjugated FITC in PBS solution

Solution of fluorescein isothiocyanate (FITC, F7250, Sigma) and FITC-Dextran 70kDa (FITC-Dx70, FD-70S, Sigma) in phosphate buffered saline (PBS) have been used in both thickness and permeability studies, but differing in concentration and route of drug administration, as listed in the Table 1 . FITC-Dx70 has high enough solubility to prepare the solution of desired concentrations by directly dissolve the FITC-Dx70 in

PBS. Centrifugation (16000 rpm, 5min) and filtering (0.26 μm polycarbonate syringe filter) were performed in sequence prior to each animal usage to eliminate high molecular aggregation that carries respiratory suppression toxicity toward rats. The solubility of FITC is highly pH dependent that peaks around pH = 10.0. Direct dissolving in PBS was achievable in low concentration like 0.1% (used in indicator dilution). However to prepare 1.0% FITC solution in D_{eff} measurements, lyophilized FITC power was first suspended in PBS solution and titrated using 1M NaOH solution till all suspension dissolved. While vigorous stirring, the pH of the solution was gradually brought down to 7.4 by slow addition of 1M HCl. The 1.0% FITC remains in soluble form up to 2 weeks at 4°C. Both FITC and FITC-Dx70 solutions were stored at 4°C.

Table 1: FITC and FITC-Dx70 solution used in this study

		Concentration	Route of Delivery
Correlation of δ, Kr and D_{eff} (Indicator Dilution)	FITC	0.1%	Ileocolic artery
	FITC-Dx70	0.2%	Ilieocolic artery
Thickness measurement	FITC-Dx70	0.1%	Jugular Vein
D_{eff} measurement	FITC	1.0%	Jugular Vein

2.3.2 Conjugation of BS-1 Lectin with Alexa Fluor 488

The conjugation of BS-1 lectin with Alexa Fluor 488 was through covalently binding of amine group with carboxyl group by the following protocol:

(1) Prepare carbonate/bicarbonate buffer stock by adding carbonate solution (0.21 mg carbonate in 10 ml distill water, pH = 11.0) to bicarbonate solution (1.68 gm in 100 nm distill water, pH = 8.0) until pH = 8.5.

(2) Dissolve 5 mg BS-1 lectin in 1 ml carbonate/bicarbonate buffer to achieve concentration of 5 mg/ml.

(3) Dissolve 1 mg Alexa Fluor in 0.1 ml dry DMSO

(4) Adding Alexa Fluor solution drop by drop (0.025 ml increments) to BS-1 solution, and stirring for 1 hour

(5) Total volume of the mixed solution was brought to 3.0 ml by adding 1.95 ml stock buffer

(6) Dialyze in PBS for 4 hours to remove unbound Alexa Fluor, using Slide-A-Lyzer (Pierce #6380, 10 kDa cutoff)

(7) Store in 4°C

The ratio of conjugation was computed by measuring the solution absorbance of BS-1 lectin at 280 nm and Alexa Fluor 488 at 495 nm wavelengths using spectrophotometer (Shimadzu, Columbia, MD). Steps and representative results are listed as the following:

(1) To get the extinction coefficient of BS-1 lectin, the absorbance at 280 nm of BS-1 lectin following step (2) of the conjugation protocol was read as $A_{280} = 0.406$, at

known concentration 5 mg/ml. The extinction coefficient at 280 nm can be calculated as $\varepsilon_{BS1} = \frac{A_{280}}{5/20} = \frac{0.406}{0.25} = 1.624$

(2) The optical density was measured again after dialysis at 280 nm and 495 nm, as $OP_{280} = 0.102$ and $OP_{495} = 0.409$. The optical density at 280 nm is contributed by the absorbance of both BS-1 lectin and Alexa Fluor 488, as

$$OP_{280} = A_{280}^{BS1} + A_{280}^{Alexa} = 0.102$$

It was previously determined for Alexa Fluor 488, $A_{280}^{Alexa} / A_{495}^{Alexa} = 0.11$

The absorbance at 280 nm for BS-1 lectin can then be calculated as

$$A_{280}^{BS1} = OP_{280} - A_{280}^{Alexa} = OP_{280} - 0.11 \cdot A_{495}^{Alexa} = 0.057$$

Using the extinction coefficient ε_{BS1}=1.624, the concentration of BS-1 after dialysis (in conjugation with Alexa Flour 488) is

$$[BS1] = 40 \times \frac{A_{280}^{BS1}}{\varepsilon_{BS1}} = 40 \times \frac{0.057}{1.624} = 1.404 \text{ mg/ml, or } 1.243\times10^{-5} \text{ mmol/ml}$$

where the value 40 refers to the dilution ratio and the MW of BS-1 is 113 kDa.

The concentration of Alexa Flour 488 was determined by taking reference to the linear absorbance-concentration curve of the fluorophore previously generated. The slope of the standard curve is $A_{495}^{Alexa} / [Alexa] = 71000$, where the concentration of Alexa is in the unit of mmol/ml. The post-dialysis concentration of Alexa was:

$$[Alexa] = 40 \times A_{495}^{Alexa} / 71000 = 40 \times 0.409 / 71000 = 0.23 \times 10^{-3} \text{ mmol/ml}$$

(3) The conjugation ratio was:

$$\frac{[Alexa]}{[BS1]} = \frac{0.23 \times 10^{-3}}{1.243 \times 10^{-5}} = 18.5 \text{ mol/mol}$$

or, 18.5 Alexa Fluor 488 molecules per BS-1 lectin molecule, which represents the typical range of conjugation.

2.3.3 Enzymes and fMLP solutions

Enzymes were used to cleave sugar residues of the endothelial glycocalyx, including heparinase III (50 units/ml, H8891, Sigma), chondroitinase ABC (10 units/ml, C2905, Sigma), bovine testicular hyaluronidase (3000 units/ml, H3631, Sigma) and neuraminidase (5units/ml, N3001, Sigma). Units used are Sigma units. Solutions of enzymes were prepared by direct injection of required volumes of PBS into the container bottle. *N*-formyl-methionyl-leucyl-phenylalanine (fMLP, F-3506, Sigma) was pre-prepared in saline at the concentration 10^{-4} M and stored in 1 ml aliquots at -20°C. Prior to each experiment, 1 ml 10^{-4} M fMLP was added in 1 liter freshly made Ringer-buffered saline solution to achieve the delivery concentration of 10^{-7} M.

2.4 Indicator Dispersion Technique using FITC

2.4.1 Technique of Indicator Dispersion

The flux of small solutes through the endothelial glycocalyx parallel to the wall of post- capillary venules was examined by infusion of a fluorescent indicator molecule (either low molecular weight fluoresceinisothiocyanate, FITC, or a high molecular weight fluoresceinated dextran 70kDa, FITC-Dx70, into the microvasculature of intestinal mesentery of the rat. Dispersion of the indicator was quantified by measurement of the intensity vs time curves, I(r,t), as a function of radial position (r) of the fluorescence emission as the bolus passed through a post-capillary venule. The dispersion was characterized by the first moment of the intensity-time curve, as typified by the classical Stewart-Hamilton method. For an indicator of infinitesimal volume and observed at a location where the entire indicator passes through the observation site, it has been shown that the first moment equals the mean transit time of indicator from injection to observation sites. It has also been demonstrated that between multiple observation sites within the microvascular network, when conservation of mass between the sites is maintained the first moment may also provide a useful measure of the mean transit time between sites. In the present approach, measurement of the first moment of the indicator at a specific radial position within a microvessel was interpreted as a virtual transit time, VTT(r), from an indeterminate source, as schematized in Fig, 1b, with its value obtained from:

$$VTT(r) = \frac{\int_0^\infty I(r,t) \cdot t \cdot dt}{\int_0^\infty I(r,t) \cdot dt} \qquad 1$$

As shown in the following experimental and computational models, the radial distribution of VTT(r) may be related to the diffusional characteristics of the indicator and the resistance to flow of its solvent as the indicator is transported through the endothelial glycocalyx.

2.4.2 Experimental Protocol

Two types of fluorescent tracers were used in the indicator dispersion experiments, FITC that can freely penetrate the glycocalyx structure and Dextran70 conjugated FITC that is incapable of glycocalyx penetration. In brief, FITC (4mg) was dissolved in 3 drops of DMSO (0.1mL). The Ringer solution (pH 7.4) was then added to bring the total volume to 4mL to achieve the delivery concentration of 0.1%. To have the same absorbance at 495nm as 0.1% FITC solution, 0.2% FITC-Dextran70 solution was made by dissolving 6mg FITC-Dextran70 in 3mL Ringer solution. To deliver the fluorescent tracers, the terminal part of the ileocolic artery was cannulated via PE10 polyethylene tubing. A small bolus of FITC or FITC-Dx70 was injected manually via the ileocolic cannula. During control period, multiple boli (3-5) were delivered for each venule. 2-3 venules were recorded in each animal experiment. Then Ringer was replaced by fMLP (10^{-7}M) Ringer solution to irrigate the mesenteric tissue for another 30min. After 10min, the second set of boli (3-5) was given for the same venules to establish the inflammatory cases.

2.4.3 Image Processing

It took 2-3 seconds for a bolus to pass through the field of view. For that reason, 4.5-second length of each bolus recording was digitized to a 128-frame TIFF stack at 30 fps. The spatial resolution is 640 × 480 pixels with a depth of 8 bits gray scale. Using a macro (see attachment) on ImageJ (NIH, Bethesda, MD), each frame of the digitized TIFF image stack was deinterlaced into two frames by separating the even and odd scanlines of each frame so that the frame rate was increased from 30 to 60 fps. In brief, the even horizontal scanlines of each frame were extracted first and the odd scanlines were filled by linear interpolation from the even lines. The second frame exacted was the even horizontal lines and filled by interpolations. The deinterlacing increased the temporal resolution of the recording and decreased the spatial blurring introduced by interlaced scanning of NTSC analog camera.

2.4.4 Data Analysis

After deinterlacing, a TIFF stack consists 256 frames with refresh rate of 60 fps. All digitized intensities were corrected by subtraction of the background fluorescent intensity obtained in the absence of the fluorophore. Background fluorescence was the average during 10-15 frames prior to the arrival of each bolus. Background fluorescence arose from the tissue autofluorescence and the presence of recirculating fluorescent molecules from previous infusion. For each vessel, radial measurement lines were drawn across the entire vessel lumen, normal to the direction of blood flow. Axial locations of

measurement lines were picked with the criterion that no adhered WBCs were on the measurement line. Intensity-time data sequences were recorded on each pixel of a selection line using the ImageJ. Subsequently, the virtual transit time was calculated for each pixel of the measurement line using Eq. 1.

To establish a radial window of consistent size near the plasma membrane of the endothelium, within which the glycocalyx could potentially retard progression of the indicator, optical power (OP) was calculated from the intensity time curve at each radial position using the definition:

$$OP(r) = \int_0^T \left(I(r,t) - I_{mean}(r)\right)^2 dt \qquad 2$$

where $I_{mean}(r) = \frac{1}{T}\int_0^T I(r,t)dt$ is the time averaged fluorescence intensity and T is the duration of the bolus. The optical power varies with radius due to the transient quenching of the fluorescence as red blood cells pass a given axial station, and due to the transient intensity changes with varying concentration of the fluorophore. As shown in ‘‘Results,’’ as the surface of the EC is approached along a radial line, *OP*(*r*) diminishes and an inflection point in *OP*(*r*) occurs as fluctuations in dye intensity from red cell passage begins to decrease relative to fluctuations arising from changes in dye concentration during passage of the bolus.

2.4.5 Computational Simulation of FITC Transport inside the Glycocalyx

To interpret the measurements of VTT(r) in terms of the permeability to solutes and the resistance to fluid transport within the glycocalyx, an annular core model of blood flow in a small bore tube of circular cross- section with three annuli was adopted. This model consisted of a central core of red cells ($0 \le r < r_c$) surrounded by an annulus of cell free plasma ($r_c \le r < r_g$) which was in turn surrounded by a porous layer lining the wall of the tube ($r_g \le r \le R$) which was representative of the glycocalyx of uniform thickness δ, where r_c, r_g and R are radial boundaries of the central core, glycocalyx and vessel wall, respectively.

Within the central red cell core and adjacent annular plasma layer, a two-layer model was adopted, following the model of Sharan and Popel (50). The outer cell-free plasma layer spans from r_c to r_g, with apparent viscosity μ_p. Within the central core an apparent viscosity μ_c that was greater than μ_p was assumed, to account for the presence of red cells. Fluid flow within the glycocalyx was modeled as a two-dimensional flow field parallel to the wall as governed by the Brinkman equation. The momentum conservation equations for these three layers are:

$$\begin{cases} \dfrac{\mu_c}{r}\dfrac{\partial}{\partial r}\left(r\dfrac{\partial u}{\partial r}\right) = \dfrac{\partial P}{\partial x} & 0 \le r < r_c \\ \dfrac{\mu_P}{r}\dfrac{\partial}{\partial r}\left(r\dfrac{\partial u}{\partial r}\right) = \dfrac{\partial P}{\partial x} & r_c \le r < r_g \\ \dfrac{\mu_P}{r}\dfrac{\partial}{\partial r}\left(r\dfrac{\partial u}{\partial r}\right) = \dfrac{\partial P}{\partial x} + K_r \cdot u & r_g \le r \le R \end{cases} \qquad 3$$

where r and x denote the coordinate system in radial and axial directions, respectively, u is the velocity in the axial direction, $\partial P/\partial x$ is the longitudinal pressure gradient, and Kr is the hydraulic resistivity within the glycocalyx. To implement the computations, a range of Kr from 10^4 to 10^{14} dyn·s/cm^4 was explored. A red cell core layer viscosity of μ_c = 3.84 cP was computed using Eq. 4 (from Sharan and Popel (50)), assuming Hc = 0.45 within a post-capillary venule.

$$\frac{\mu_c}{\mu_p} = 1 + 2.2\frac{(1-Hc)^{-0.8} - 1}{(1-0.45)^{-0.8} - 1} \qquad 4$$

The viscosity of plasma was taken as μ_p = 1.20 cP (38).

Solution of the system of Eq. 3 was implemented for the following boundary conditions:

(i) Axisymmetric flow along the vessel centerline

$$\frac{\partial u}{\partial r} = 0, \text{ at } r = 0$$

(ii) No slip boundary at the blood vessel wall

$$u = 0, \text{ at } r = R, \text{ and}$$

(iii) No slip at adjacent layers

$$u_{r=r_{c-}} = u_{r=r_{c+}}$$
$$u_{r=r_{g-}} = u_{r=r_{g-}}$$

The transient mass transfer of the dye bolus is affected by two processes: convection in the axial direction and diffusion in both radial and axial directions, as specified in the following equation,

$$\frac{\partial c}{\partial t} + u\frac{\partial c}{\partial x} = D_x \frac{\partial^2 c}{\partial x^2} + \frac{D_r}{r}\frac{\partial}{\partial r}\left(r\frac{\partial c}{\partial r}\right) \qquad 5$$

where c is the concentration of the indicator molecule as a function of time (t), radius (r) and length (x). D_x and D_r are the effective diffusion coefficients of the indicator molecule in plasma in axial and radial directions, respectively. In the present study, the effective diffusion coefficient was assumed to be isotropic, $D_x = D_r = D$. However, the isotropic diffusion coefficient assumes different values for core, plasma layer and the glycocalyx layer. Diffusion coefficients in the core and plasma layer were taken as the free diffusion coefficient (D_{free}) of FITC in aqueous media 2.7×10^{-6} cm^2/s (Periasamy and Verkman, 1998). Although mixing effects of RBCs may contribute to a higher effective diffusion coefficient in the core layer, parametric numerical simulations indicated that the variation of diffusion coefficient in the core had minimal impact on the radial distribution of VTT. Similarly, varying the diffusion coefficient in the plasma layer by assuming a 90% reduction due to the presence of macromolecules, revealed less than a 5% reduction in the variation of VTT(r) with radial position near the EC.

Solution of the mass transfer equation was obtained with the boundary conditions:

(i) Axisymmetric flow along the vessel centerline

$$\frac{\partial c}{\partial r} = 0,\ r = 0$$

(ii) No flow transport normal to the vessel wall,

$$\frac{\partial c}{\partial r} = 0, \text{ r = R, and}$$

(iii) Well mixed entrance flow, with uniform concentration along the vessel radius which varied only as a prescribed function of time

$$c = c_{ent}, \text{ at x = 0}$$

where c_{ent} was taken from experimental recorded intensity time curves in the post-capillary venule.

The governing differential equations (Eq. 3 and Eq. 5) were solved in a two-step process using the finite element solver of Comsol Multiphysics, version 3.5 (Comsol Inc., Burlington, MA) using a triangular mesh. The stationary velocity profile was computed by the built-in direct UMFPACK (Unsymmetric Multi-frontal sparse LU Factorization Package) solver. The stationary velocity profile was stored and used to solve for transient concentration profiles using the UMFPACK linear solver.

The result from simulation, shown as Fig. **3**, the entrance effect has very limited effect on the $\Delta VTT/\Delta r$ when the axial location x/D is above 30. The simulated length of a post-capillary venule was taken as 1 mm (>30 times diameter) to allow sufficient mixing. Vessel diameter was assumed to be 30 μm. Values for the cell-free plasma layer were obtained from *in vivo* measurements.

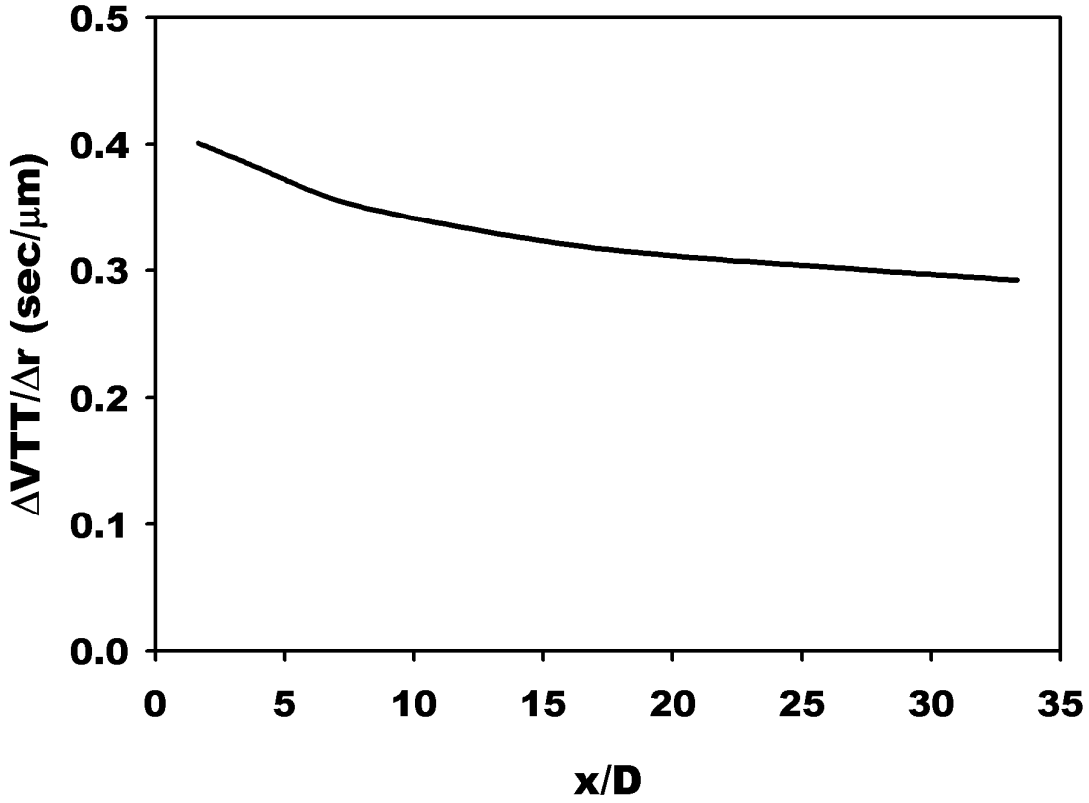

Figure 3: Variations of DVTT/Dr with the axial location x/D. The result was from the simulation of the dispersion of a FITC bolus in a 30 μm diameter vessel coated with 500 nm glycocalyx layer. The hydraulic resistivity is 1×10^{-9} dyn·sec/cm^4. The effective diffusion coefficient of FITC is 5.5×10^{-5} cm^2/sec.

2.5 Enzymatic Shedding of BS1 labeled GAGs

BS-1 lectin, a permissive GAG-binding molecule that binds to all three principal GAGs (Schnitzer et al., 1990), HS, CS, and HA, was used to examine enzymatic removal of components of the endothelial glycocalyx. BS1-Alexa solution was infused continuously for 10 min. The micro-pipette was then withdrawn to allow resuming of the blood flow to washout non-bound BS1-Alexa. Fluorescent intravital microscopic reading #1 was taken 10 min after the end of the BS1-Alexa infusion. Six different tissue treatments were entailed, no treatment (control), fMLP, heparinase, chondroitinase, hyaluronidase and neuraminidase.

The labeling of the sugar residues of the glycocalyx, an upstream branch venule to the targeted post-capillary venule was inserted with a micro-pipette by micro-cannulation described in 2.1. GAGs of the post-capillary venule were perfused with BS1-Alexa for 10 min. Micro-pipette was then removed to resume the blood flow for another 10 min so that unbound fluorophores can be washed out. The first set of microscopic readings was then taken (20 min post-BS1) as the control. The second set of readings was taken after another 40 min (60 min post-BS1). During the 40 min, the venule was cannlated again for a 10-min infusion of heparinase, chondroitinase or hyaluronidase. For the no-treatment and fMLP cases, no micro-cannulation was performed and tissue was irrigated topically with Ringer solution or 10^{-7} M Ringer solution, respectively. Timelines of these different treatments were listed in Table 2.

The method for quantifying the extent of BS1-Alexa binding to the EC is illustrated in Fig. 4 for a representative post-capillary venule in both brightfield (Fig. 4A) and fluorescence (Fig. 4B) illumination. In this particular venule, infused BS1-Alexa solution stream was confined to the left venular wall (Fig. 4B). The luminal surface of the EC was identified as the outer edge of the dark refractive band in the brightfield image. BS1 staining appears on the luminal side of the EC. A measurement line was drawn along the center of the fluorescent band and the average fluorescence intensity was recorded in a region of interest (ROI) along this line bounded by the edges of the band, which typically spanned about 500 nm on either side of the line. The total width of the ROI was 1000 nm, which covers the typical thickness of the glycocalyx.

Table 2: Experimental Timeline of Enzymatic shedding of BS1-GAG

Time (min)	No stimulus (Control)	fMLP	Hepari -nase	Chondroi -tinase	Hyaluroni -dase	Neurami -nidase	Chondrotinase-Neuraminidase
							Cannulation
-20							
-10							Chondrotinase
	Cannulation						
0	BS1 infusion						
10	Normal blood flow / Ringer						
20	Reading 1						
30	Normal flood flow / Ringer	Normal flood flow / fMLP	Cannulation				
40			Hepari -nase	Chondroi -tinase	Hyaluroni -dase	Neurami -nidase	Neuraminidase
50			Normal flood flow / Ringer				
60	Reading 2						

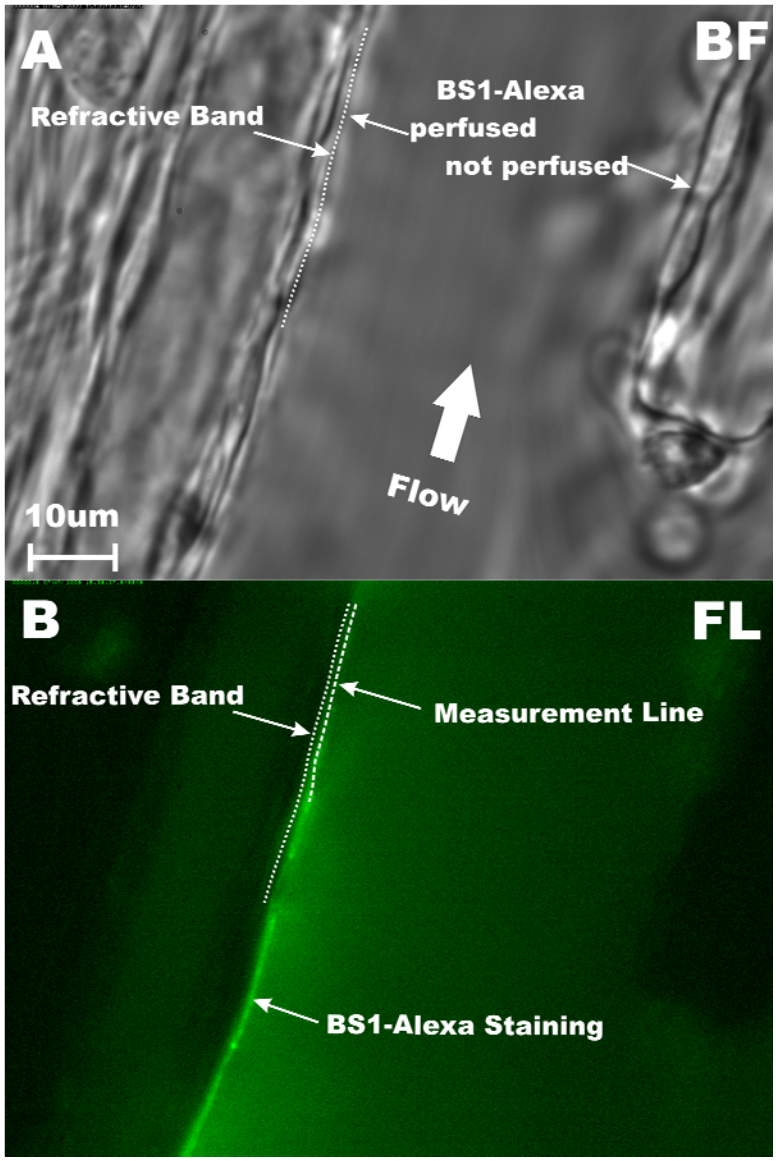

Figure 4: Fluorescent labeling of the endothelial cell (EC) glycocalyx. (A) Brightfield image of a post-capillary venule (diameter = 40.7 μm). The plasma membrane of the EC was taken as the outermost edge of the dark refractive band between the EC and plasma layer. (B) Fluorescence image 10-min following proximal micropipette infusion of BS1-Alexa lectin. In this example fluorescence was confined to the left microvessel wall due to heterogeneity of network perfusion. A measurement line was drawn along the left EC wall and fluorescence intensity was averaged over an area within 0.5 μm on either side of the measurement line.

2.6 Measurement of Barrier Layer Thickness

The thickness of the glycocalyx layer was estimated by measuring the distance between the luminal surface of the EC and the edge of circulating FITC-Dx70, introduced into the systemic circulation as a bolus (0.1% in 0.15 ml) via the jugular vein cannula. After completion of the bolus infusion, brightfield images were taken of selected post-capillary venules, in a focal plane where the dark refractive band at the EC luminal surface was sharply in focus. The microscope was then switched to fluorescence epi-illumination and video scenes of the edge of the FITC-Dx70 dye column were recorded without disturbing the image alignment with the brightfield image.

2.7 Glycocalyx Layer Permeability Measurement

The thickness of the glycocalyx layer was estimated by measuring the distance between the luminal surface of the EC and the edge of circulating FITC-Dx70, introduced into the systemic circulation (0.1% in 0.15 ml) via the jugular vein cannula. After completion of the bolus infusion, brightfield images were taken of selected post-capillary venules, in a focal plane where the dark refractive band at the EC luminal surface was sharply in focus. The microscope was then switched to fluorescence epi-illumination and video scenes of the edge of the FITC-Dx70 dye column were recorded without disturbing the image alignment with the brightfield image.

The images were analyzed by drawing a line along the EC surface under brightfield (Fig. 5A) and then overlaying this line on the fluorescence image (Fig. 5B). The radial distribution of fluorescence intensity was then obtained along a radial

measurement line with its center on, and normal to, the EC boundary line, as shown in Fig. 5B. This radial measurement line was moved along the EC boundary line to acquire a radial distribution at each pixel of the boundary line and calculate an average radial intensity profile for up to 1600 locations along the boundary (symbols in Fig. 6). The radial distribution of intensity was then fit with a 5-parameter sigmoidal curve, $I = I_0 + a\left(1 + e^{\frac{r - r_0}{b}}\right)^{-c}$ (solid line in Fig. 6). The inflection point of this curve (IP) was calculated from the curve fit parameters as $IP = r_0 + b \cdot \ln(c)$ and taken at the location of the edge of the glycocalyx. The distance between the EC wall and IP was taken as the thickness of the glycocalyx layer. The separation of IP from EC wall increases slightly with the vessel diameter with slope 4.38 nm/μm (p = 0.027), as shown in Fig. 7. However, values of the control thickness for all treatments are not significantly different from each other, as shown later in Chapter 4. All the image processing and measurements were done using ImageJ.

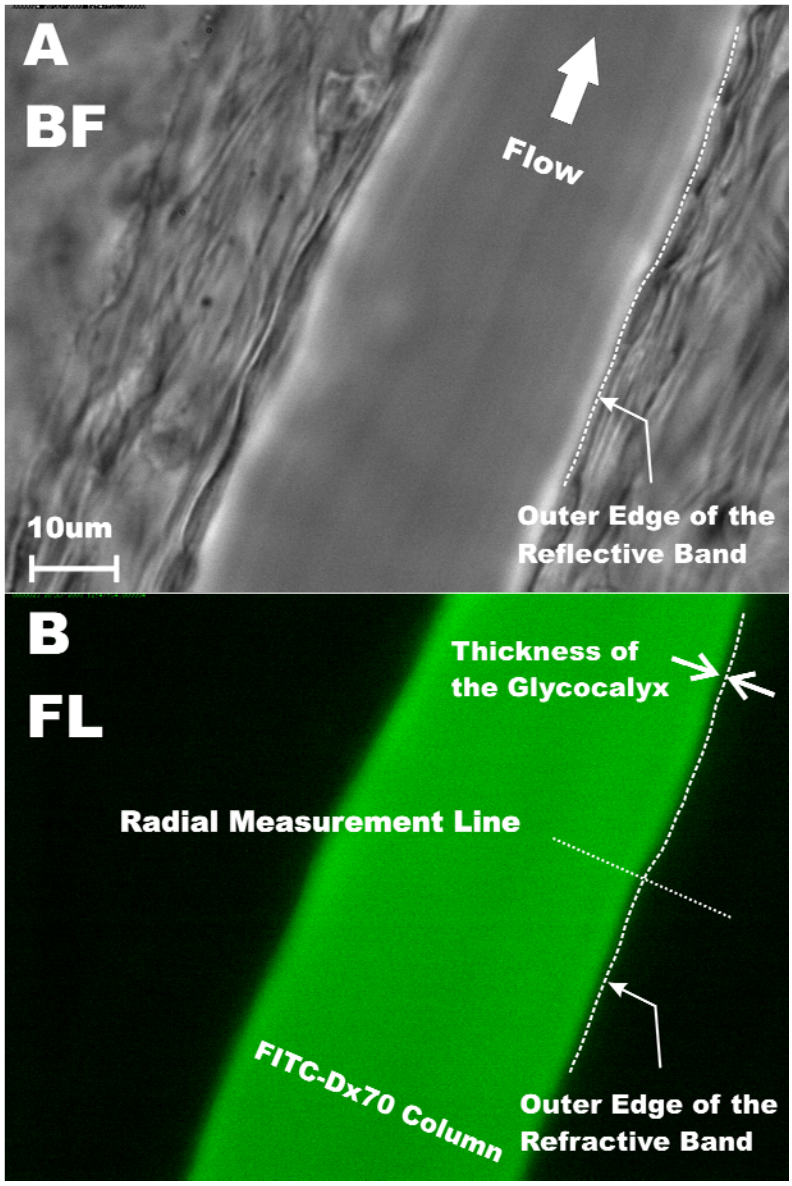

Figure 5: Measurement of glycocalyx thickness. (A) Brightfield image of a post-capillary venule (dia = 35 μm) after a 0.15 mL systemic FITC-Dx70 bolus injection. The outermost edge of the dark refractive band was taken as the surface of the EC. (B) Fluorescence micrograph with circulating FITC-Dx70.

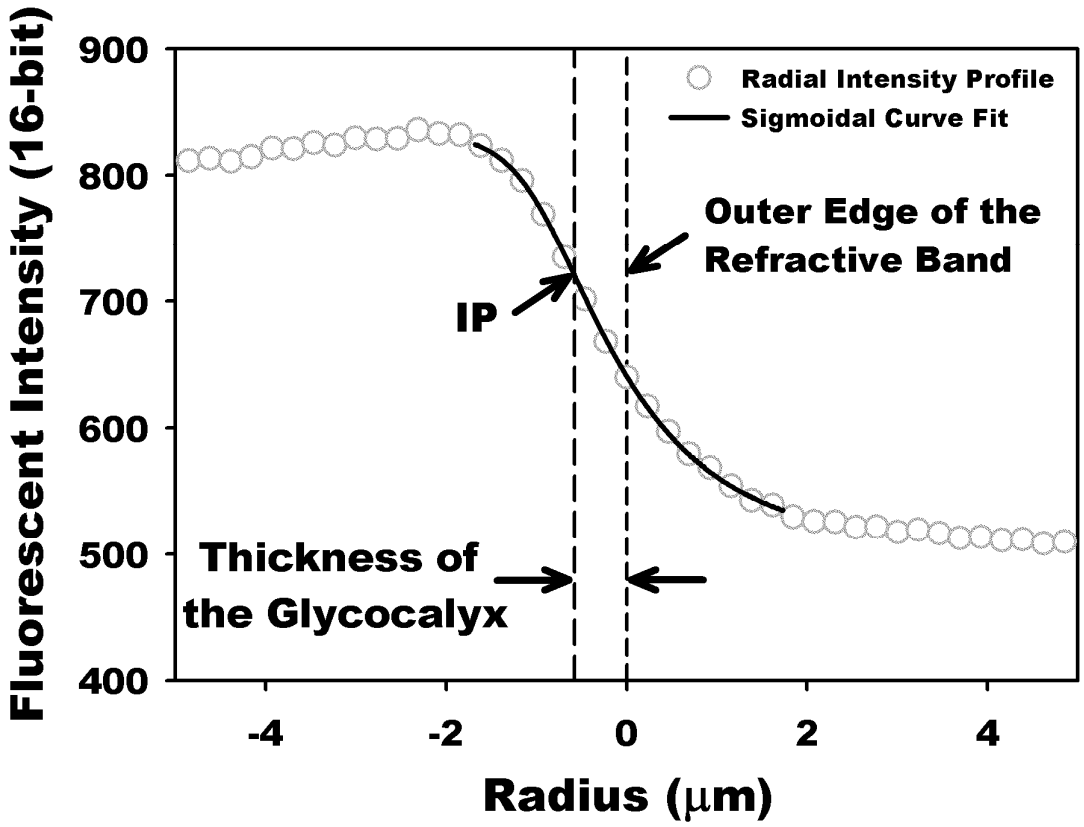

Figure 6: Fluorescence intensity distribution (open symbols) along a radial measurement line was fit with a sigmoidal curve (solid line) to determine its inflection point, IP. The distance between the IP and the EC surface was taken as the thickness of the glycocalyx.

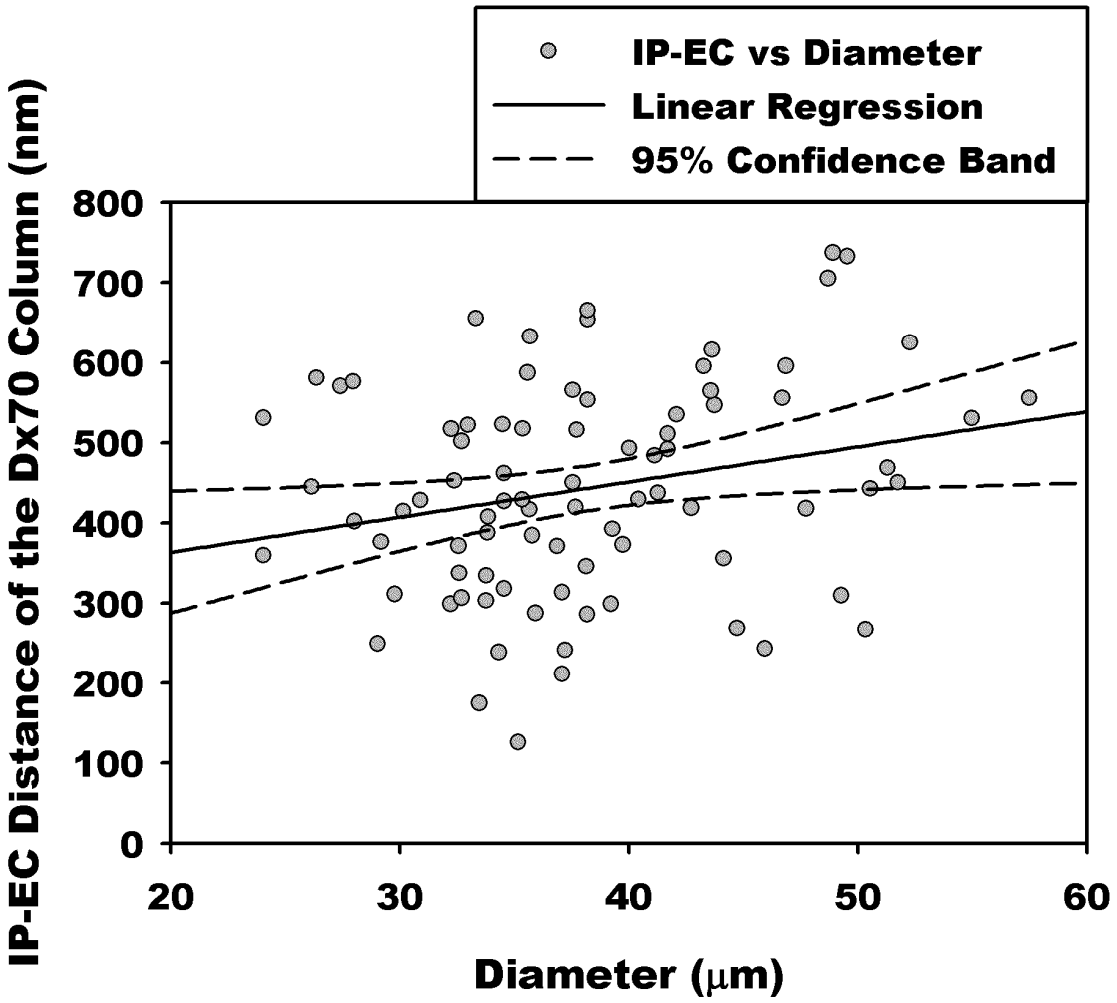

Figure 7: The distance of IP from the EC surface for FITC-Dx70 dye column under control condition. Data included all control cases from fMLP, heparinase, chondroitinase, hyaluronidase and enzyme mixture.

Free FITC solution was given as a systemic bolus (0.16mL at 1.875mL/min) using a syringe pump (PhD2000 Programmable, Harvard Apparatus, Holliston, MA) via the jugular vein catheter. The first 10 seconds of the fluorescent bolus passing through the venular section was recorded at 2 frames/s (500 ms exposure time per frame). Brightfield images were recorded following the bolus to locate the EC surface. The radial intensity profiles over 1 μm distance from the EC boundary was recorded with a spatial resolution of 17.3 pixel/μm to obtain the transient distribution of intensity, I(r,t). The intensities recorded at the location of the edge of the glycocalyx (determined from previous Dx70 measurements) I(δ,t), were used as the boundary conditions for a computational model of quasi-1-D transient diffusion through a porous layer bounding the EC surface. The diffusion coefficient, D, of FITC molecules inside the glycocalyx was estimated by determining the value of D which yielded the best agreement of computed and measured distributions of I(r,t).

The transient diffusion of a solute of concentration c(r,t) through a porous layer of thickness δ was obtained from the one-dimensional diffusion equation, non-dimensionalized in time, radial distance and concentration to yield,

$$\frac{\partial \theta}{\partial \tau} = \frac{\partial^2 \theta}{\partial \eta^2} \qquad 6$$

where the dimensionless parameters are $\theta = \frac{c}{c_m}$, $\eta = \frac{r}{\delta}$, $\tau = \frac{t \cdot D}{\delta^2}$, D is the diffusion coefficient, and c_m is the maximum concentration of solute at the edge of the glycocalyx, r = δ, and r = 0 at the EC surface. The initial concentration within the layer was taken as c(r,0) = 0, and the concentration at the outer edge, c_δ = c(δ,t), was taken from

measurements. The concentration of solute, c(r,t), was assumed to be linearly proportional to fluorophore intensity, I(r,t), for which the background intensity at each pixel was subtracted off using values taken under fluorescence illumination immediately prior to entry of FITC into the video field.

The differential equation, Eq. 6, and boundary conditions were rewritten into finite difference equations with 2nd order accuracy in space and time. Equation (1) was solved using a fully implicit computation scheme in MatLab (The MathWorks Inc., Natick, MA), for specified values of $c_\delta(t)$ and D. The surface depicting a solution of c(r,t) was compared with the experimental measurements of I(r,t) by computing the root mean square (RMS) error $\varepsilon = \sqrt{\frac{1}{N}\sum\left(1-\frac{c(r,t)}{I(r,t)}\right)^2}$, where N is the total number of measured data points. An iterative method was used to determine the diffusion coefficient that yielded a minimum in the RMS error which was selected as the solution. Fig. **8** shows the RMS error plotted against the diffusion coefficient corresponding to each case. The RMS error has a single minimal value, where the corresponding D was used. However, the curve is not symmetric on either side of the minimum. The RMS error reaches a limit as the diffusion coefficient increases. This limit is determined by the cumulative difference of intensity between each pixel inside the glycocalyx and the pixels on the luminal boundary. The difference between the minimal RMS errors to the RMS errors at higher end of the diffusion coefficient is largest for control, which suggests the maximal barrier capability for the glycocalyx. The precision of this technique enabled resolution of D to within a numerical error of 0.5%.

2.8 Statistical Methods

Statistical analyses of the data were performed using SigmaStat 3.0, SPSS Inc. Multiple comparisons of different treatments were performed using the Student-Newman-Keuls test for one-way ANOVA. Statistical significance was asserted when the probability of the null hypothesis being true was $p < 0.05$. Statistics of vessel diameters for all three protocols, glycocalyx thickness and goodness of fit (R^2 or RMS error) for $\Delta VTT/\Delta r$ and diffusion coefficient measurements are listed in Table 3 and Table 4 respectively.

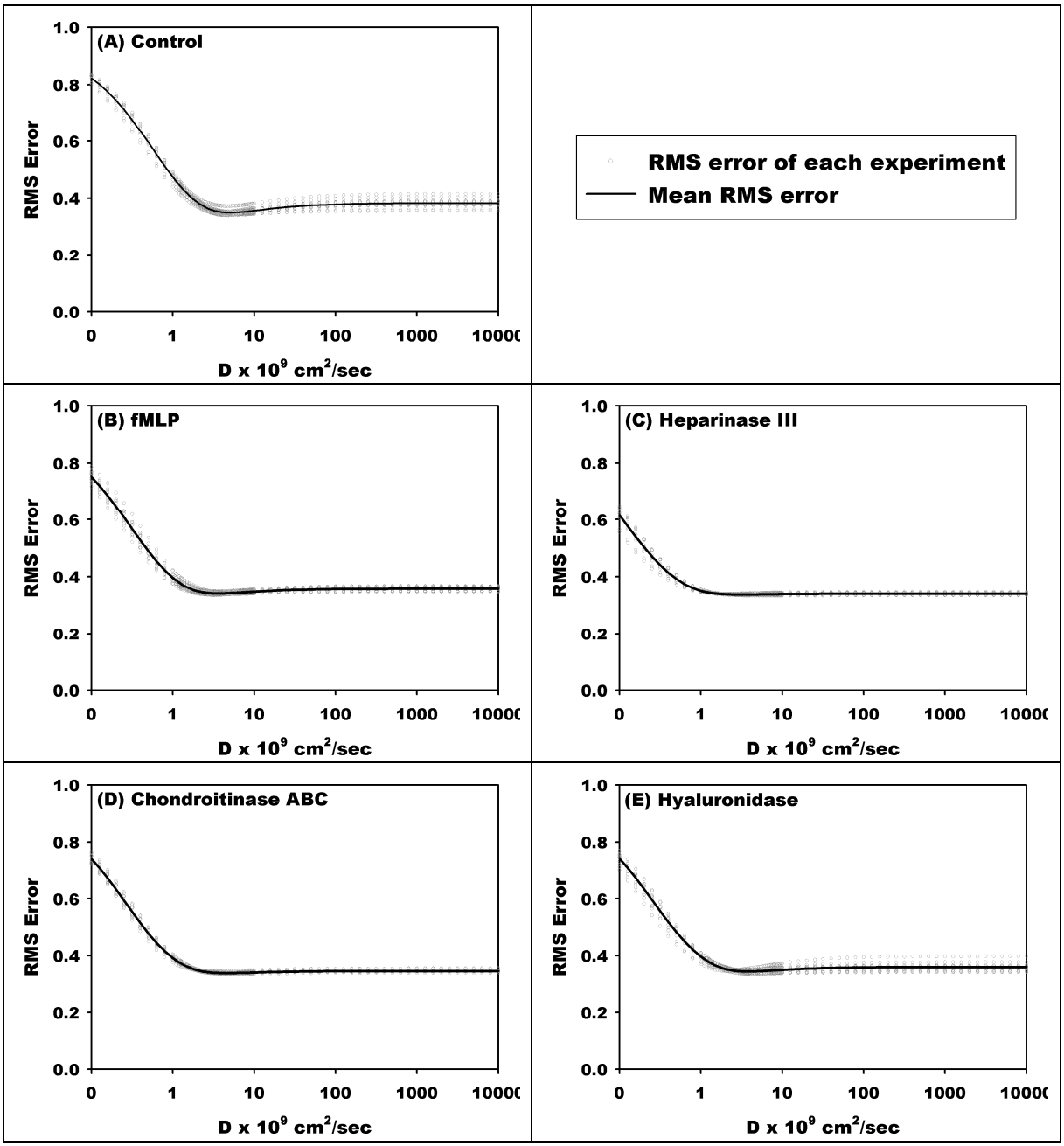

Figure 8: A representative result of RMS error versus the diffusion coefficient of FITC across the whole glycocalyx layer. In each treatment, a single minimum RMS error exists, at which the corresponding diffusion coefficient was taken as the solution.

Table 3: The RMS errors of linear regressions in determining values of $\Delta VTT/\Delta r$

		N	R^2	RMS Error
FITC	Control	108	0.66 ± 0.22 *	4.4 ± 2.2 %
	fMLP	90	0.64 ± 0.24 *	3.6 ± 3.8 %
FITC-Dx70	Control	112	0.52 ± 0.26 *	4.5 ± 3.0 %
	fMLP	130	0.59 ± 0.27 *	3.6 ± 2.3 %

* There is a statistically significant difference between R^2 and 1, $p \leq 0.001$.

Table 4: Statistics of vessel diameters and curve fits determining the boundary of the glycocalyx and the diffusion coefficient of FITC

	Treatment	Control	Hepari-nase	Chondroi-tinase	Hyaluro-nidase	Enzyme Mix	fMLP
(A) BS1 Cleavage assay	N	12	8	8	12		11
	Diameter (μm)	42.6 ± 6.19	45.4 ± 8.1	47.2 ± 8.3	44.6 ± 7.1		42.1 ± 11.4
(B) Sigmoidal fits of FITC-Dx70 radial intensity *	N	77	14	17	16	17	13
	Diameter (μm)	38.3 ±7.58	37.8 ± 10.3	40.0 ± 8.5	39.9 ± 6.2	36.9 ± 5.7	36.2 ± 5.2
(C) Intensity-distance-time fits for diffusion coefficient calculation	N	10	7	7	8		9
	Diameter (μm)	25.5 ±5.9	27.7 ± 8.1	38.3 ± 10.8	35.7 ± 13.3		27.4 ± 7.4
	RMS error (%) D_{Dx70}	35.0 ± 0.9%	33.8 ± 0.2%	33.9 ± 0.2	34.5 ± 0.6		34.2 ± 0.4
	RMS error (%) D_{173}	33.7 ± 0.2%	33.6 ± 0.1%	33.5 ± 0.1%	33.8 ± 0.2%		33.7 ±0.2%

Data are Mean ± SD

In each case, all treatments were not statistically significant from control for diameter and goodness of of of fit.

* For all sigmoidal fits, R^2=0.9998±0.0001 SD

Chapter 3

Solute Transport in Glycocalyx

The endothelial glycocalyx functions as a selective sieving barrier to the vasculature that impedes the efflux of the liquid and the macromolecules of the blood plasma, and shields the endothelial cells from interrogation of the circulating WBCs under physiological conditions. This barrier function can be expressed in terms of three independent variables that are the targets of this study. These independent variables are thickness of the glycocalyx layer (δ), effective diffusion coefficient of the solute (D_{eff}), and hydraulic permeability (Lp). D_{eff} expresses the ability of the glycocalyx to diminish the flux of plasma solutes. Lp determines resistance to solvent (water) flow through the glycocalyx layer.

3.1 Experimental measurements of VTT

Fig. 9 presented brightfield and fluorescence image of a 30 mm diameter post-capillary venule as the peak of a FITC bolus pass through the vessel. A measurement line was place across the vessel perpendicular to the local direction of the flow. Fluorescence intensity along the measurement line was digitized to compute the VTT(r) Eq. 1 and optical power, OP(r) Eq. 2. The plasma layer separating the red blood cell core and the EC, the EC surface and the location of the inflection point in OP(r) are shown. The surface of the EC was taken as the outermost edge of the dark refractive band that

parallels the EC that is consistent with the surface upon which leukocytes can be clearly observed to roll. Average thicknesses of the plasma layer between the edge of the RBC core and the EC surface are given in Table 5 for control and fMLP-treated conditions. No significant difference was found for location of IP or plasma layer thickness between control and fMLP for either FITC or FITC-Dx70.

The intensity time curve I(r,t) corresponding to each pixel along the radial measurement line is shown in Fig. 10 for dispersion of the FITC bolus. At each radial position, the intensity-time curve appears as a log-normal shaped distribution. Near the wall of venule (r=R) the glycocalyx layer appears to hinder progression of bolus, as manifested by a delayed peak time and prolonged and elevated tail. In the vicinity of the venule centerline (r/R=0) light scattering by red cells results in diminished peak intensity of the fluorescence emission at a given radius, which gives the bolus a parabolic appearance in the radial direction. Average red cell velocity within this venule equaled 3.0 mm/sec. The transient intensities near the centerline of the vessel were averaged over 5 adjacent pixels (~0.7 μm) to reduce noise and used as an input function for the computational model.

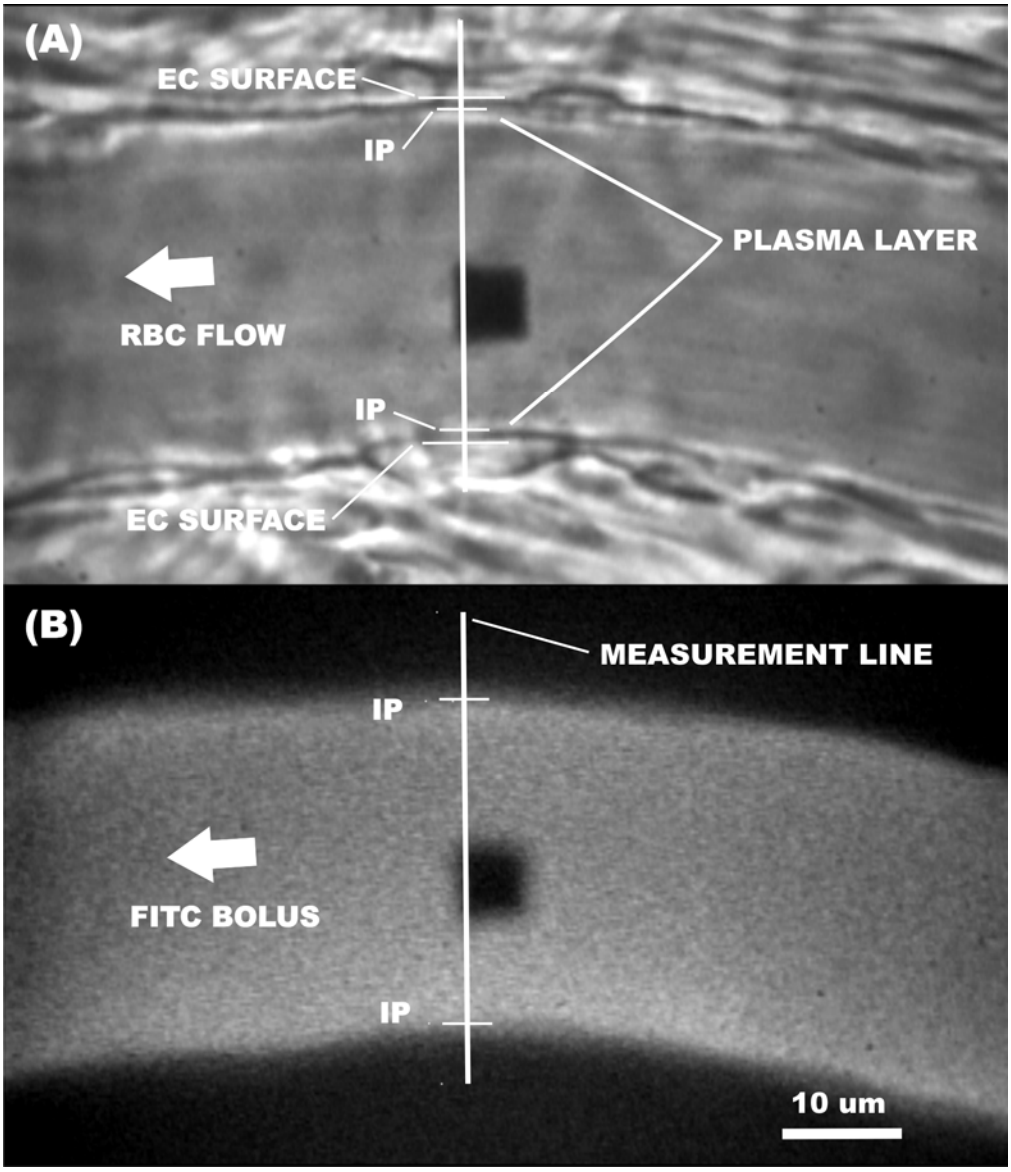

Figure 9: Intensity–time curves were measured along a line normal to the vessel longitudinal axis, shown above for (a) brightfield and (b) fluorescence images of a 30 μm diameter venule. The radial location of inflection points (IP) in the optical power and the endothelial cell (EC) surface are indicated by the short bars normal to the measurement line. The EC surface was taken at the outermost edge of the dark refractive band along the EC, which is consistent with the location of adhering and rolling leukocytes. The location of the IP is within the plasma layer, between the red blood cell column (RBC) and EC surface. The square black box in the center is the photodetector used for measurement of RBC velocity by the two-slit photometric method.

Table 5: Measurements of the plasma layer thickness and inflection point location

Distance	FITC		Dextran-70	
μm	Control	fMLP	Control	fMLP
n	51	51	27	27
Inflection Point - EC Surface	0.90±0.25	0.93±0.23	1.11±0.25	1.10±0.35
Red Cell Column - EC Surface	1.77±0.35	1.85±0.58	1.97±0.25	1.80±0.38

Table 6: Summary of Indicator Dispersion Experiments

	Number of Vessels	Number of Bolus Injections	Venule Diameter (μm)	Velocity (mm/sec)	VTT(R) (sec)
(a) FITC					
Control	9	51	24.88±4.09	2.83±1.03	1.49 ± 0.26
fMLP	9	51		2.26±1.19	1.59 ± 0.38*
(b) Dextran-70					
Control	5	27	25.72±3.8	2.37±0.61	1.35 ± 0.34
fMLP	5	27		2.01±0.92	1.42 ± 0.27†

Values shown are mean ± SD for venular diameter, centerline RBC velocity and virtual transit time (Eq. 1) evaluated by extrapolating VTT(r) to the wall, r=R. VTT(R) not significantly different from control, t-test: *p = 0.124, †p=0.406.

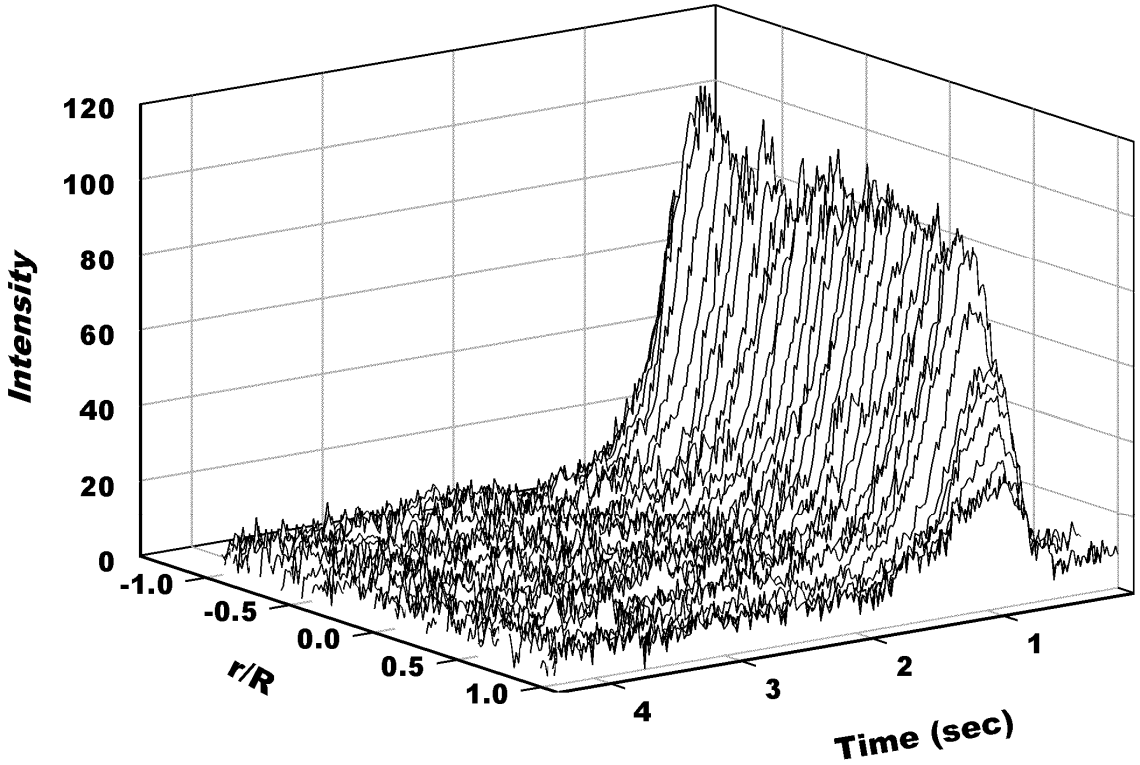

Figure 10: Representative intensity–time curves against radius for dispersion of a bolus of FITC in a 30 μm diameter venule with centerline red cell velocity of 1.5 mm/s. Fluorescence intensity was digitized using an 8-bit gray scale, and taken as proportional to solute concentration. Data were corrected for background intensity by averaging the radial profile over the 0.5-s prior to appearance of the bolus and subtracting the background from the bolus recording. The presence of red cells attenuates the bolus intensity along the microvessel centerline due to absorption of the excitation and emission, and light scattering. Peak intensity (with time) falls near the vessel wall due to dispersion of the bolus, and is delayed relative to the peak at the centerline.

To explore the emission intensity distributions near the vessel wall in greater detail, shown in Fig. 11a is the radial distribution of I(r, t) at the time at which intensity reaches a maximum and also for the time at which intensity at the wall reaches a maximum value for the 30 μm venule of Fig. 10. The vertical dashed line in each panel represents the locations of the inflection points in the optical power Eq. 2. Near the wall, both radial distributions exhibit similar slopes as the intensity diminishes with increasing distance from the luminal plasma layer. As shown in Fig. 4b, the total integrated mass flux ($\int_0^\infty I(r,t)dt$) reveals a characteristic decrease in magnitude with radius in the vicinity of the wall, which is indicative of dilution of the indicator with its dispersion along the axis of the vessel. The total mass passing the near-wall region between the EC and IP is 50% or less of the centerline, despite the fact that the indicator molecule is well mixed with plasma when entering the post-capillary venule. This behavior is consistent with diffusion of the indicator from the glycocalyx toward the center region when its concentration is higher than outside of the glycocalyx layer, at the trailing edge of the bolus, as illustrated in panel (a).

The optical power calculated from the a/c component of each intensity time curve along the vessel radius is shown in Fig. 11c. The IP was obtained by fitting a cubic spline to the descending edges of the radial optical power curve, and then finding the location of the zero second derivatives. Under control conditions with FITC, the distance between the IP and plasma membrane of the EC averaged 0.90 μm, as summarized in Table 7. In contrast, the distance from the edge of the core of RBCs to the EC averaged 1.77 μm, as obtained from brightfield images of each venule. In all cases studied, the IP was typically

on the order of 1 μm from the EC and half-way between the edge of the RBC core and EC.

The radial distribution of VTT(r) is shown in Fig. 11d for this representative venule. Within the central region of the vessel (for $r/R < 0.8$) VTT remained fairly flat across the entire core region, possibly as a result of the blunted velocity profile. The VTT value increased dramatically when approaching the wall, primarily due to the reduction of velocity near the wall and attains a maximum value at the wall. Because of the noise level in the value of VTT(R), it was difficult to consistently identify a near wall value of VTT for analysis of dye transport through the glycocalyx. As shown in Table 5, values of VTT extrapolated to the wall ($r = R$), did not show a significant change between control and fMLP treatments. In contrast, however, the slope of VTT(r) between the IP of the optical power and the wall ($\Delta VTT/\Delta r$) gave a consistent measure of the behavior of VTT near the wall, obtained by linear regression of the computed VTT(r) vs. r, as shown by the dashed lines in Fig. 11d. For all 156 measurements made, linear regressions of VTT near the wall had an average correlation coefficient (r) of 0.89 ± 0.07 SD with RMS errors less than 5% (Table 3) and each regression slope was statistically significant (t-test, $p < 0.05$).

Before $\Delta VTT/\Delta r$ was used to reflect the relationship between the glycocalyx and on the solute transport, several other parameters were explored. Beside IP, another characteristic spatial point can be obtained by linearly extrapolating VTT to zero from the IP based on the slope of OP(r) at IP, defined as the extrapolated point (EP). The location of the EP is determined by the value of optical power and the slope at the IP. In theory, it is less influenced by the uneven endothelial surface. The average distance between IP and

EP, shown in Fig. 12, is on the order of 1 μm. Significant difference was observed between FITC and FITC-Dx70, but not between control and fMLP. Difference in transit time between IP and EP, VTT_{EP}-VTT_{IP}, reflects the retardation of the glycocalyx structure between the two points. Fig. 13A and B showed the VTT difference normalized by VTT at IP and VTT at centerline, $(VTT_{EP}$-$VTT_{IP})/VTT_{IP}$ and $(VTT_{EP}$-$VTT_{IP})/VTT_{CL}$ respectively. Post-fMLP, both parameter decreased significantly for FITC, but not for FITC-Dx70, possibly due to the inability of FITC-Dx70 in penetrating the glycocalyx. The post- to pre-fMLP ratio of the VTT difference, $(VTT_{EP}$-$VTT_{IP})_{fMLP}/(VTT_{EP}$-$VTT_{IP})_{Control}$ as in Fig. 13C, is significantly different between FITC and FITC-Dx70, between which the ratio for FITC is significantly less than 1, but not for FITC-Dx70. At last, the centerline velocity corrected VTT difference, $(VTT_{EP}$-$VTT_{IP})\cdot V$ was plotted in Fig. 13D. One observed significant drops in both FITC and FITC-Dx70, and also significant difference between control values of FITC and FITC-Dx70.

The parameter ΔVTT/Δr was chosen after comparing with these four parameters to represent the experimental observations, because it provides the strongest signal for FITC after treatment of fMLP, and no signal for FITC-Dx70, that fits the theoretic expectations.

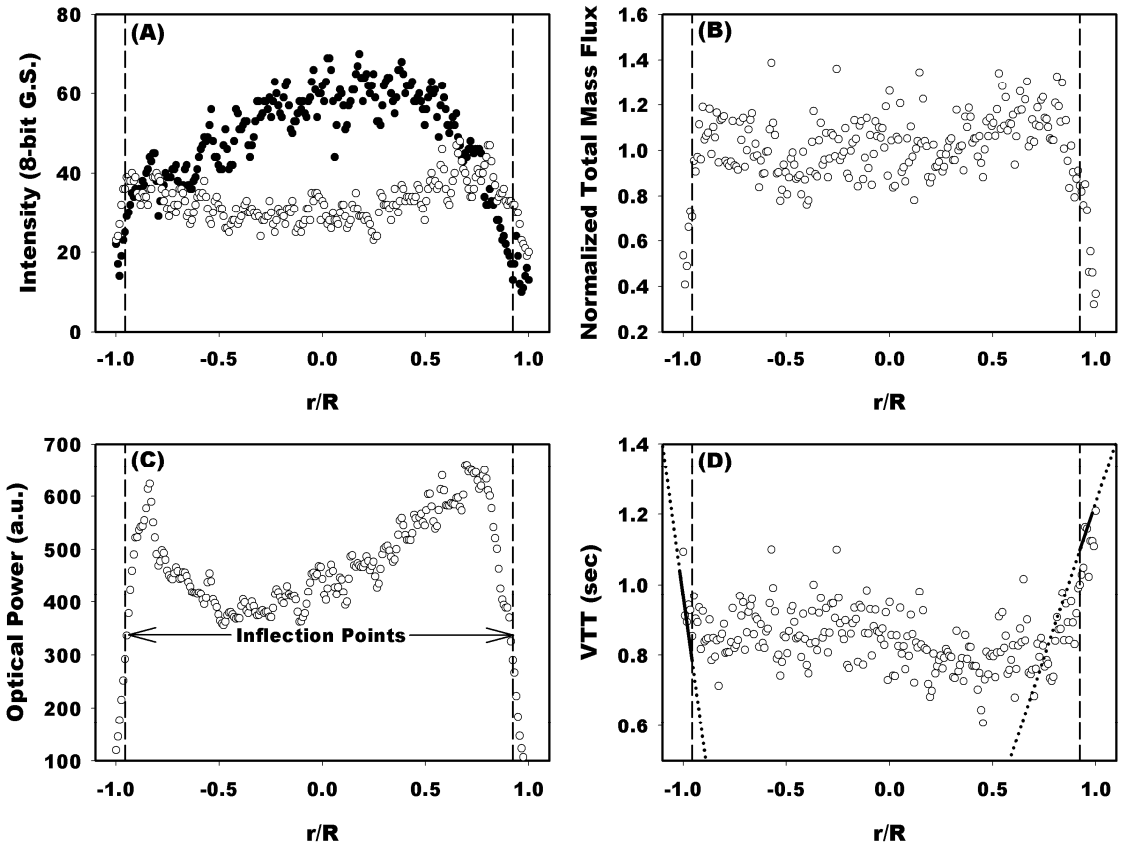

Figure 11: Representative experimental results extracted from the data of Fig. 3. (a) Radial distributions of fluorescent intensity when the centerline reaches its maximum (●) and when the near wall value attains its maximum (○). (b) Radial distribution of total mass flux ($\int I(t)\,dt$) normalized with respect to its centerline value. (c) Distribution of optical power calculated from the AC component of the intensity–time curve. The inflection point of optical power near the wall (dashed line shown in each panel) was taken as the boundary of a region containing the glycocalyx. (d) Radial profile of the calculated virtual transit time (VTT(r)). VTT has a uniformly low centerline value and rises rapidly from the inflection point to the wall (r/R = 1). The slope of VTT was determined by linear regression between the inflection point and vessel wall (shown in panel d as a solid line between the inflection point and wall, and dotted line beyond).

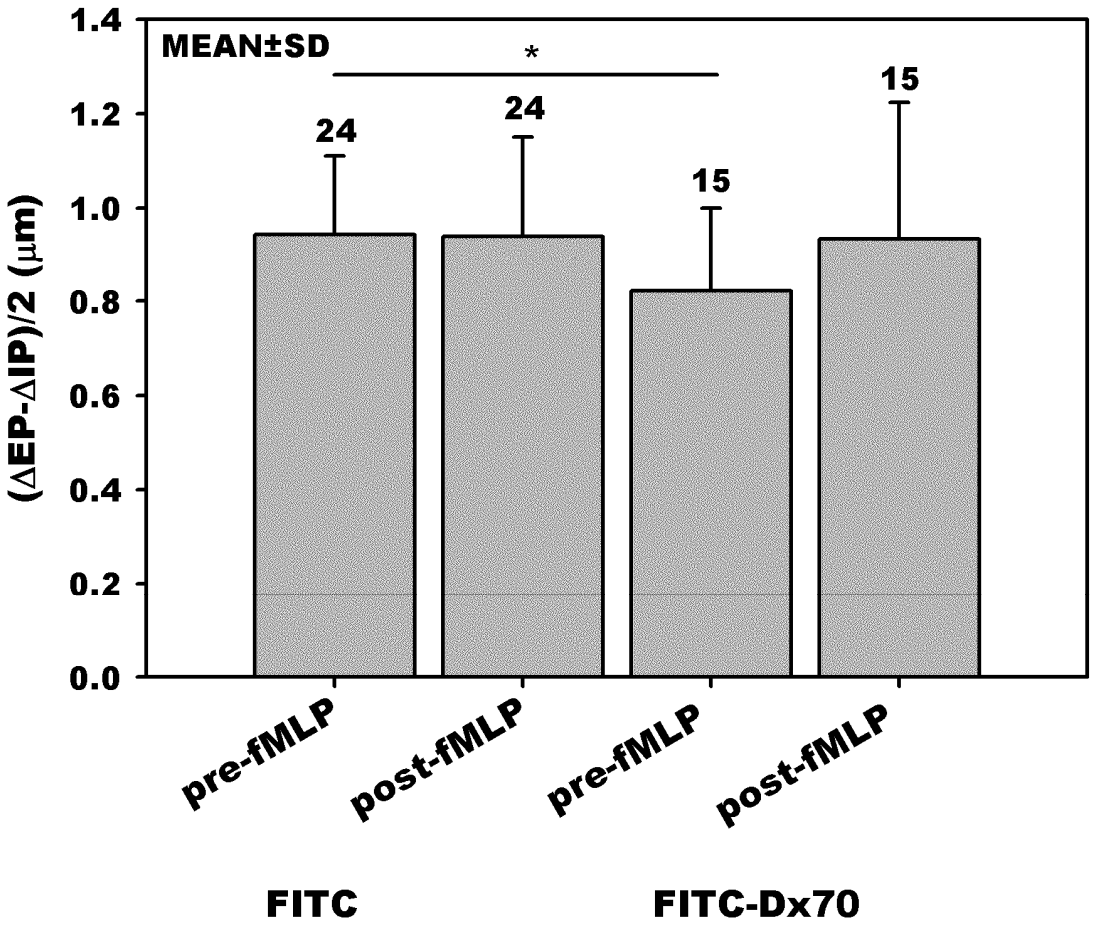

Figure 12: The average distance between IP and EP, compared between pre- (control) and post-fMLP, for FITC and FITC-Dx70 boli. Significant difference was observed between FITC and FITC-Dx70 for control condition ($p < 0.05$).

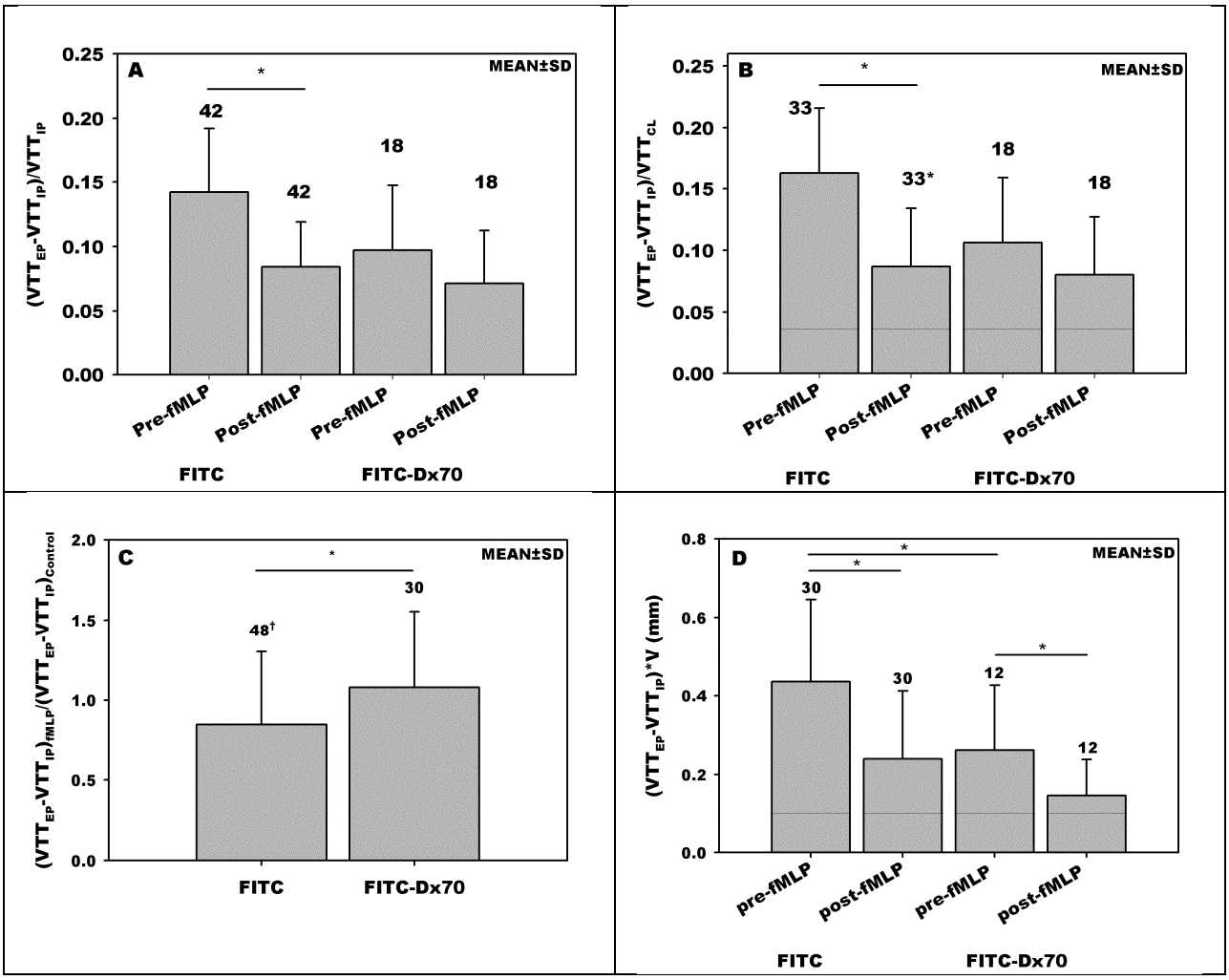

Figure 13: Difference in the virtual transit time between IP and EP, (VTT_{EP}-VTT_{IP}), was explored in four parameters. A, VTT_{IP}-normalized, B, VTT_{CL}-normalized, C, ratio of fMLP-treated to control, and D, mean RBC velocity corrected. * Statistical significance between two groups at either end of the corresponding horizontal line. † Statistically significant difference from 1. ($p < 0.05$.)

Measurements of the slope of the virtual transit time (ΔVTT/Δr) for two different size solutes, FITC and FITC-Dx70, are shown in Fig. 14 for 9 and 5 venules, respectively, prior to and following superfusion of the tissue with fMLP. The number of bolus infusions is given in Fig. 14, and statistics on venule diameters and mean RBC velocity are presented in Table 6. For FITC, ΔVTT/Δr fell significantly from 0.23 ± 0.08 SD to 0.18 ± 0.09 SD s/μm following fMLP (t-test, $p < 0.05$) presumably due to shedding of components of the glycocalyx. In contrast, ΔVTT/Δr for the Dx70 was significantly less than that for FITC and was not affected by shedding of the glycocalyx, thus suggesting that the larger Dx70 did not penetrate the glycocalyx significantly as the bolus traversed the venule. Statistical analysis of these data on a per vessel basis (i.e. 9 and 5 venules for FITC and Dx70, respectively) using average values of ΔVTT/Δr for each venule, revealed similar results. Values of DVTT/Dr are not affected by size of the vessel, as shown in Fig. 15. Due to variations in the 3-D shape of the vessel, its planar orientation (vessels were not always strictly horizontal), heterogeneity of the glycocalyx along the length of a venule, and the limitations in optical resolution, it was virtually impossible to perform repeated measurements at the same location. Hence, the statistical analysis was performed on the basis of the total number of measurements and each measurement was weighted individually.

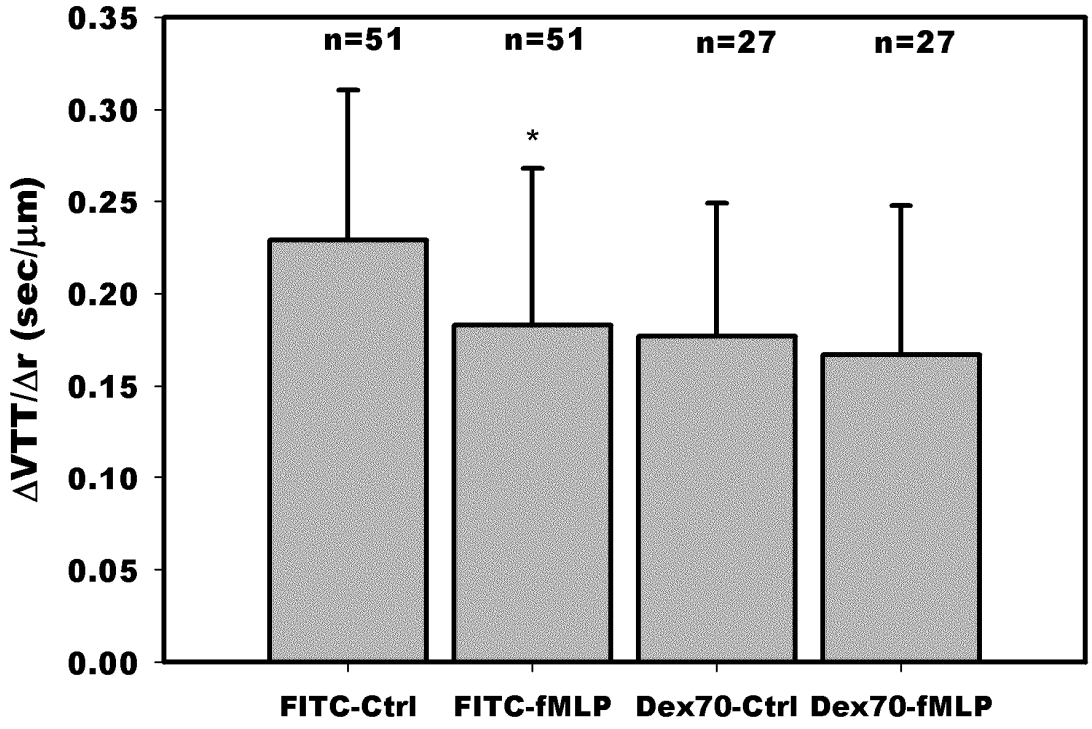

Figure 14: Comparison of slopes of the measured VTT(r), ΔVTT/Δr, for dispersion of FITC and FITC-Dextran 70 during superfusion of the mesentery under control conditions (Ringer's solution) and with 10^{-7} M fMLP-Ringer's solution (fMLP). For FITC, ΔVTT/Δr decreased significantly from 0.23±0.08 SD to 0.18±0.09 SD sec/μm following fMLP superfusion, *$p<0.05$. For boli of FITC-Dextran-70 ΔVTT/Δr did not change significantly, from control to fMLP and averaged 0.18±0.07 SD and 0.17±0.08 SD sec/μm, respectively. The number of measurements (n) is shown for multiple boli in 9 venules.

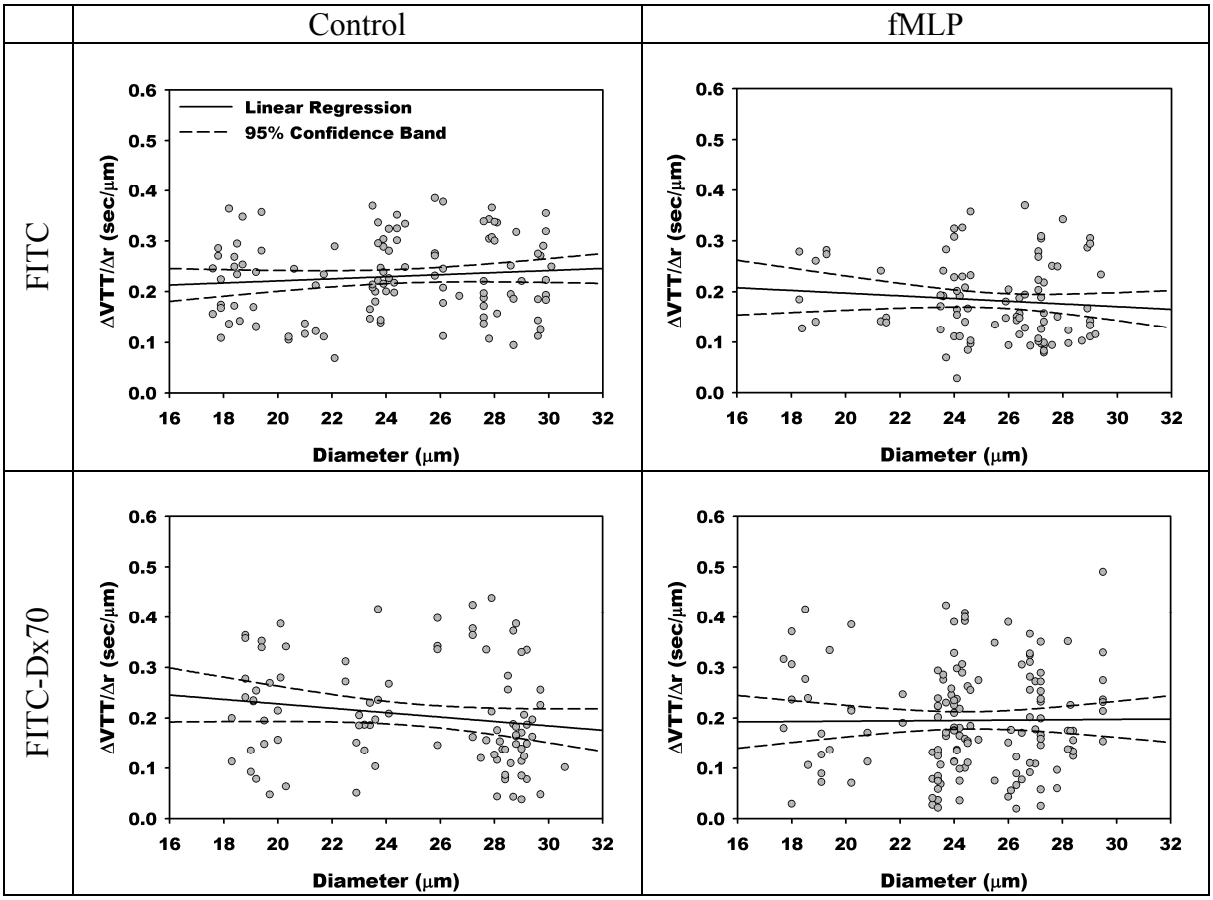

Figure 15: Linear regression of ΔVTT/Δr versus the vessel diameter. No significant correlations were found between ΔVTT/Δr and the diameter for all cases. Probabilities of the slope for control and fMLP are p = 0.25, 0.33 for FITC and p = 0.11, and 0.90 for FITC-Dx70, respectively.

3.2 Simulation of the bolus and VTT

Results of a representative simulation of transmission of a bolus of small solutes through a tube are presented in Fig. 16. The simulation was performed using in vivo intensity–time curves averaged over five radial pixels on the centerline of a venule and applied uniformly across the entrance of the tube (shown in inset of Fig. 16, with specified values of δ, D_{eff} and K_r. For this simulation, the thickness of the glycocalyx was assumed to be 5% of the vessel radius, which for a 30 μm vessel would correspond to $\delta =$ 0.8 μm. As in the case of the experimental measurements, a progressive delay of the intensity time curve is indicated by a delayed peak and prolonged tail in the indicator concentration vs time curve at the wall ($r/R = 1$).

Illustrated in Fig. 17 are the radial distributions of the computed solute concentration (panel a), normalized total (cumulative) mass flux (panel b), optical power (panel c) and virtual transit time (VTT) (panel d). All four distributions reveal trends similar to those acquired *in vivo* (Fig. 4), with slight differences due to the absence of discrete RBC's in the simulation. The simulated total mass flux (Fig. 17b) appears much more parabolic compared with the in vivo measurements (Fig. 11b) because the light scattering by RBCs attenuates the fluorescence excitation and emission and thus disrupts the proportionality between light intensity and dye concentration. In contrast, measurements of fluorescence emission are affected less within the plasma layer and glycocalyx. It should be noted that light scattering effects become accentuated with high numerical aperture objectives (needed for higher spatial resolution) and play a lesser role

with lower magnification-numerical aperture objectives (McKay and Lipowsky, 1988). The vertical dashed lines in each panel represent the radial location of the inflection point in the optical power distribution (panel c). In all simulations, the inflection point occurred between the EC and edge of the RBC core (r_c), and was typically within ±6% of r_c, for assumed thicknesses ranging from 100 nm to 1 μm. The radial distribution of VTT(r) falls rapidly within the layer bounded by the RBC core with its maximum slope at the inflection point. Near the wall (r/R = 1), VTT(r) approaches a constant value as dVTT(r)/dr approaches 0. As suggested by Eq. 1, the slope of c(r) and dVTT/dr approach zero near the wall to reflect zero radial mass transfer ($\partial c/\partial r = 0$). Thus, in light of the bounded nature of the slope of VTT(r) within the plasma layer, its absolute value was used as an indicator of the behavior of VTT(r) and transit of solutes through the glycocalyx.

Parametric numerical simulations corresponding to the three independent variables, δ, K_r and D_{eff} were performed to describe the variation of ΔVTT/Δr over a range that includes its measured values, as shown in Fig. 18. Each panel corresponds to the indicated thickness of the glycocalyx (δ) and shows a set of parametric curves for a range of values in D_{eff} normalized with respect to the free diffusion coefficient of FITC. In each case, the variation of DVTT/Dr was relatively insensitive to large variations in K_r for $10^5 < K_r < 10^{14}$ dyn·s/cm^4 (shown only up to 10^{10} for clarity). Most strikingly, in order to approach a range of ΔVTT/Δr similar to in vivo measurements, values of D_{eff} on the order of 0.003% of D_{free} were required for a 100 nm thick glycocalyx and 0.5% of D_{free}

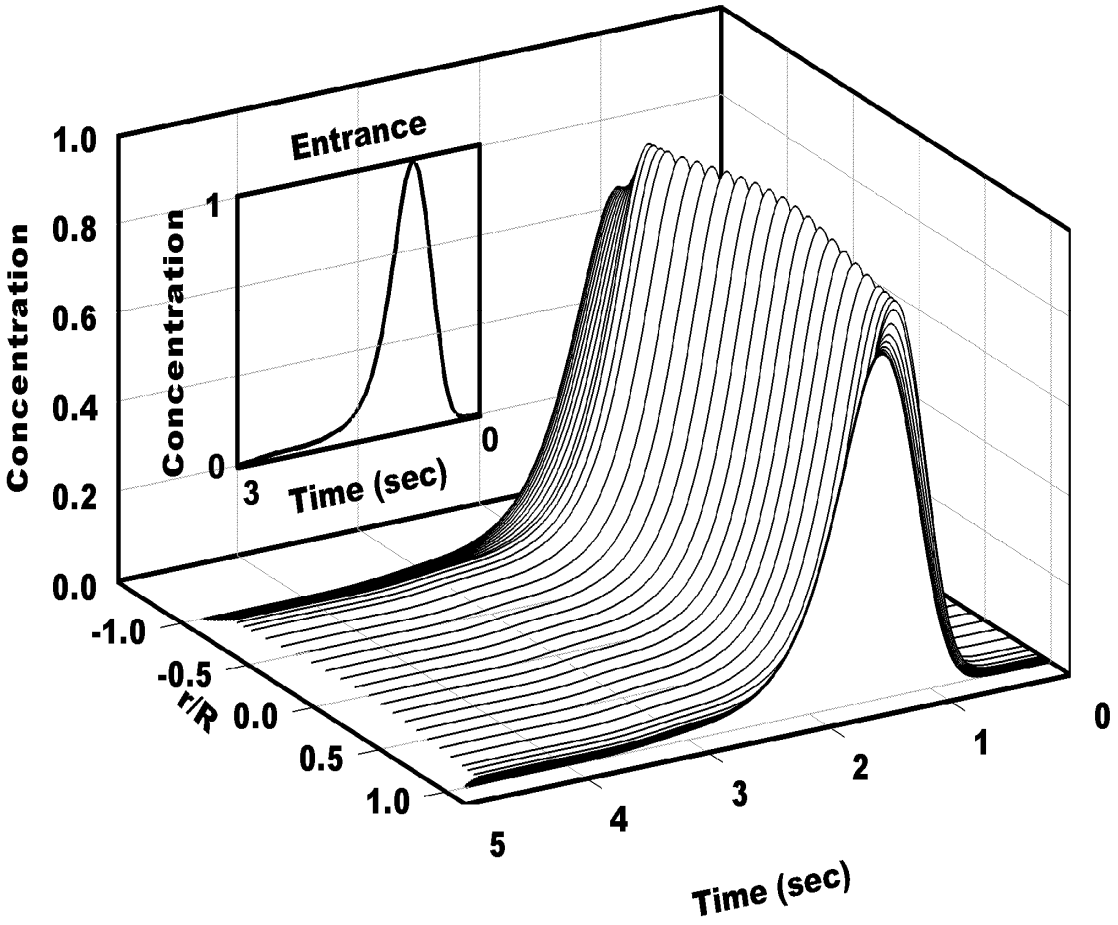

Figure 16: Computer simulation of dispersion of a bolus of solutes at 30 vessel diameters downstream of the entrance of a 30 μm diameter venule resulting from a specified concentration-time curve at the entrance (inset) taken from *in vivo* measurements. Shown are solute concentration-time (normalized by centerline values) curves over radius. The red cell core was assumed to be 1.7 μm from the vessel wall, the glycocalyx was 0.8 μm thick, the effective diffusion coefficient $D_{eff} = 0.2\times10^{-8}$ cm^2/sec and the hydraulic resistivity $K_r = 10^{10}$ dyn·sec/cm^4. The simulation replicates the gross features of the *in vivo* measurements, as evidenced by the attenuated and delayed peak concentration within the glycocalyx.

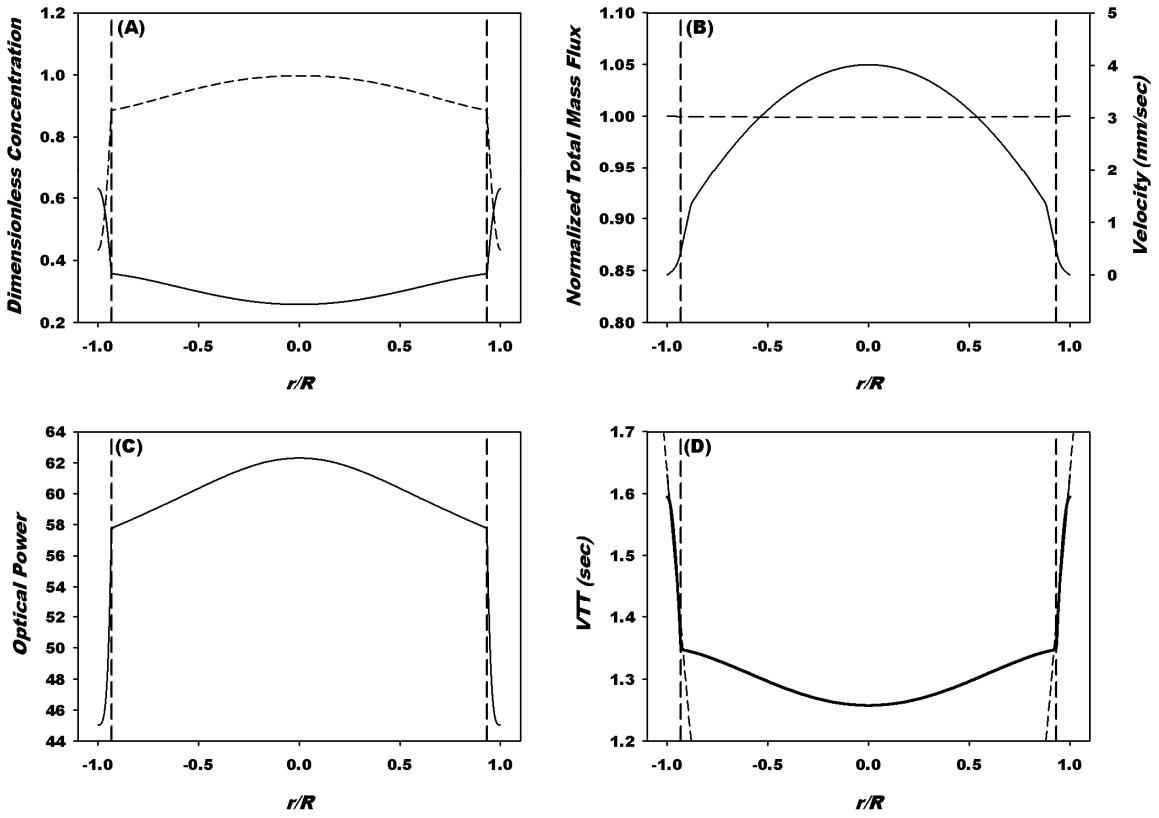

Figure 17: Radial distribution of parameters for the simulated bolus transport shown in Fig 8. Two vertical dashed lines in each panel indicate the location of the inflection point in the optical power. (A) Radial distribution of dimensionless concentration of the indicator molecule. The dash line corresponds to the time when centerline concentration attains its maximum value, and the solid line refers to the time when the near-wall layer reaches its maximum. (B) Centerline-normalized total mass flux (dashed line) and velocity profile (solid line). The velocity begins to fall off sharply at the boundary of the red cell core with increasing r/R, and reveals an inflection point within the glycocalyx at $\approx \delta/2$. (C) Radial distribution of the optical power. (D) VTT(r), where linear regression lines in the region 1-μm from the wall (solid line, extended with dash lines) were used to obtain the slope $\Delta VTT(r)/\Delta r$. These results are consistent with the *in vivo* measurements, although the location of the inflection point for the optical power occurs within ±6% of the location of edge of the red cell core.

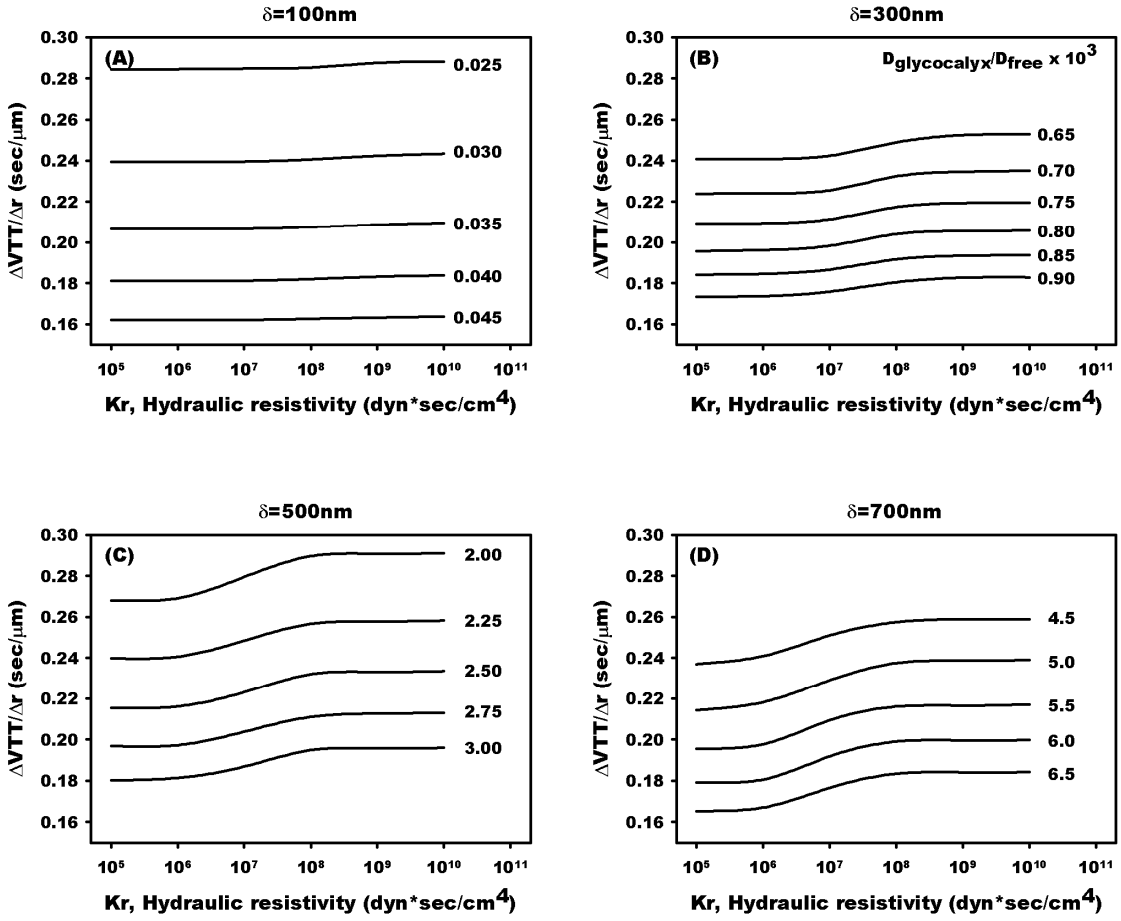

Figure 18: Parametric plots derived from the computer simulations illustrating the slope ΔVTT/Δr as a function of hydraulic resistivity of the glycocalyx (K_r) for specified values of the effective diffusion coefficient ($D_{glycocalyx}/D_{free}$) of a small solute in the surface layer, for four thicknesses of the glycocalyx. The slope of VTT is relatively constant over the indicated range of K_r and is much more sensitive to diffusion coefficient within the glycocalyx of a given thickness.

for a 700 nm thick glycocalyx. Thus, the thinner the glycocalyx, the greater the reduction in the effective diffusion coefficient must be in order to slow down the movement of solutes through the layer to yield the indicated slope of VTT near the wall.

Simulations corresponding to control and fMLP values of ΔVTT/Δr are presented in Fig. 19 for four specific thicknesses of the glycocalyx ranging from 100 to 700 nm. These computations illustrate the possible range of concurrent changes in D_{eff} and K_r that would result in the measured change in ΔVTT/Δr for a given thickness. For example, given a nominal thickness of 500 nm (Fig. 19c) the response to fMLP would be typified by moving from one point on the lower (solid) curve to a point on the upper (dashed) curve. Assuming that structural elements of the glycocalyx are lost due to enzymatic shedding, it would appear logical to envisage a reduction in K_r from, for example, its maximum value of 10^{10} dyn·s/cm^2 to as low 10^5 dyn·s/ cm^2 with an attendant increase in D_{eff} from 2.5×10^3 to about 2.9×10^3 times the free diffusion coefficient, i.e. a 15% increase in D_{eff}. If K_r remains constant at 10^{10} dyn·s/cm^2 in response to fMLP, then the solution could be obtained with roughly a 10% greater increase in D_{eff} from 2.5 to $3.2 \times 10^3 \times D_{free}$. Thus, one may conclude that very small changes in the ability of the solute to diffuse through the glycocalyx have the greatest impact on its transport.

Simulation results as shown in Fig. 20 also indicated that large variations of the bulk velocity of blood flow (from 1 to 10 mm/s) has only a small effect (< 0.15%) on ΔVTT/Δr, indicating that the near-wall velocity rather than core velocity affects transport through the glycocalyx layer.

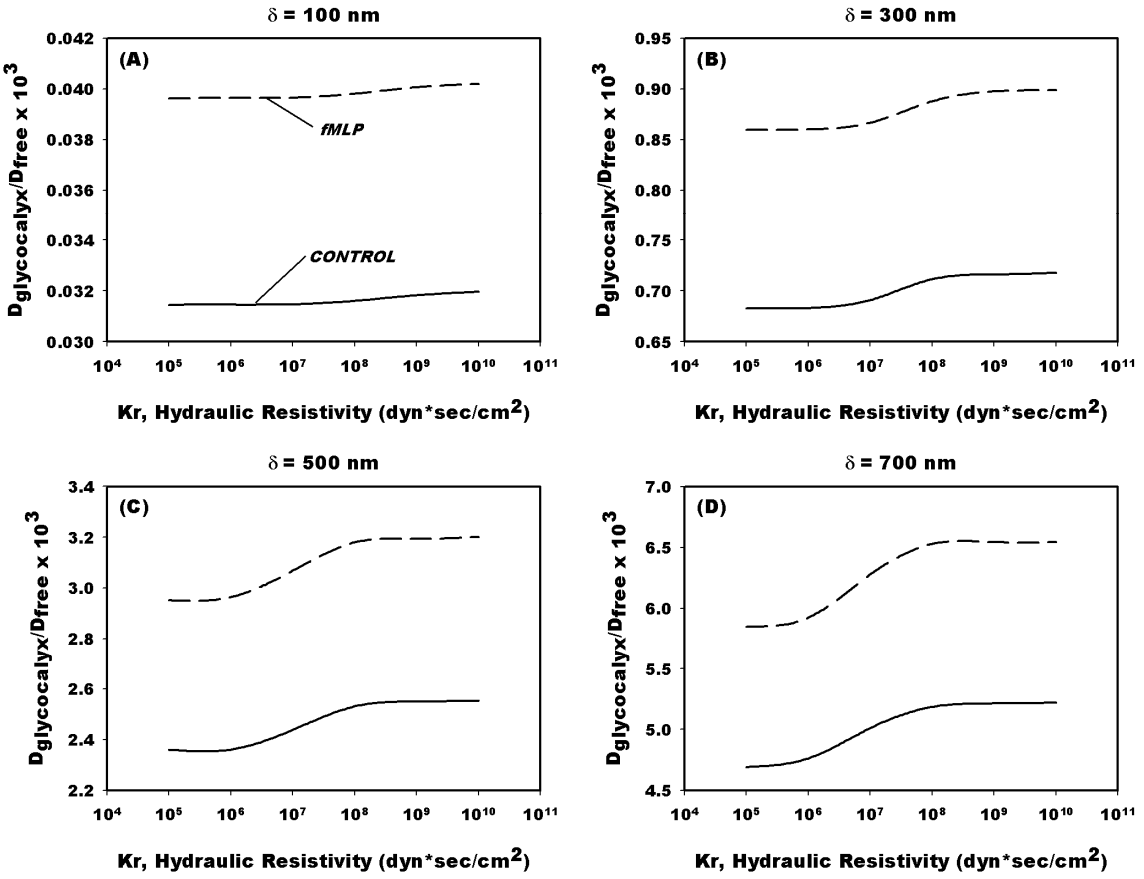

Figure 19: Simulations representing curves of constant ΔVTT/Δr for control (solid line) and fMLP (dashed line) treatments (FITC, Fig. 14) for four assumed thicknesses of the glycocalyx: 100nm, 300nm, 500nm and 700nm. Radial diffusion of the solute through the glycocalyx has the greatest effect on the slope of the virtual transit time at the wall and dominates changes in response to superfusion with fMLP.

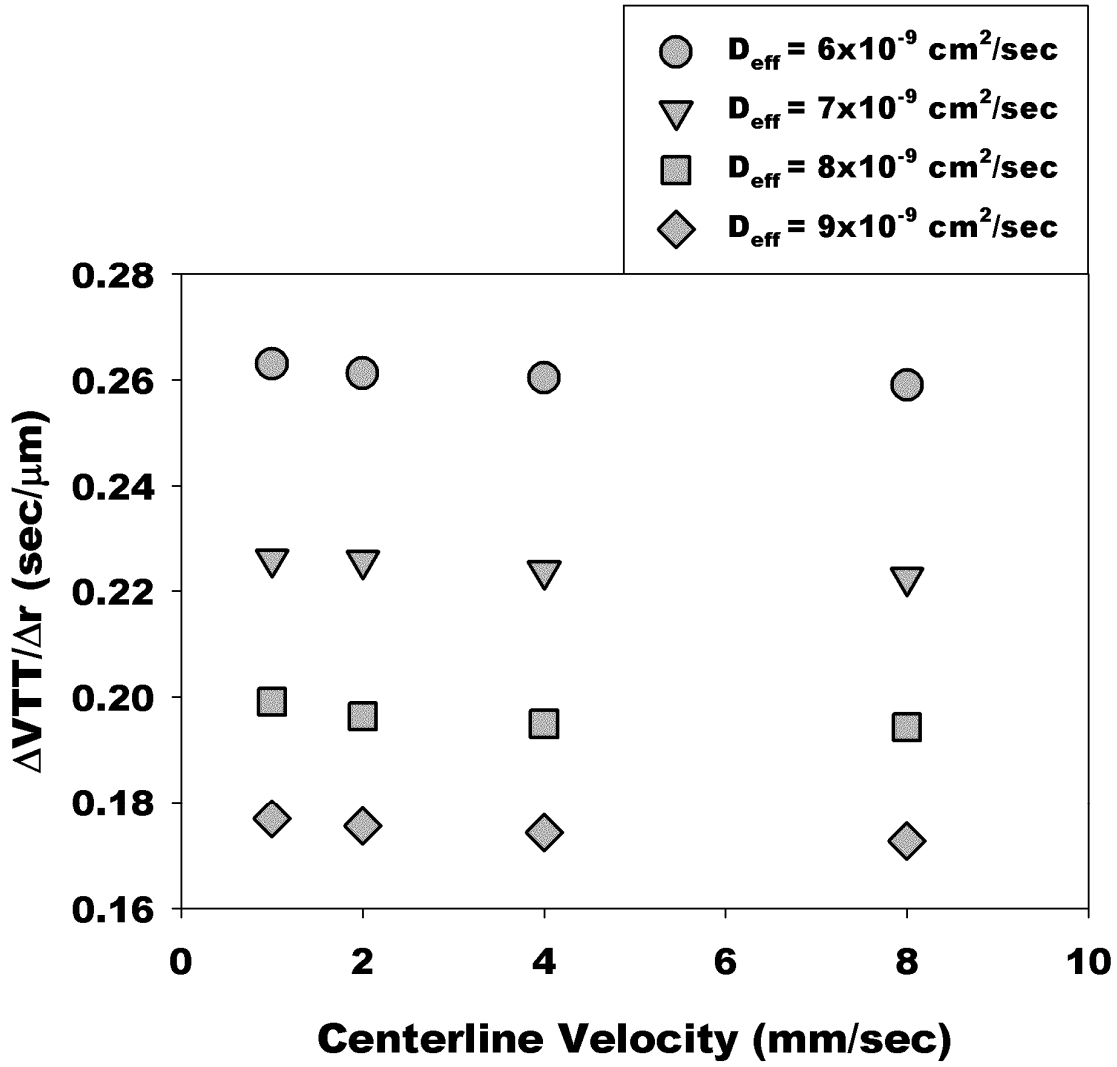

Figure 20: The effects of the centerline velocity on ΔVTT/Δr. The simulation results were presented for four different effective diffusion coefficients of the FITC in the glycocalyx layer with the thickness 500 nm and hydraulic resistivity $K_r = 1 \times 10^{12}$ dyn·sec/cm^2 of a 30-μm diameter vessel.

3.3 Discussion

3.3.1 The Indicator Dilution Principle in a Single Vessel

The present study has employed a variant of the indicator dilution technique to probe for changes in the endothelial glycocalyx during a model inflammatory response in post-capillary venules. The dispersion of solutes flowing through a uniform tube of circular cross-section is a classic problem that has been extensively studied since the seminal studies of Sir Geoffrey Taylor (Taylor, 1953). As shown therein, the axial dispersion of a bolus of solute in steady flow is dependent upon convective transport parallel to the axis of the tube and molecular diffusion in the radial direction. The relative contributions of convection and diffusion in affecting indicator dispersion have been characterized mathematically by Taylor (Taylor, 1953; Taylor, 1954). Given a vessel of length L and radius a, and a steady flow with mean velocity U, radial diffusion of a solute with diffusion coefficient D will dominate convection when $L/U \gg 2a^2/3.8^2D$ (Taylor's condition B). Given values typical of postcapillary venules (L = 0.5 mm, U = 1 mm/s, a = 0.015 mm, D_{FITC} = 2.7 × 10^{-4} mm^2/s) values for these terms are 0.5 and 0.12 s, respectively. Thus, for an idealized uniform fluid devoid of blood cells the dispersion of a bolus of FITC would depend upon both diffusion and the mean velocity of flow. However, in the case of in vivo microvessels, it is well recognized that the presence of RBCs in the central core enhances mixing of plasma borne solutes and results in an effective diffusion coefficient that is much greater than in a quiescent solvent (Spaeth and Friedlander, 1967). Studies of the transit time of fluorescent macromolecules and red cells through successive branches of the microvasculature have revealed that mixing

within the central core of RBCs occurs rapidly and that the Stewart–Hamilton relationship can be used to give a realistic measure of mean transit time of fluorescently tagged RBCs and plasma that is consistent with the average Fahraeus effect within a microvascular network (Lipowsky et al., 1993).

The use of first moment of indicator concentration as a probe for the speed with which solutes negotiate the glycocalyx departs from the traditional Stewart–Hamilton approach. A discrete reference for the injection time and assurance of conservation of the mass of indicator were not used. Instead, the VTT was based upon the total concentration of indicator passing through the observation site with both integrals in Eq. (1) ranging from the time of first appearance of the indicator in the RBC core to its full duration. In the context of the Stewart–Hamilton approach, the first moment corresponds to the mean value of the indicator which exhibits a temporal distribution that represents the frequency distribution of transit times through all pathways taken by the indicator from injection to observation sites (MEIER and ZIERLER, 1954). In the current approach VTT corresponds to the time weighted average of the observed indicator, normalized with respect to the total indicator passing through the observation site. Attempts to use higher moments, such as the second moment, indicative of the variance of the indicator, were confounded by noise inherent to the low amplitude signals near the microvessel wall and therefore were not productive. The numerical simulations (Fig. 16. 17, 18 and 19) provide evidence that the slope (dVTT/dr) at the wall was sensitive to the diffusion coefficient (D_{eff}) and hydraulic resistance (K_r) in the glycocalyx.

Simulations of indicator dispersion under conditions similar to those observed *in vivo* revealed that the effective diffusion coefficient within the core does not significantly

affect dispersion of the indicator within the plasma layer. Namely, variation of the slope of the virtual transit time VTT(r), at the wall, reveals that it is insensitive to the magnitude of D_{eff} within the RBC core and depends mainly on D_{eff} within the plasma layer and glycocalyx. Hence, to gain insight into the behavior of ΔVTT/Δr with D_{eff}, K_r and δ, the numerical simulations were performed for mean bulk velocities and vessel geometries similar to those observed *in situ*.

3.3.2 Changes in the Thickness, Permeability and Diffusion Coefficient

Using numerical simulations to interpret the in vivo response to the fMLP model of inflammation, suggests that changes in K_r have a lesser effect compared to D_{eff} or d, as indicated by the simulations shown in Fig. 16. 17, 18 and 19. The relative insensitivity of ΔVTT/Δr to K_r suggests that the in vivo measurements may be much more sensitive to the diffusion of solutes through the layer in the radial direction. Although structural and composition changes in the glycocalyx may affect K_r, it appears that restrictive flow of the solvent is not sufficient to impede the diffusional transport of small solutes through the glycocalyx. These results are summarized in Fig. 21, where parametric curves are shown for the calculated decrease in d (nm) required for the measured changes in ΔVTT/Δr from control to fMLP treatments. As indicated, for low values of D_{eff}, a small 10–20 nm decrease in d is needed over a broad range of K_r. That is, the more compact the glycocalyx, with greater restriction of the diffusion of solutes as pathways become narrower compared to the size of the solute, then the more sensitive the solution becomes

to small reductions in the total thickness. In contrast, for a relatively less compact glycocalyx, with greater diffusivity of solutes, a greater reduction in thickness of the layer is required to affect the change in $\Delta VTT/\Delta r$.

3.3.3 Implication on the correlation of L_p, K_r and D_{eff}

To date, in vivo studies of the transvascular exchange of fluid have been unable to separate the dynamics of hydraulic permeability between the glycocalyx and its accompanying endothelial and tissue barrier, except by physically modifying the endothelial surface layer to observe changes in the radial permeability to fluid, L_p.2 The current approach affords the opportunity to characterize permeability of the glycocalyx in the radial direction without the influence of the endothelial barrier itself. In general, the hydraulic permeability of the glycocalyx in radial and axial directions may be related by drawing upon the definition of L_p which is defined as the solvent flux per unit area, Jv/A, divided by the pressure drop, i.e. $L_p = Jv/A \cdot \Delta P$.14 Upon consideration of conservation of momentum from Eq. (3) for an average flow parallel to the vessel wall within the glycocalyx with $\partial u / \partial r = 0$ then for equivalent pressure gradients in radial and axial directions, $L_p K_r \delta = 1$. Assuming that the hydraulic resistivity in axial and radial directions are equal, i.e. that the glycocalyx is isotropic, the values of K_r spanned in the present simulations (Fig. 18, 19, and 21) bracket experimental measurements suggested by in

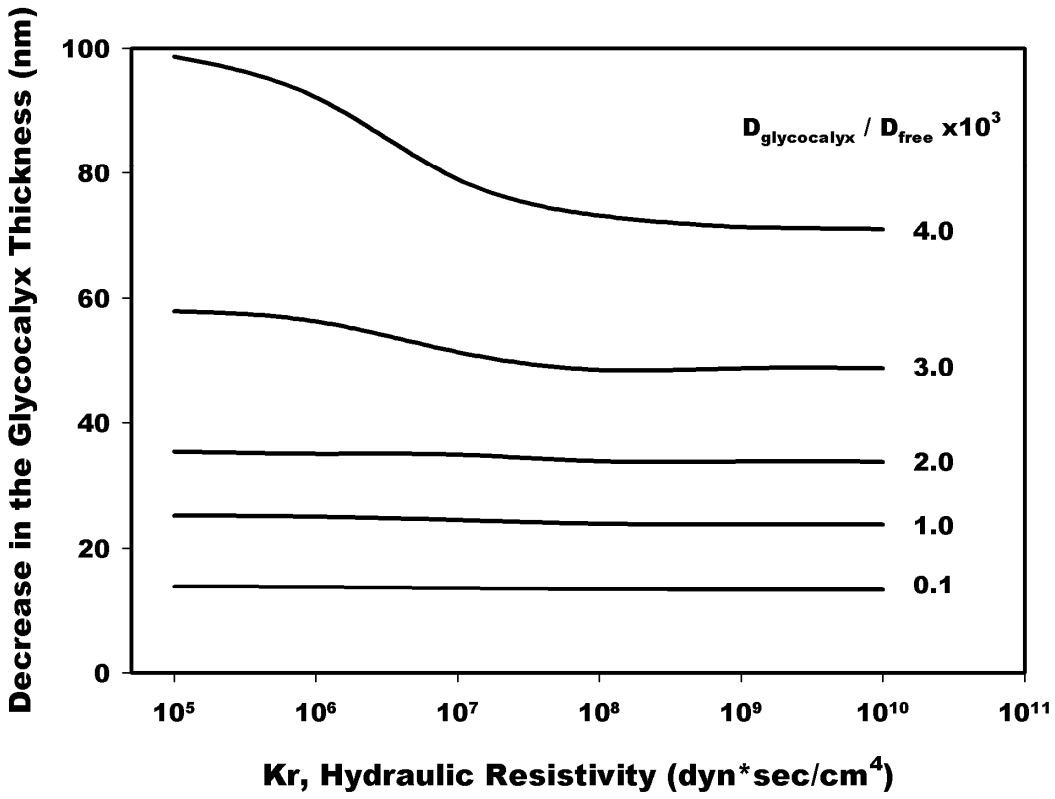

Figure 21: Calculated decrease in thickness of the glycocalyx (δ) required to produce the increase in ΔVTT/Δr from control to fMLP treatments for a given value of K_r and diffusion coefficient in the glycocalyx. D_{free} is the free diffusion coefficient of FITC in aqueous media. At higher levels of Kr the required decrease in d approaches an asymptote that is dependent on diffusion coefficient in the glycocalyx.

vivo measurements of L_p. For example, for $K_r = 10^5$ dyn·s/cm^4 and $\delta = 100$ nm, and $K_r = 10^{14}$ dyn·s/cm4 and $\delta = 700$ nm, then L_p would range from 10^3 to 10^{-7} cm/s/cmH2O, respectively.

Direct measurement of L_p using the Landis technique in frog capillaries have resulted in a value of 2×10^{-7} cm/s/cmH2O measured in frog mesentery by Adamson (Adamson, 1990). In these experiments, capillaries were perfused with pronase to strip off the glycocalyx resulting in a measurement of L_p equal to 4.9×10^{-7} cm/s/cmH2O. Assuming that the hydraulic resistance is the result of two serial resistive elements (i.e. with resistance = $1/ L_p$) one may calculate L_p for the glycocalyx equal to 3.38×10^{-7} cm/s/cmH2O. Thus, for a thickness $\delta = 500$ nm, in vivo measurements (Adamson, 1990) suggest that $K_r = 5.8 \times 10^{13}$ dyn·s/cm^4. The present simulations suggest that the effect of hydraulic resistance on solute transport reaches an asymptote for $K_r > 10^8$ dyn·s/cm4 in order to attain the measured slope of VTT(r) at the wall (Fig. 10). That is, axial water movement through the glycocalyx has little effect on the diffusion limited transport of small solutes in the radial direction. For $K_r < 10^8$ dyn·s/cm4, with increasing thickness of the layer, the greater the hydraulic resistance in the layer, the larger D_{eff} must be in order to attain a solution that matches experimental measurements of the slope of VTT(r) (Fig. 21). Hence, reductions in the near wall axial fluid flow with increased K_r tend to limit the axial dispersion of small solutes, which parallels Taylor's analysis of dispersion from convection alone (Taylor, 1953).

As shown previously, enzymatic shedding of glycans occurs due to the activation of G-protein coupled receptors on the endothelium (Mulivor and Lipowsky, 2004). These structural changes in the density of proteoglycans and GAGs may serve to increase the

effective pore size through which small solutes can diffuse. The effect of fMLP on the relationship between D_{eff} and K_r for a given δ (Fig. 21) is consistent with direct measurements of L_p in microvessel where it has been shown that L_p is not affected by perfusion of microvessels with fMLP (Zhu et al., 2005). Apparently, the D_{eff} has to increase when K_r increase to keep the same resistance to the transport if assuming a constant thickness. With the application of fMLP, shedding of the glycans likely reduce the thickness or Kr, if not both. In such scenario, the D_{eff} would have to decrease to maintain the L_p. The changes in the thickness and in the diffusion coefficient of the FITC will be elucidated in the following chapter.

Chapter 4

Contributions of Individual GAG to the Barrier Properties

A physiological barrier is one of the most important properties that the glycocalyx layer provides to the vascular endothelium. The glycocalyx layer contributes significantly to the vascular permeability in controlling the efflux of the fluid and blood borne molecules.

4.1 Enzymatic removal of BS1 labeled GAGs

Presented in Figure 22 are ratios of the intensity of the BS1-Alexa stain to its respective control for no stimulus and following enzyme perfusion. The control measurements ($I_{control}$) were taken at a time of 30-40 min following introduction of the BS1, which corresponds to the cumulative elapsed time between labeling, intubation of the venule and 10 min of enzyme perfusion. The fluorescence intensity of BS1-Alexa decreased significantly after perfusion with each enzyme, $p < 0.05$. Under conditions of no stimulus, natural shedding of the glycocalyx components caused the fluorescence to decrease to 89.5±8.0SD % of control in a 40 min period. By comparison, during the same length of time, enzyme perfusion induced significantly greater reductions to: 37.1±7.7SD % with heparinase, 43.0±6.9SD % with chondroitinase and 65.6±7.4SD % with hyaluronidase. Superfusion with 10^{-7} M fMLP superfusion for 10 min resulted a

reduction in intensity to 64.5±7.6SD%. This decrease was consistent with previous studies using BS1-FITC and superfusion with 10^{-7} M fMLP for 10 min (Mulivor and Lipowsky, 2004). Treating the glycocalyx with heparinase or chondroitinase lead to a significantly greater reduction in BS1 label compared with fMLP, but hyaluronidase did not.

In additional, 10-min infusion of neuraminidase was applied to shed possible sialic acid moiety of the GAGs. BS1 labeling intensity was significantly reduced to 66.5±8.4SD %, comparing with 89.5±8.0SD % without application of neuraminidase (Fig. 23, superscript 1). Interestingly, if CS was pre-shed by 10-min perfusion of chondroitinase before BS1 labeling, the neuraminidase failed to induce any significant in BS1 intensity level, 80.7±5.0SD % versus 81.2±8.5SD % without neuraminidase (Fig. 23, superscript 2). The difference in the substrate composition between group 1 and group 2 is that in group 1, BS1 labeled all three GAGs (HS, CS and HA), but in group 2, BS1 labeled only HS and HA after CS was enzymatically shed. This result suggests the importance of chondrotin sulfate to BS1 labeling of the sialic acid on the endothelial GAGs.

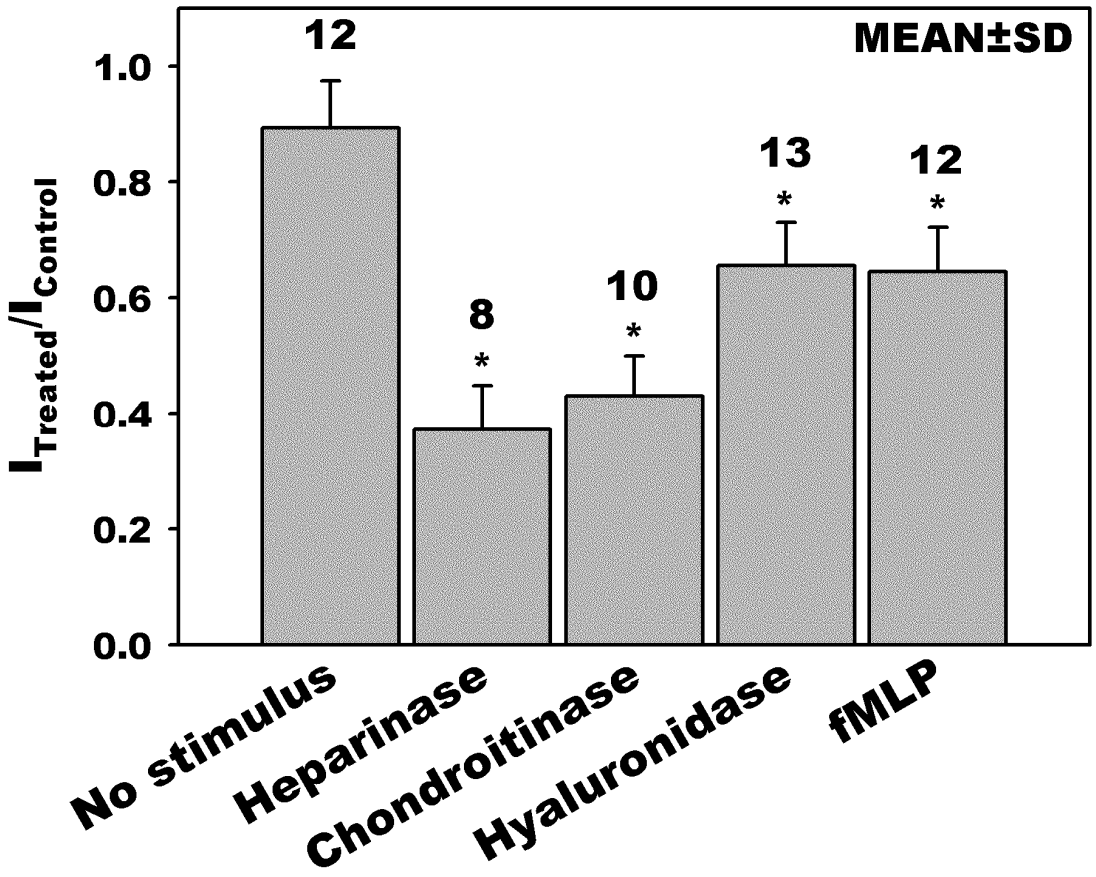

Figure 22: Fluorescence intensity of BS1-Alexa along the endothelial surface of post-capillary venules 30-40 min following proximal infusion of the lectin with a micropipette. Control measurements were taken 10 min prior to each treatment. Intensities were normalized with respect to control, $I_{Treated}/I_{Control}$. Intensity of the fluorescent stain fell 15% with no stimulus, due to natural shedding of glycans. Following 10-min of enzymatic degradation with heparinase, chondroitinase and hyaluronidase, and superfusion of the mesentery with fMLP, glycan labeling was reduced significantly compared to natural shedding (no stimulus), $*p < 0.05$.

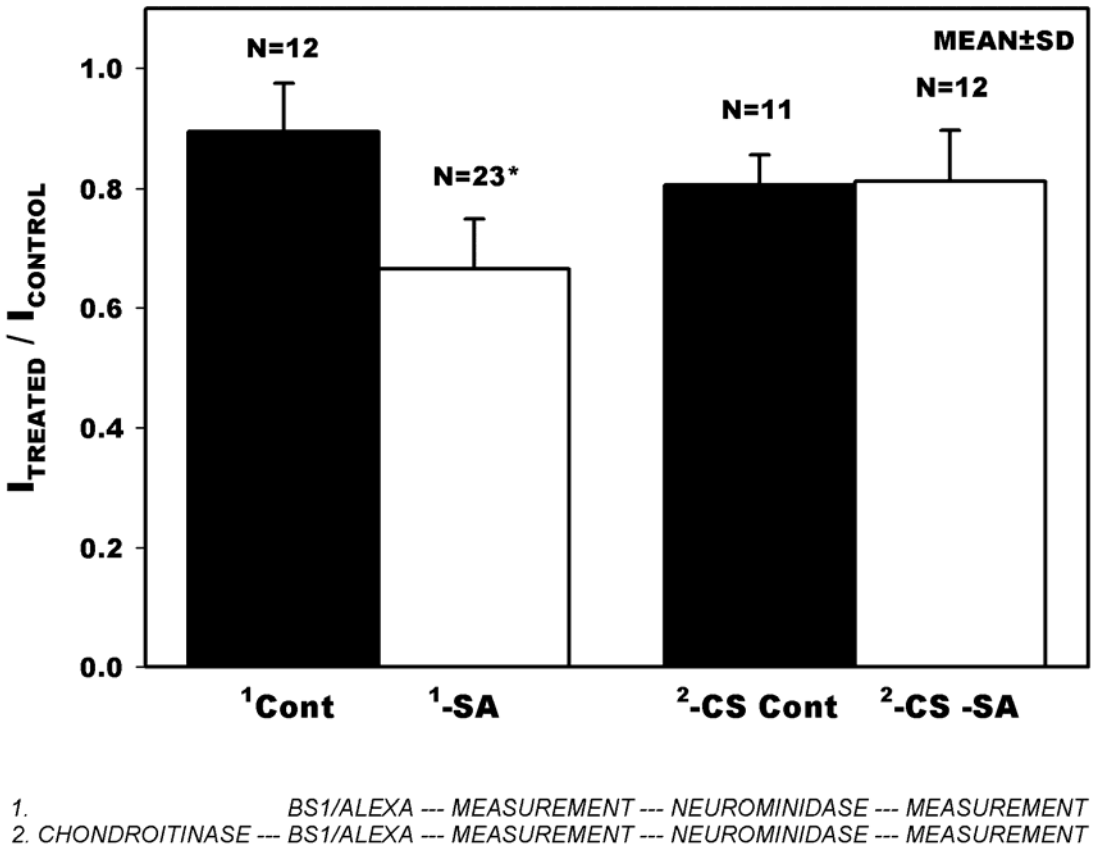

Figure 23: Reduction of the fluorescent intensity of BS1-Alexa pre- and post-neuraminidase shedding of sialic acid from the endothelial glycocalyx on a post-capillary venule with diameter of on the order of 40 μm. Group 1 denotes the BS1 staining of intact GAGs. Group 2 denotes the BS1 staining of GAGs devoid of CS. Significant decrease in BS1 intensity was found in group 1 (*$p < 0.05$) but not in group 2.

4.2 Thickness of the Clycocalyx Barrier

The apparent thickness of the glycocalyx estimated by Dx70 exclusion is shown in Figure 24A for control conditions (no treatment), enzymatic removal of HS, CS and HA and superfusion with fMLP. Under control condition, the Dx70 exclusion thickness averaged 463.1 ± 146.1 SD nm, which was consistent with prior measurements using Dx70 (Vink and Duling, 2000). Enzymatic GAG shedding by heparinase, chondrotinase and hyaluronidase decreased the barrier thickness to 234.0 ± 106.0 SD nm, 285.6 ± 145.2 SD nm and 303.3 ± 165.8 SD nm, respectively. The greater decrease in thickness with heparinase, compared to chondroitinase and hyaluronidase, was not significantly different from the thickness corresponding to these two enzymes. When all three GAGs were removed by a mixture of the three enzymes (same concentration as used individually) the barrier thickness decreased to 51.8 ± 41.3 SD nm.

The fractional decreases in thickness ($\delta_{treated}/\delta_{control}$) are illustrated in Figure 24B. Individually, the reductions in thickness for each enzyme were not significantly different from the 28% reduction incurred by superfusion with fMLP. The mixture of enzymes removed nearly 90% of the barrier thickness, i.e. $\delta_{treated}/\delta_{control} = 0.103 \pm 0.07$ SD.

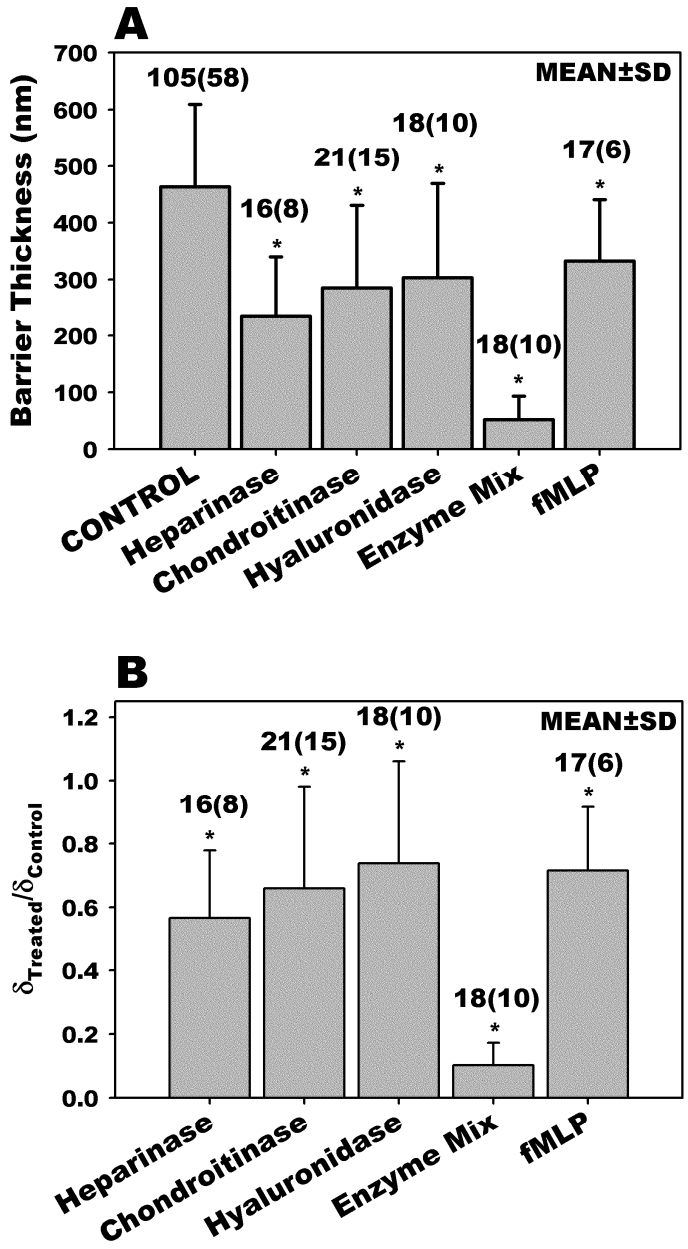

Figure 24: Estimation of the thickness of the glycocalyx from the thickness of the barrier to infiltration of FTIC-Dx70. (A) Thickness measurements taken as the distance between the inflection point in the radial intensity profile at the wall and the EC surface, for control (no perfusion) and micropipette perfusion with the indicated enzymes, and superfusion with fMLP. (B) Ratio of the post to pre-treatment thickness, $\delta_{Treated}/\delta_{Control}$. The number of observations is given along with the number of post-capillary venules (in parenthesis). All treatments caused a significant decrease (*p<0.05) relative to control measurements.

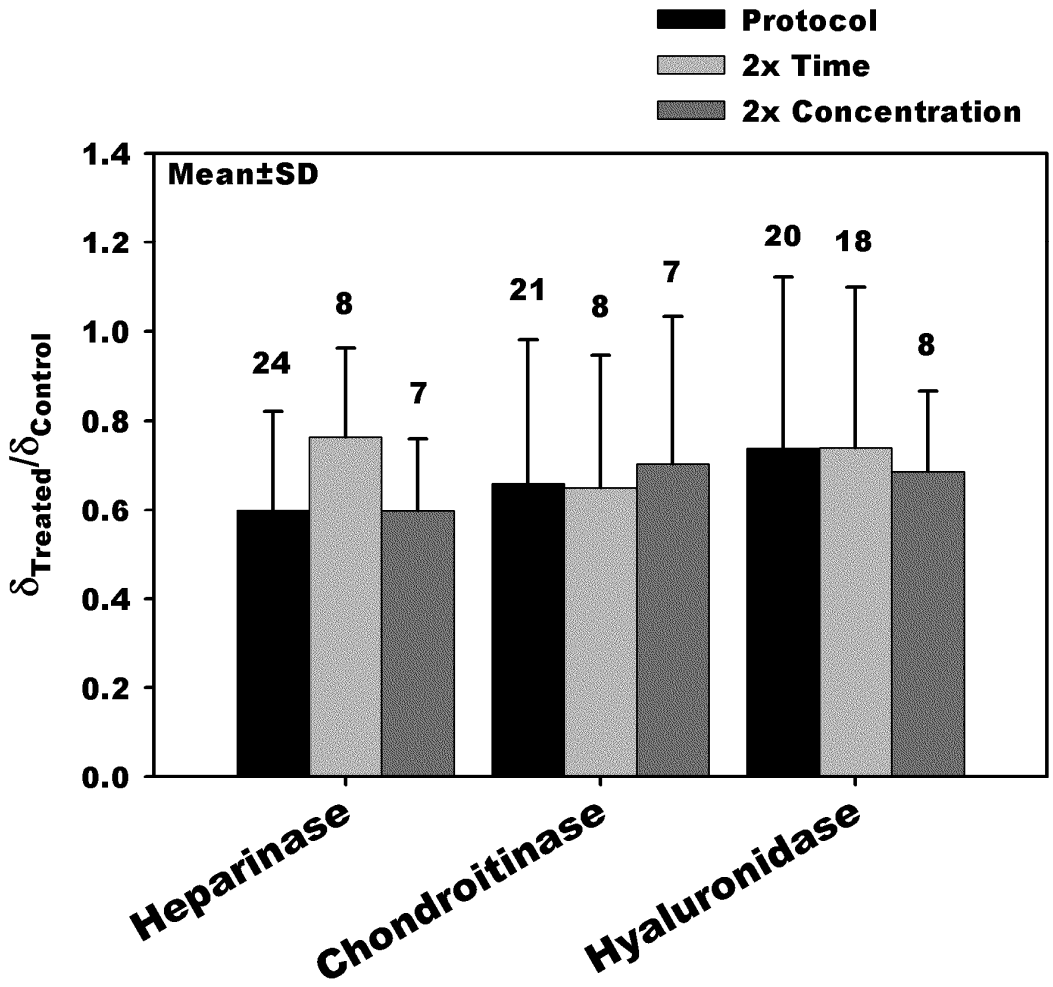

Figure 25: Ratios of post- to pre-thickness of the endothelial glycocalyx following the experimental protocols (50 U/ml, 10 min for heprainase, 10 U/ml, 10 min for chondroitinase, and 3000 U/ml, 10 min for hyaluronidase), doubled infusion time and doubled concentration.

The effectiveness of enzyme treatments was tested by measuring the barrier thickness reduction with doubled perfusion time and doubled concentration of the enzyme solution. As seen in Fig. 25, no significant differences were found by doubling the infusion time or concentration of three enzymes, heparinase, chondroitinase or hyaluronidase. The results ensured exhaustive enzymatic digestion of three GAGs under experimental protocols.

4.3 The Diffusion Coefficient of FITC in the Endothelial Glycocalyx

Typical results for comparison of the computed and measured transient diffusion of FITC into the glycocalyx are shown in Figure 26. The shaded region shows the radial concentration profile with time, computed using the fluorescence intensity-time curve measured at the edge of the glycocalyx (r = 462 nm, control in Figure 26A). The EC luminal surface is at R=0. Measured fluorescence intensities (symbols) agreed with the computational model to within an RMS error of 34.6%. The greatest errors in the fit appear to occur near the wall as the concentration of the FITC accumulates at maximal time, and scattered light or possible dye leakage through the wall interferes with the measurements. In this example, the best fit solution was obtained for a diffusion coefficient of 2.61×10^{-9} cm^2/s.

To explore the heterogeneity of the glycocalyx structure, two different boundary conditions were employed for calculation of the diffusion coefficient for all treatments: (a) Using the intensity-time curve at r = δ, where δ was determined by the Dx70 exclusion, and (b) using the intensity-time curve at 4 pixels from the EC surface (r = 173

nm from the EC surface). This latter sublayer represented the minimum number of pixels (thickness) needed to compute the transient dye concentration profile. Results for computation of D based on the Dx70 exclusion thickness (D_{Dx70}) are shown in Fig. 27A for all treatments. Under control conditions (δ=462 nm), D_{Dx70} for FITC equaled $2.30\pm0.44 \times 10^{-9}$ cm^2/sec, which was three-orders less than its free diffusion coefficient of 2.7×10^{-6} cm^2/sec. After application of chondroitinase and hyaluronidase, D_{Dx70} increased significantly to $3.27\pm0.89 \times 10^{-9}$ and $3.24\pm1.28, \times 10^{-9}$ cm^2/sec, respectively, roughly a 1.4-fold increase. However, decreases were found following heparinase ($1.37\pm0.35 \times 10^{-9}$ cm^2/sec) and fMLP ($1.90\pm0.38 \times 10^{-9}$ cm^2/sec) treatments.

Diffusion coefficients for the sub-layer at 173 nm from the EC surface (D_{173}) are shown in Fig. 27B. Under control conditions, D_{173} was on the order of 1×10^{-9} cm^2/s, which was roughly half of the D_{Dx70}, suggesting a more compact sub-layer. In contrast, D_{173} for heparinase treatment was not significantly different from control ($p = 0.860$), and was only 25% less than that for the Dx70 thickness. Treatment with chondoitinase and hyaluronidase resulted in an increase in D_{173} to on the order of 2×10^{-9} cm^2/sec compared to control. Within the sub-layer, the effect of fMLP was similar to that of heparinase. These relative changes are addressed in the Discussion. The statistics of vessels size and goodness of the fits are summarized in Table 7.

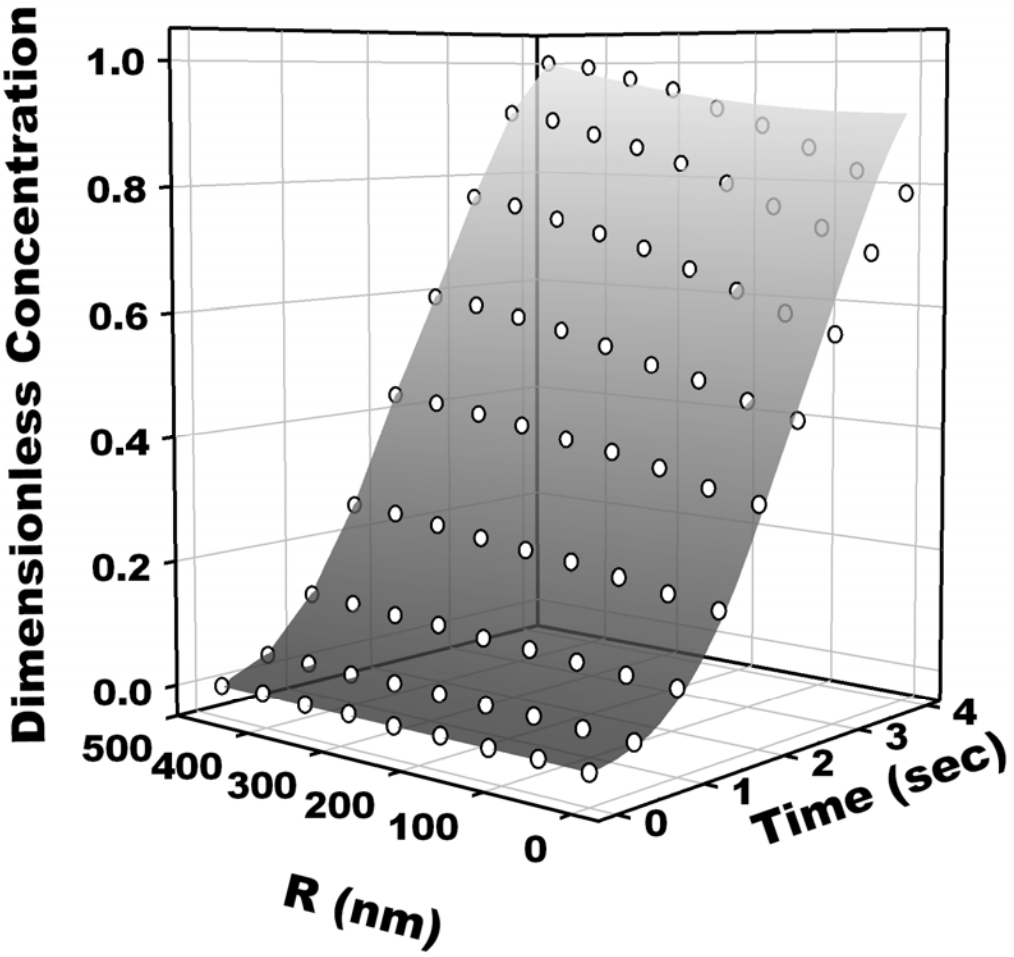

Figure 26: Radial concentration at the wall of a post-capillary venule following systemic infusion (jugular vein, i.v.) of a small solute (FITC). Measured fluorescence intensity profiles (○) were obtained with time, normal to venular wall. The shaded surface represents the solution to the 1-D diffusion model, computed using the measured intensity-time curve at a distance δ from the wall, determined by the exclusion of FITC-Dx70 (Fig. 5). In this illustrative case, the experimental data and the computational prediction agreed within an RMS error of 34.6%, and correspond to a diffusion coefficient for FITC of 2.61×10^{-9} cm^2/sec.

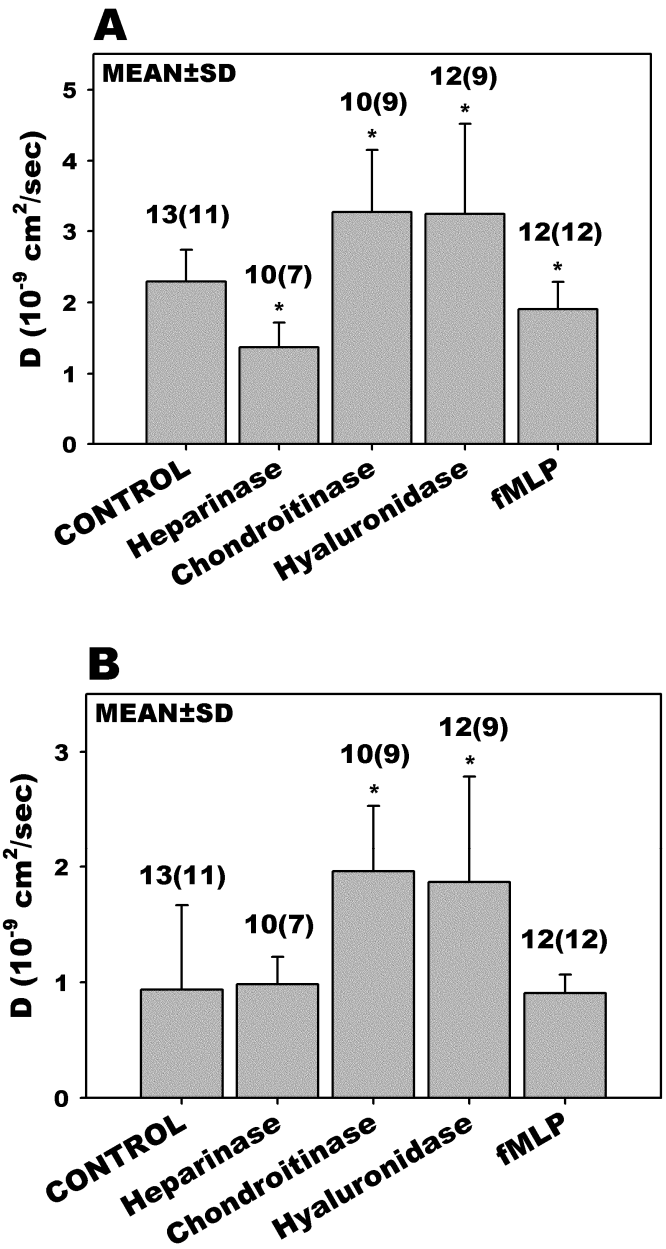

Figure 27: Calculated diffusion coefficient, D, of FITC in the glycocalyx obtained from a model of unsteady one dimensional diffusion normal to the EC surface. (A) Diffusion coefficient (D_{Dx70}) from solution of the diffusion equation based upon time variation of FITC concentration at a distance from the EC surface equal to the exclusion thickness of Dx70. (B) Diffusion coefficient (D_{173}) assessed for a sublayer 173 nm above the EC surface. Neither heparinase nor fMLP significantly affected D_{173}. The number of observations is given along with the number of post-capillary venules (in parenthesis). *Significantly different from control, $p<0.05$.

Table 7: Statistics of vessel diameters and curve fits determining the boundary of the glycocalyx and the diffusion coefficient of FITC

	Treatment	Control	Hepari-nase	Chondroi-tinase	Hyalu-ronidase	Enzyme mix	fMLP
(A) BS1 Cleavage assay	N	12	8	8	12		11
	Diameter (μm)	42.6 ±6.19	45.4 ±8.1	47.2 ± 8.3	44.6 ± 7.1		42.1 ± 11.4
(B) Sigmoidal fits of FITC-Dx70 radial intensity *	N	77	14	17	16	17	13
	Diameter (μm)	38.3 ±7.58	37.8 ±10.3	40.0 ± 8.5	39.9 ± 6.2	36.9 ± 5.7	36.2 ± 5.2
(C) Intensity-distance-time fits for diffusion coefficient calculation	N	10	7	7	8		9
	Diameter (μm)	25.5 ±5.9	27.7 ±8.1	38.3 ± 10.8	35.7 ±13..3		27.4 ± 7.4
	RMS error (%) D_{Dx70}	35.0 ±0.9%	33.8 ± 0.2%	33.9 ± 0.2	34.5 ± 0.6		34.2 ± 0.4
	RMS error (%) D_{173}	33.7 ±0.2%	33.6 ±0.1%	33.5 ± 0.1%	33.8 ±0.2%		33.7 ± 0.2%

Data are Mean ± SD

In each case, all treatments were not statistically significant from control for diameter and goodness of of of fit.

* For all sigmoidal fits, R^2=0.9998±0.0001 SD

4.4 Discussion

The studies of this section have aimed to delineate the relative contributions of the three principal GAGs which serve as a barrier to transvascular exchange of macromolecules and leukocyte-endothelium adhesion. The lability of the glycocalyx has been shown previously in models of inflammation by topical application of either the cytokine TNF-α (Henry and Duling, 2000) or the chemoattractant fMLP (Mulivor and Lipowsky, 2004). In the latter case, rapid shedding of glycans was indicated by a reduction in the bound fluorescent lectin BS1. Given the permissive nature of lectin binding (Schnitzer et al., 1990) and the increase of circulating HA found in response to stimuli such as shear and oxidative stress (Gouverneur et al., 2006) and hyperglycemia (Nieuwdorp et al., 2006), the effectiveness of enzymatically removing the BS1 stained glycocalyx was compared with the acute fMLP response (Fig. 4). The results of these experiments suggest that heparinase, chondroitinase and hyaluronidase are equal to or greater in cleaving their respective targets compared with the physiologically induced shedding by fMLP. Although the binding and staining of lectin to each of the GAG species may not be in proportion to GAG concentration, the slightly greater decrease in HS-bound lectin compared to that bound to CS is consistent with prior studies of the greater amounts of HS compared to CS. It has been shown that in the case of HS and CS bound to syndecans, there exists one or two CS chains for every four HS chain (Rapraeger and Bernfield, 1985).

Building upon techniques established by Vink and Duling (1996, 2000), a measure of the thickness of the glycocalyx was derived from the depth of infiltration of Dx70 which was consistent with their measurements for the undisturbed surface layer thickness, δ. Prior reports of the effect of hyaluronidase on δ are similar in many respects, albeit derived using other methods (systemic infusion *vs* direct perfusion of individual microvessels), different species (hamster or mouse *vs* rat), and/or different classes of microvessels (arterioles, capillaries or venules). Henry and Duling showed that systemic infusion of hyaluronidase for 1 hr resulted in a 35% reduction in δ in small post-capillary venules (10-15 μm) (Henry and Duling, 1999) which was equivalent to the decrease found herein by 10 min of direct perfusion using micropipettes in larger venules (14-60 μm). A similar loss of δ in response to infusion of hyaluronidase was inferred by the indirect technique of particle image velocimetry by extrapolation of venular velocity profiles in cremaster muscle (Potter and Damiano, 2008). The uniqueness of the present study is its attempt to make a systematic comparison of the individual contribution of all three GAGs to the barrier thickness in post-capillary venules where physiological shedding of glycans have been shown to govern the adhesion of leukocytes in models of inflammation and ischemia (Mulivor and Lipowsky, 2004).

4.4.1 Specificities of Enzymes

Three enzymes, heparinase, chondroitinase, and hyaluronidase, were used in the measurements of the barrier thickness. Interpretation of the effect of each enzyme

treatment needs to be made in light of their specificity for each GAG. It has been shown that heparinase III only cleaves HS and does not react with CS or HA (Lohse and Linhardt, 1992). However, hyaluronidase can degrade CS and chondroitinase can degrade HA. As a result, the chondroitinase or hyaluronidase treatments may not lead to exclusive degradation of CS or HA. To address the possible cross reactivity, all three enzymes were mixed and applied to the venular glycocalyx to degrade all three GAGs, as shown in Figure 24B. The thickness of the glycocalyx was reduced dramatically to 10.3% of the control for an 89.7% loss. By comparison, the percentage loss in thickness for individual enzymes was 43.3%, 34.1% and 26.1% for heparinase, chondroitinase and hyaluronidase, respectively. A simple model can be applied to attribute the loss in layer thickness to the fractional reduction of each individual GAG by assuming that the loss of each specific GAG is proportional to the decrease in glycocalyx thickness caused by each specific enzyme. A set of simultaneous algebraic equations may be written if one assumes that the specificity of each enzyme is such that: (1) All enzymatic degradations are maximal, (2) chondrotinase does not degrade HA significantly due to the low rate of enzymatic activity against HA (Hamai et al., 1997), and (3) hyaluronidase can cross-react with CS (Volpi et al., 1995). Based upon the data in Figure 24B, the percentage loss (PL) of the barrier thickness corresponding to each enzyme may then be expressed by the following equations:

$$PL_{HS} = 1 - \delta_{Heparinase} / \delta_{Control} = 43.3\% \quad (7)$$

$$PL_{CS} = 1 - \delta_{Chondroitinase} / \delta_{Control} = 34.1\% \quad (8)$$

$$PL_{HA} + PL_{CS'} = 1 - \delta_{Hyaluronidase} / \delta_{Control} = 26.1\% \quad (9)$$

$$PL_{HS} + PL_{CS} + PL_{HA} = 1 - \delta_{EnzymeMix} / \delta_{Control} = 89.7\% \quad (10)$$

where $PL_{CS'}$ refers to the percentage of the thickness reduction due to shedding of CS by hyaluronidase and the percentages on the right hand side are from Fig. 5B. Solution of these equations indicates that HS, CS and HA contributed 43.3%, 34.1% and 12.3% respectively to the barrier thickness, and collectively, the three GAGs account for 90% of the barrier thickness. Hyaluronidase also induced a major 13.8% ($PL_{CS'}$) drop in barrier thickness through cross-reacting with CS.

Thus, this simplified model suggests that HS provides the greatest contribution to the barrier thickness of the glycocalyx, followed by CS and HA. However, caution should be taken to interpret the reduction of 'barrier thickness' as reduction of 'glycocalyx thickness.' It has been shown that the magnitude of post-hyaluronidase reduction measured with Dx70 is similar to that with Dextran 145kDa, but completely vanished when using larger molecular weight dextrans of 580kDa or 2000kDa (Henry and Duling, 1999), suggesting that infiltration of Dx70 may follow an increase of porosity, instead of a decrease in layer thickness.

4.4.2 Structural Implications of the Glycocalyx Layer

The present results suggest a non-uniformity of GAG distribution through the depth of the glycocalyx. In control experiments, the significantly lower diffusion coefficient of FITC in the 173 nm thick sublayer compared to the value at the Dx70 exclusion thickness (463 nm) (Fig. 27) may reflect a non-uniform density of the glycocalyx. The difference suggests a denser sublayer that hinders FITC diffusion. The effective diffusion coefficient of small solutes in a porous media is proportional to the free media diffusion coefficient, porosity and constrictivity, and inversely proportional to the tortuosity of pathways. In a fibrous matrix such as the glycocalyx, the void volume is likely high enough to render the tortuosity as a trivial factor. The constrictivity is dependent upon size of the particle relative to the pore size. For FITC, with a Stokes-Einstein diameter of 1.68 nm, variations in pore size from 4 to 10 nm (Squire et al., 2001) may introduce significant heterogeneities in diffusion throughout the glycocalyx layer. The lower diffusion coefficient found in the sublayer is consistent with the their findings of a more compact layer near the EC surface, as indicated by greater staining of the glycocalyx 50-100 nm above the EC. This denser sublayer may result from continued biosynthesis of HA chains near the EC membrane and loss of distal GAGs by shear stress effects of blood flow on the outer boundary of the glycocalyx.

The variation of diffusion coefficient with specific enzyme treatment is also suggestive of the heterogeneity of GAG distribution. In Fig. 27, shedding of HS by heparinase failed to induce any change in the diffusion coefficient of the sublayer from the control. This suggests that HS predominantly resides in the top portion of the

glycocalyx layer. In contrast, shedding of CS and HA both significantly increased the diffusion coefficient two-fold from control within the 173 nm sublayer, suggesting greater amounts of CS and HA. The overall distributions of CS and HA are also likely to be biased toward the EC surface, because after shedding by chondroitinase or hyaluronidase, D_{173} increased two-fold, but only by a factor of 1.4 for D_{Dx70}. This finding is consistent with previous studies on syndecan-1 proteoglycan (a major glycocalyx associated GAG carrier) that the HS attachment sites are closer to the N-terminal where the CS attachment sites are in the proximity of the trans-membrane domain on the core protein (Kokenyesi and Bernfield, 1994). The observation that both D_{Dx70} and D_{173} increased dramatically from control after CS or HA was cleaved, but not with removal of HS, suggests that CS and HA contribute a significantly greater amount to glycocalyx permeability (by affecting the porosity of the glycocalyx layer) compared to HS.

The anomalous decrease in diffusion coefficient at the Dx-70 exclusion thickness with heparinase and fMLP may arise from structural rearrangements following the treatment. It is plausible that the layer collapses due to the loss of HS and associated macromolecules. In a previous study, Squire et al. observed reductions in the perpendicular spacings of the glycocalyx fiber matrix from 22.6 nm under control to 15.5 nm under inflammatory conditions (Squire et al., 2001). It would thus appear that HS could provide the structural support of the upper layer of the glycocalyx.

4.4.3 fMLP-induced Shedding and Permeability Alteration

Previous studies have shown that the glycocalyx is rapidly shed after 10 min application of fMLP (Mulivor and Lipowsky, 2004). In this study, after 10min fMLP superfusion, the glycocalyx thickness was reduced from 463 nm to 332 nm (Figure 24A), and the FITC diffusion coefficient (D_{Dx70}) across the glycocalyx layer decreased from 2.3 to 1.9×10^{-9} cm^2/sec (Fig. 27A). Thus it appears that fMLP decreased both barrier thickness and porosity. The combination of these two counteracting effects may result in no significant net change in the solute permeability across the layer. Previous studies have shown that fMLP alone was unable to change endothelial permeability, despite the fact that glycocalyx was lost (Zhu et al., 2005). The pattern of change in diffusion coefficient by fMLP is similar to heparinase, in which both treatments reduced D_{Dx70} but not $D_{173.}$ However, further studies are needed to determine if the dominant GAG loss with fMLP is heparan sulfate in contrast to chondroitin sulfate or hyaluronan.

Chapter 5

Summary

5.1 Summary of Results

The present study applied a two-step approach to delineate the thickness and permeability, two important variables that defines the barrier function of the endothelial glycocalyx. First, updated indicator dispersion technique was employed to study the effect of δ, Lp and D_{eff} to the solute transport through the glycocalyx, and using simulation to explore the correlation of these three parameters. The primary dependent variable $\Delta VTT/\Delta r$ denotes the slowing down of the VTT inside the glycocalyx layer, which enables, for the first time, the permeability of the glycocalyx layer being studied in the direction parallel to the flow. The results indicated that the mass flux is fairly uniform across the mainstream bound by two IPs, but declines fast across the glycocalyx layer. Through mathematical simulations, it is found that the axial convective flow quickly diminished, rendering the glycocalyx a diffusion-dominated layer. The concentration of FITC is essentially controlled by the diffusion process in the radial direction and the convective flow of water has little effect of the solute transport. The slope of VTT for FITC decreases with fMLP-induced local inflammation, suggesting an increased FITC transport. But no change in $\Delta VTT/\Delta r$ was observed when FITC was replaced with Dx70, suggesting Dx70 doesn't penetrate the glycocalyx structure.

The second set of experiments was then designed to further measure the thickness and diffusion coefficient in the diffusion-dominated glycocalyx layer. The thickness of the barrier layer was estimated by the distance between Dx70 column and the endothelial luminal surface. This technique was adapted from method originally used by Henry and Duling, and provided details in intravital microscopy and image processing, which the original work lacks, for example, which parameter to use in determine the edge of the dye column. Detailed protocol provided in this study can be repeated easily for consistent glycocalyx thickness estimation. The thickness measurements under control and enzymatic shedding of individual GAGs revealed the heparan sulfate glycosaminoglycan leads chondroitin sulfate and hyaluronan in supporting the proper dimension of the glycocalyx layer. Lost in any GAGs will reduce the thickness of the barrier. However, results also indicated that careful exercise is needed in interpret any barrier thickness changes using similar technique of exclusion thickness. More specifically, the reduction in the barrier thickness can be result of shrinking physical thickness, but can also be due to increased porosity which leads to deeper penetration of the solute. Thickness study also showed a significant degree of enzymatic activity toward CS by hyaluronidase, which should be considered in other studies involving specific shedding of HA.

The method used in measuring the diffusion coefficient of FITC in the glycocalyx media is also innovative by measuring the initial radial penetration of small FITC molecules into the glycocalyx. Although inherited with certain level of optical error, this technique is fast, sensitive and providing an unique feature that allows the diffusion within the layer to be measured. The diffusion coefficients of FITC across the whole layer and within a 173 nm sublayer were measured in control and enzyme-treated

conditions. Rich information has been obtained and revealed the differentiated roles of three GAGs in the structure and biological funtions of the glycocalyx. The structural support is mainly from the heparan sulfate, and the diffusion constrain toward macromolecules is more influenced by chondroitin sulfate and hyaluronan. The distribution of three GAGs is not random or even. Chondroitin sulfate and hyaluronan exist through all depth of the glycocalyx layer. However, heparan sulfate is located on the upper portion (toward vessel lumen) of the layer. This biased distribution may also lead to different roles in physiological functions.

Using BS-1 lectin staining, experiments revealed the HS to CS ratio is similar to the ratio of syndecan-1. Also, the results confirmed that GAGs are modified with post-synthesis sialylation, which is exclusively on chondroitin sulfate.

5.2 Improvements and Future Work

The biggest uncertainty in measuring the thickness and permeability of the glycocalyx in present study is the two parameters can not be obtained simultaneously. Currently, the thickness used in determining the diffusion coefficient was obtained in separated experiments using different fluorescent dyes. As a result, the computational estimation of the diffusion coefficient will be less precise without using the true local thickness of the layer. To overcome this obstacle, two fluorescent molecules with different wavelengths can be applied to the circulation for thickness and diffusion coefficient measurements respectively, for example, TRITC-conjugated 70 kDa dextran for thickness measurement and free FITC for diffusion coefficient measurement.

In all experiments, images from brightfield and fluorescent illumination were needed with the requirement for perfect alignment. In many cases, the tissue movements due to labored respiration or intestinal peristaltic movement led to inacceptable recordings. Improvement in the design of the animal stage will help better supporting the exteriorized tissue and minimizing the movement to improve the successful ratio.

The present study opened up a new avenue in future research to examine the fine sub-structure of the glycocalyx, the integration to the intracellular structures and molecules, as well as detailed steps in alteration under disease states. Based on the results of this study, being able to simultaneously label GAGs with different fluorescent molecules will enable co-localization of three GAGs, studying on the dynamics of individual GAG during inflammation or other cardiovascular challenges, and elucidating the association of GAGs to cytoskeleton, G-protein, enzymes and receptors of the endothelial cells.

References

Adamson RH 1990 Permeability of frog mesenteric capillaries after partial pronase digestion of the endothelial glycocalyx. J Physiol 428:1-13

Adamson RH, Clough G 1992 Plasma proteins modify the endothelial cell glycocalyx of frog mesenteric microvessels. J Physiol 445:473-486

Anderson AO, Anderson ND 1976 Lymphocyte emigration from high endothelial venules in rat lymph nodes. Immunology 31:731-748

Aruffo A, Stamenkovic I, Melnick M, Underhill CB, Seed B 1990 CD44 is the principal cell surface receptor for hyaluronate. Cell 61:1303-1313

Ausprunk DH, Boudreau CL, Nelson DA 1981a Proteoglycans in the microvascular. II. Histochemical localization in proliferating capillaries of the rabbit cornea. Am J Pathol 103:367-375

Ausprunk DH, Boudreau CL, Nelson DA 1981b Proteoglycans in the microvasculature. I. Histochemical localization in microvessels of the rabbit eye. Am J Pathol 103:353-366

Benjawatanapon C, Bell LE, Williams L 1982 Ultrastructural localisation of alkaline phosphatase in adult human large intestine. Gut 23:134-136

Broekhuizen LN, Mooij HL, Kastelein JJ, Stroes ES, Vink H, Nieuwdorp M 2009 Endothelial glycocalyx as potential diagnostic and therapeutic target in cardiovascular disease. Curr Opin Lipidol 20:57-62

Carey DJ 1997 Syndecans: multifunctional cell-surface co-receptors. Biochem J 327 (Pt 1):1-16

Chappell D, Jacob M, Paul O, Rehm M, Welsch U, Stoeckelhuber M, Conzen P, Becker BF 2009 The glycocalyx of the human umbilical vein endothelial cell: an impressive structure ex vivo but not in culture. Circ Res 104:1313-1317

Chen RL, Lander AD 2001 Mechanisms underlying preferential assembly of heparan sulfate on glypican-1. J Biol Chem 276:7507-7517

Cummings RD, Smith DF 1992 The selectin family of carbohydrate-binding proteins: structure and importance of carbohydrate ligands for cell adhesion. Bioessays 14:849-856

Dougher AM, Wasserstrom H, Torley L, Shridaran L, Westdock P, Hileman RE, Fromm JR, Anderberg R, Lyman S, Linhardt RJ, Kaplan J, Terman BI 1997 Identification of a heparin binding peptide on the extracellular domain of the KDR VEGF receptor. Growth Factors 14:257-268

Filmus J, Capurro M, Rast J 2008 Glypicans. Genome Biol 9:224

Fitzgerald ML, Wang Z, Park PW, Murphy G, Bernfield M 2000 Shedding of syndecan-1 and -4 ectodomains is regulated by multiple signaling pathways and mediated by a TIMP-3-sensitive metalloproteinase. J Cell Biol 148:811-824

Florian JA, Kosky JR, Ainslie K, Pang Z, Dull RO, Tarbell JM 2003 Heparan sulfate proteoglycan is a mechanosensor on endothelial cells. Circ Res 93:e136-e142

Fransson LA 2003 Glypicans. Int J Biochem Cell Biol 35:125-129

Fromm JR, Hileman RE, Weiler JM, Linhardt RJ 1997 Interaction of fibroblast growth factor-1 and related peptides with heparan sulfate and its oligosaccharides. Arch Biochem Biophys 346:252-262

Ghitescu L, Fixman A 1984 Surface charge distribution on the endothelial cell of liver sinusoids. J Cell Biol 99:639-647

Gouverneur M, Broekhuizen L, Meuwese M, Mooij HL, Stroes ES, Vink H 2008 Sulfated glycosaminoglycans restore glycocalyx barrier properties of cultured endothelial cells in hyperglycemia. FASEB J 22:lb83

Gouverneur M, Spaan JA, Pannekoek H, Fontijn RD, Vink H 2006 Fluid shear stress stimulates incorporation of hyaluronan into endothelial cell glycocalyx. Am J Physiol Heart Circ Physiol 290:H458-2

Hamai A, Hashimoto N, Mochizuki H, Kato F, Makiguchi Y, Horie K, Suzuki S 1997 Two distinct chondroitin sulfate ABC lyases. An endoeliminase yielding tetrasaccharides and an exoeliminase preferentially acting on oligosaccharides. J Biol Chem 272:9123-9130

Henry CB, Duling BR 1999 Permeation of the luminal capillary glycocalyx is determined by hyaluronan. Am J Physiol 277:H508-H514

Henry CB, Duling BR 2000 TNF-alpha increases entry of macromolecules into luminal endothelial cell glycocalyx. Am J Physiol Heart Circ Physiol 279:H2815-H2823

Ho G, Broze GJ, Jr., Schwartz AL 1997 Role of heparan sulfate proteoglycans in the uptake and degradation of tissue factor pathway inhibitor-coagulation factor Xa complexes. J Biol Chem 272:16838-16844

Hornung M, Wollensak J 1979 [Proof of glycosaminoglycans in the corneal endothelium]. Albrecht Von Graefes Arch Klin Exp Ophthalmol 211:67-84

Jacob M, Chappell D, Rehm M 2009 The 'third space'--fact or fiction? Best Pract Res Clin Anaesthesiol 23:145-157

Jacob M, Rehm M, Loetsch M, Paul JO, Bruegger D, Welsch U, Conzen P, Becker BF 2007 The endothelial glycocalyx prefers albumin for evoking shear stress-induced, nitric oxide-mediated coronary dilatation. J Vasc Res 44:435-443

Jimenez D, Roda-Navarro P, Springer TA, Casasnovas JM 2005 Contribution of N-linked glycans to the conformation and function of intercellular adhesion molecules (ICAMs). J Biol Chem 280:5854-5861

Karlsson K, Marklund SL 1988 Extracellular-superoxide dismutase association with cell surface-bound sulfated glucosaminoglycans. Basic Life Sci 49:647-650

Kato H 2002 Regulation of functions of vascular wall cells by tissue factor pathway inhibitor: basic and clinical aspects. Arterioscler Thromb Vasc Biol 22:539-548

Kokenyesi R, Bernfield M 1994 Core protein structure and sequence determine the site and presence of heparan sulfate and chondroitin sulfate on syndecan-1. J Biol Chem 269:12304-12309

Laurent TC, Fraser JR 1992 Hyaluronan. FASEB J 6:2397-2404

Lindahl U, Hook M 1978 Glycosaminoglycans and their binding to biological macromolecules. Annu Rev Biochem 47:385-417

Lipowsky HH 2005 Microvascular rheology and hemodynamics. Microcirculation 12:5-15

Lipowsky HH, Cram LE, Justice W, Eppihimer MJ 1993 Effect of erythrocyte deformability on in vivo red cell transit time and hematocrit and their correlation with in vitro filterability. Microvasc Res 46:43-64

Lohse DL, Linhardt RJ 1992 Purification and characterization of heparin lyases from Flavobacterium heparinum. J Biol Chem 267:24347-24355

Luft JH 1966 Fine structures of capillary and endocapillary layer as revealed by ruthenium red. Fed Proc 25:1773-1783

McEver RP 1994 Selectins. Curr Opin Immunol 6:75-84

McKay CB, Lipowsky HH 1988 Arteriovenous distribution of transit times in cremaster muscle of the rat. Microvasc Res 36:75-91

MEIER P, ZIERLER KL 1954 On the theory of the indicator-dilution method for measurement of blood flow and volume. J Appl Physiol 6:731-744

Monnens LA 1982 [The basal membrane of the kidney]. Tijdschr Kindergeneeskd 50:121-130

Mulivor AW, Lipowsky HH 2002 Role of glycocalyx in leukocyte-endothelial cell adhesion. Am J Physiol Heart Circ Physiol 283:H1282-H1291

Mulivor AW, Lipowsky HH 2004 Inflammation- and ischemia-induced shedding of venular glycocalyx. Am J Physiol Heart Circ Physiol 286:H1672-H1680

Nieuwdorp M, Meuwese MC, Mooij HL, Ince C, Broekhuizen LN, Kastelein JJ, Stroes ES, Vink H 2008 Measuring endothelial glycocalyx dimensions in humans: a potential novel tool to monitor vascular vulnerability. J Appl Physiol 104:845-852

Nieuwdorp M, van Haeften TW, Gouverneur MC, Mooij HL, van Lieshout MH, Levi M, Meijers JC, Holleman F, Hoekstra JB, Vink H, Kastelein JJ, Stroes ES 2006 Loss of endothelial glycocalyx during acute hyperglycemia coincides with endothelial dysfunction and coagulation activation in vivo. Diabetes 55:480-486

Nijenhuis N, Mizuno D, Spaan JA, Schmidt CF 2009 Viscoelastic response of a model endothelial glycocalyx. Phys Biol 6:025014

Periasamy N, Verkman AS 1998 Analysis of fluorophore diffusion by continuous distributions of diffusion coefficients: application to photobleaching measurements of multicomponent and anomalous diffusion. Biophys J 75:557-567

Potter DR, Damiano ER 2008 The hydrodynamically relevant endothelial cell glycocalyx observed in vivo is absent in vitro. Circ Res 102:770-776

Pries AR, Secomb TW, Gaehtgens P 2000 The endothelial surface layer. Pflugers Arch 440:653-666

Rapraeger A, Bernfield M 1985 Cell surface proteoglycan of mammary epithelial cells. Protease releases a heparan sulfate-rich ectodomain from a putative membrane-anchored domain. J Biol Chem 260:4103-4109

Robinson CJ, Stringer SE 2001 The splice variants of vascular endothelial growth factor (VEGF) and their receptors. J Cell Sci 114:853-865

Romanova LK, Filippenko LN 1975 [The state of the "glycocalyx" of rat lung cells following left-sided pneumonectomy]. Biull Eksp Biol Med 80:25-29

Rostgaard J, Qvortrup K 1997 Electron microscopic demonstrations of filamentous molecular sieve plugs in capillary fenestrae. Microvasc Res 53:1-13

Ryan US, Ryan JW 1984 The ultrastructural basis of endothelial cell surface functions. Biorheology 21:155-170

Ryan US, Ryan JW, Crutchley DJ 1985 The pulmonary endothelial surface. Fed Proc 44:2603-2609

Schneeberger EE 1988 Interaction of plasma proteins with negatively charged sites on the pulmonary capillary endothelium of the rat. Cell Tissue Res 251:417-423

Schnitzer JE, Shen CP, Palade GE 1990 Lectin analysis of common glycoproteins detected on the surface of continuous microvascular endothelium in situ and in culture: identification of sialoglycoproteins. Eur J Cell Biol 52:241-251

Scott JE, Heatley F 1999 Hyaluronan forms specific stable tertiary structures in aqueous solution: a 13C NMR study. Proc Natl Acad Sci U S A 96:4850-4855

Shimada K., Kobayashi K., Kobayashi M., Kimura S., Nishinaga M., Takeuchi K., Ozawa T., 1991, Anticoagulant heparin-like glycosaminoglycans on endothelial cell surface. Japanese Circulation Journal 55, 1016-1021.

Singh A, Satchell SC, Neal CR, McKenzie EA, Tooke JE, Mathieson PW 2007 Glomerular endothelial glycocalyx constitutes a barrier to protein permeability. J Am Soc Nephrol 18:2885-2893

Smith ML, Long DS, Damiano ER, Ley K 2003 Near-wall micro-PIV reveals a hydrodynamically relevant endothelial surface layer in venules in vivo. Biophys J 85:637-645

Spaeth EE, Friedlander SK 1967 The diffusion of oxygen, carbon dioxide, and inert gas in flowing blood. Biophys J 7:827-851

Squire JM, Chew M, Nneji G, Neal C, Barry J, Michel C 2001 Quasi-periodic substructure in the microvessel endothelial glycocalyx: a possible explanation for molecular filtering? J Struct Biol 136:239-255

Sugahara K, Mikami T, Uyama T, Mizuguchi S, Nomura K, Kitagawa H 2003 Recent advances in the structural biology of chondroitin sulfate and dermatan sulfate. Curr Opin Struct Biol 13:612-620

Sugihara-Seki M., Akinaga T, Itano T., 2008, Flow across microvessel walls through the endothelial surface glycocalyx and the interendothelial cleft. Journal of Fluid Mechanics 601, 229-252.

Tarbell JM, Ebong EE 2008 The endothelial glycocalyx: a mechano-sensor and -transducer. Sci Signal 1:t8

Taylor G 1953 Dispersion of Soluble Matter in Solvent Flowing Slowly Through A Tube. Proceedings of the Royal Society of London Series A-Mathematical and Physical Sciences 219:186-203

Taylor G 1954 Conditions Under Which Dispersion of A Solute in A Stream of Solvent Can be Used to Measure Molecular Diffusion. Proceedings of the Royal Society of London Series A-Mathematical and Physical Sciences 225:473-477

Thi MM, Tarbell JM, Weinbaum S, Spray DC 2004 The role of the glycocalyx in reorganization of the actin cytoskeleton under fluid shear stress: a "bumper-car" model. Proc Natl Acad Sci U S A 101:16483-16488

Tumova S, Woods A, Couchman JR 2000 Heparan sulfate proteoglycans on the cell surface: versatile coordinators of cellular functions. Int J Biochem Cell Biol 32:269-288

Ueda A, Shimomura M, Ikeda M, Yamaguchi R, Tanishita K 2004 Effect of glycocalyx on shear-dependent albumin uptake in endothelial cells. Am J Physiol Heart Circ Physiol 287:H2287-H2294

Van den Berg BM, Spaan JA, Vink H 2009 Impaired glycocalyx barrier properties contribute to enhanced intimal low-density lipoprotein accumulation at the carotid artery bifurcation in mice. Pflugers Arch 457:1199-1206

Van Teeffelen JW, Brands J, Stroes ES, Vink H 2007 Endothelial glycocalyx: sweet shield of blood vessels. Trends Cardiovasc Med 17:101-105

Vartanian KB, Berny MA, McCarty OJ, Hanson SR, Hinds MT 2010 Cytoskeletal structure regulates endothelial cell immunogenicity independent of fluid shear stress. Am J Physiol Cell Physiol 298:C333-C341

Vink H, Duling BR 2000 Capillary endothelial surface layer selectively reduces plasma solute distribution volume. Am J Physiol Heart Circ Physiol 278:H285-H289

Volpi N, Sandri I, Venturelli T 1995 Activity of chondroitin ABC lyase and hyaluronidase on free-radical degraded chondroitin sulfate. Carbohydr Res 279:193-200

Wang CS, Hartsuck J, McConathy WJ 1992 Structure and functional properties of lipoprotein lipase. Biochim Biophys Acta 1123:1-17

Weinbaum S, Zhang X, Han Y, Vink H, Cowin SC 2003 Mechanotransduction and flow across the endothelial glycocalyx. Proc Natl Acad Sci U S A 100:7988-7995

Yao Y, Rabodzey A, Dewey CF, Jr. 2007 Glycocalyx modulates the motility and proliferative response of vascular endothelium to fluid shear stress. Am J Physiol Heart Circ Physiol 293:H1023-H1030

Zhang X, Curry FR, Weinbaum S 2006 Mechanism of osmotic flow in a periodic fiber array. Am J Physiol Heart Circ Physiol 290:H844-H852

Zhu L, Castranova V, He P 2005 fMLP-stimulated neutrophils increase endothelial [Ca2+]i and microvessel permeability in the absence of adhesion: role of reactive oxygen species. Am J Physiol Heart Circ Physiol 288:H1331-H1338

Appendix **A**

Deinterlace Routine

The deinterlace routine was used in ImageJ for the processing of digitized image sequence (in TIFF) of FITC bolus captured by SIT-66 camera. After load the TIFF file into ImageJ, the user can hit 'd' to initiate the automatic deinterlace routine.

Language: Java
Software: ImageJ

```
macro "Deinterlace a stack [d]" {

FNo=nSlices;

width = getWidth();
height = getHeight();
avg=newArray(width);
for (k=0; k<FNo; k++) {
    run("Copy");
    run("Add Slice");
    run("Paste");
    run("Previous Slice [<]");

    for (y=2; y<height; y+=2) {
        for (x=0; x<width; x++) {
            p1 = getPixel(x, y-1);
            p2 = getPixel(x, y+1);
          avg = ((p1+p2)/2);
            setPixel(x, y, avg);
        }
    }
    for (x=0; x<width; x++) {
        p1 = getPixel(x, 1);
        p2 = getPixel(x, 3);
        avg = 1.5*p1-0.5*p2;
        setPixel(x, 0, avg);
    }
    for (y=0; y<height-1; y++) {
      for (x=0; x<width; x++) {
      setPixel(x,y,getPixel(x,y+1));
      }
    }
    run("Next Slice [>]");

    for (y=1; y<height-2; y+=2) {
        for (x=0; x<width; x++) {
            p1 = getPixel(x, y-1);
```

```
            p2 = getPixel(x, y+1);
          avg = ((p1+p2)/2);
            setPixel(x, y, avg);
        }
    }
    for (x=0; x<width; x++) {
        p1 = getPixel(x, height-1);
        p2 = getPixel(x, height-3);
        avg = 1.5*p1-0.5*p2;
        setPixel(x, height-1, avg);
    }
    for (y=height-1; y>1; y--) {
      for (x=0; x<width; x++) {
      setPixel(x,y,getPixel(x,y-1));
      }
    }
    run("Next Slice [>]");
}
```

Appendix B

Intensity-Time Recording Routine

The intensity-time recording routine was a macro using in ImageJ to measure the intensity-time data on a measurement line drawn on the deinterlaced TIFF image stack of the FITC bolus. To measure, a measurement line that is normal to local EC surface was drawn, then hitting 'f' to start the routine. A pop-up dialogue would appear to acquire desired number of slices to measure.

Language: Java
Software: ImageJ

```
macro "Intensity Time on one SL [f]" {

OrthLength=getNumber("Half bar length in pixel: ", 0);
getSelectionCoordinates(x6, y6);
FNo=getNumber("number of frame in the stack",nSlices);
setSlice(1);

preprofile=getProfile();
envelope=preprofile.length;
ll=envelope;

gg=(x6[1]-x6[0])*(x6[1]-x6[0])+(y6[1]-y6[0])*(y6[1]-y6[0]);
gx=(x6[1]-x6[0])/sqrt(gg);
gy=(y6[1]-y6[0])/sqrt(gg);

x60=x6[0]; y60=y6[0];
dpm=(x60-x6[0])*(x60-x6[0])+(y60-y6[0])*(y60-y6[0]);

profile=newArray(envelope);
CSFI=newArray(envelope);

for (k=0; k<FNo; k++) {
//profile = getProfile();
for (k6=0; k6<ll; k6++) {
x60=(x60+1*gx);
y60=(y60+1*gy);
dpm=(x60-x6[0])*(x60-x6[0])+(y60-y6[0])*(y60-y6[0]);
x61=(x60-OrthLength*gy);
y61=(y60+OrthLength*gx);
x62=(x60+OrthLength*gy);
y62=(y60-OrthLength*gx);

makeLine(x61, y61, x62, y62);
getStatistics(ar,meanfi0, mi, ma);
profile[k6]=meanfi0;
```

```
//print(meanfi0);
//wait(20);
}
x60=x6[0]; y60=y6[0];

for (i1=0; i1<envelope; i1++) {
CSFI[i1] = profile[i1];
if (CSFI[i1]<0) {CSFI[i1]=0;}
print(k+", "+(i1+1)+", "+CSFI[i1]);
}
run("Next Slice [>]");
}

makeLine(x6[0],y6[0],x6[1],y6[1]);
}
```

Appendix C

Radial Intensity Profile Across the Glycocalyx

The radial intensity profile routine was a macro used in ImageJ to measure the transient intensity profile of the fluorescence-labeled glycocalyx. After selecting the background frame, the user would first draw a measurement line that defines the ideal half length of the measurement in radial direction (200-pixel line was used in this study), then hit 'y' to register the length of the line. Then a polygon tracing line has to be drawn to mark the outer edge of the refractive band. The routine will start by hitting 't', checking 'finished' and clicking 'OK'. The radial intensity profile is then averaged along the polygon tracing line. The process will be repeated on each the following 8 to 10 frames.

Language: Java
Software: ImageJ

```
macro "Ave Rad Prof [t]" {
OrthLength=getResult("OrthLength",0)
//OrthLength=getNumber("Half bar length in pixel: ", 35);

//    OrthLength = 50;  //Initial length guess of line

      RadialWidth = OrthLength * 2;

//



//do profile and then get profile.length as the full width of the line

//Lets find centerline



getSelectionCoordinates(x, y);
      // (x,y) are the coordinates of the nodes in the line
      // If there are n nodes, then there are n-1 segments
      //Let k = the number of radial profiles that are to be averaged
      k=0;  //This is the index variable for saving profiles
      segNo=lengthOf(x)-1;
      //print ("segNo =", segNo);


//Get the array of intensities along the very first radial segment
//to define the initial reference.  This assumes that you have made a
good
```

```
//centered choice for the beginning of the line.

i = 0;
      gg=(x[i+1]-x[i])*(x[i+1]-x[i])+(y[i+1]-y[i])*(y[i+1]-y[i]);
      gx=(x[i+1]-x[i])/sqrt(gg);
      gy=(y[i+1]-y[i])/sqrt(gg);

      x0=x[i];
      y0=y[i];
      dpm=(x0-x[i])*(x0-x[i])+(y0-y[i])*(y0-y[i]);
            x0=(x0+2*gx);
            y0=(y0+2*gy);
            //print ("x0 = ", x0, "      y0 = ", y0);
            dpm=(x0-x[i])*(x0-x[i])+(y0-y[i])*(y0-y[i]);
            x1=(x0-OrthLength*gy);
            y1=(y0+OrthLength*gx);
            x2=(x0+OrthLength*gy);
            y2=(y0-OrthLength*gx);
            makeLine(x1, y1, x2, y2);



//*******************Routine to size and re-size the length of the
radial scan line*************
      jj = 1;
      while (jj <= 1) {


      Dialog.create("Select Size");

      Dialog.addCheckbox("Add", false);
      Dialog.addCheckbox("Sub", false);
      Dialog.addCheckbox("Finished", false);
      Dialog.show();
      Add = Dialog.getCheckbox();
      Sub = Dialog.getCheckbox();
      Finished = Dialog.getCheckbox();
      if(Add==true)    OrthLength = OrthLength + 5;
      if (Sub==true)   OrthLength = OrthLength - 5;

            x1=(x0-OrthLength*gy);
            y1=(y0+OrthLength*gx);
            x2=(x0+OrthLength*gy);
            y2=(y0-OrthLength*gx);
            makeLine(x1, y1, x2, y2);
      print("OrthLength = " + OrthLength);
      if (Finished==true) jj=2;}
//**********************End of size  and re-size
routing**********************

      RadialWidth = OrthLength * 2;

//Create a temporary storage array to hold all the profiles along the
centerline with max size
//equal to the product of length of profile x 1024
```

```
      Storage = newArray(RadialWidth*1024);   //Store the full profile
for display
      StoreAC = newArray(RadialWidth*1024); //Store the AC component
for cross-corr

//Define Temp Arrays
      A0 = newArray(RadialWidth+1);  //for saving the first profile
      A1 = newArray(RadialWidth+1);  //for saving the ith profile as
needed

      //add "1" to max dimension for safetysake
//*****************************************************************
***************
            profile = getLineValues(x1,y1,x2,y2);  //use this function
from the web

            A0 = profile;  //this is the reference profile array
//          for (ii = 0;ii<=RadialWidth-1;ii++){print("A0 = " +
A0[ii]);}


// k is the index variable for saving profiles
for (i=0; i<segNo; i++) {
      //print ( "   x(",  i,      ") = ",       x[i],       "
y(",       i ,       ") =  ", y[i]      );
      gg=(x[i+1]-x[i])*(x[i+1]-x[i])+(y[i+1]-y[i])*(y[i+1]-y[i]);
      gx=(x[i+1]-x[i])/sqrt(gg);
      gy=(y[i+1]-y[i])/sqrt(gg);

      x0=x[i];
      y0=y[i];
      dpm=(x0-x[i])*(x0-x[i])+(y0-y[i])*(y0-y[i]);

      while (sqrt(dpm)<=sqrt(gg)) {
            x0=(x0+2*gx);
            y0=(y0+2*gy);
            //print ("x0 = ", x0, "      y0 = ", y0);
            dpm=(x0-x[i])*(x0-x[i])+(y0-y[i])*(y0-y[i]);
            x1=(x0-OrthLength*gy);
            y1=(y0+OrthLength*gx);
            x2=(x0+OrthLength*gy);
            y2=(y0-OrthLength*gx);
            //print(x1,y1,x2,y2);
            makeLine(x1, y1, x2, y2);

            profile = getLineValues(x1,y1,x2,y2);  //use this function
from the web
            A1 = profile;

      Ntot = 0;
//Calculate the average value of this radial profile
      AveA1 = 0;
            for (n=0; n<profile.length-1;n++){
            Ntot++;
```

```
            AveA1 = AveA1 + A1[n];
            }
      AveA1 = AveA1/Ntot; //this is the DC value

//Store the ith profile in the storage array
            for (n=0; n<=profile.length-1;n++){
            Storage[n + RadialWidth*k]  = A1[n];
//          print ("A1[" + n + "," + k +  "] = " + A1[n]);
//          print ("Storage( " + n + RadialWidth*k + ")  = " +
Storage[n + RadialWidth*k]+"  k = "+k);
            }


//    setResult("MaxFI",k,MaxInten);
//    print("k = " + k);
      k++;
      MaxInten=0;
      wait(0);
      }

}
//Let's display the collected profiles

      print ("Out of the loop now and k = " + k);

      Nprofiles = k;

newImage("temp", "16-bit ramp", RadialWidth, Nprofiles, 1);

for (i = 0;i<=RadialWidth-1;i++){
      for(j=0;j<=Nprofiles-1;j++) {
            index = i + j*RadialWidth;
            //value =0;//= Storage[index];
            //print("index = "+ index+" i = " + i + "  j = " + j+
"Storage(i,j) = " + Storage[index]);
            setPixel(i, j, Storage[index]);
      }}

updateDisplay();
run("Brightness/Contrast...");
run("Enhance Contrast", "saturated=0.5");


//run("Surface Plot...", "polygon=100" draw temp);

//Now we are ready to cross-correlate StoreAC(i) against StoreAC(0) to
get the shift Delta
//Let L = half the total shift
      L = 20;
      RXY=newArray(L*2);  //Reserve an array for the correlogram
                  //RXY = correlogram array



//Compute the average of all non-shifted profiles.
```

```
      Aveprofile = newArray(RadialWidth);
      STD = newArray(RadialWidth);
      xprofile= newArray(RadialWidth);
//Let us modify the plot display to plot only the second half of the
ave radial profile, putting origin at RadialWidth/2
      for(i = 0;i<=RadialWidth-1; i++){
            ncount = 0;
            ave=0;
            ss =0;
            std= 0;
            for(n=0;n<=Nprofiles-1;n++){

                  ave = ave + Storage[i+RadialWidth*n];
                  ss    =  ss  +
Storage[i+RadialWidth*n]*Storage[i+RadialWidth*n];
                  ncount++;
//                print ("ncount = "+ncount + "    Storage =
"+Storage[i+RadialWidth*n]);
                  }
            Aveprofile[i] = ave/ncount;
            STD[i] = (ss/(ncount-1) )  - ave*ave/(ncount*(ncount-1));
            STD[i] = sqrt(STD[i]);
            xprofile[i] = i;
            }

//    xhalfprofile=newArray(RadialWidth/2);
//    yhalfprofile=newArray(RadialWidth/2);
//    for(i=0;i<=RadialWidth/2-1;i++){
//          xhalfprofile[i] = xprofile[i];
//          yhalfprofile[i]= Aveprofile[i];
//          }
// Note: this plots the lef half of the profile, which is good if the
selection line is to the right of the dye column
Plot.create("Average Profile", "Radial Position", "Aveprofile",
xprofile, Aveprofile);
//Plot.create("Distance from EC","Distance from
EC","Intensity",xhalfprofile,yhalfprofile);
Plot.setColor("red");
//Plot.add("error bars", xprofile, STD);


exit();

//updateResults();
MeanFI=0;
StddevFI=0;
      for (i2=0; i2<nResults; i2++) {
            MeanFI=MeanFI+getResult("MaxFI",i2);
      }

MeanFI=MeanFI/nResults;

      for (i3=0; i3<nResults; i3++) {
      StddevFI=StddevFI+(getResult("MaxFI",i3)-
MeanFI)*(getResult("MaxFI",i3)-MeanFI);
```

```
      }

StddevFI=sqrt(StddevFI/(nResults-1));

print("No.   "+"Mean    "+"    Std Dev");
print(nResults+"  "+MeanFI+"  "+StddevFI);


}
//*********************************
  function getLineValues(x1, y1, x2, y2) {
      dx = x2-x1;
      dy = y2-y1;
      n = round(sqrt(dx*dx + dy*dy));
      xinc = dx/n;
      yinc = dy/n;
      n++;
      values = newArray(n);
       i = 0;
       do {
          values[i++] = getPixel(x1,y1);
          x1 += xinc;
          y1 += yinc;
      } while (i<n);
      return values;
  }
```

Appendix D

Computation of the Diffusion Coefficient of FITC inside the Glycocalyx

The following program is to compute the corresponding diffusion coefficient of the FITC inside the glycocalyx layer. The experimentally measured intensity-time data was organized as a matrix, of which the column represents the radial dimension from 0 to a desired thickness and the row represents the time starting with the background intensity. Then a column of radial dimension in the unit of nm was put in front of matrix and saved the matrix variable 'rInt0' in the program 'DataInput.m'. The 'DataInput.m' will call function 'seekingD.m' to scan a pre-defined range of the diffusion coefficient 'D' for the diffusion coefficient with the minimal RMS error which is computed by another function 'surf_fit.m'. The data in 'rInt0' listed below is a representative data matrix. The precision of the resulting D is set as 0.01×10^{-9} cm^2/sec.

Software: MatLab
Program 1, `DataInput.m`

```
%close all
clear
clc
%% Input
% make sure the first column is in the unit of nm
rInt0=[0.0  751.1347    825.2244873 934.5633    1083.3306   1304.8326
57.8    750.9224    826.6122437 942.0245    1091.3633   1323.6571
115.6   761.0123    827.7387695 945.8123    1100.9469   1330.0571
173.4   758.6776    837.5183716 953.2898    1109.5183   1345.6653
231.2   766.2694    842.302063  957.9918    1122.9225   1357.9755
289.0   764.7837    844.9959106 968.4572    1128.3265   1379.8857
346.8   778.8735    850.1061401 978.4163    1144.3755   1392
404.6   777.0123    863.8040771 982.0735    1154.7755   1410.4
462.4   789.6653    858.6775513 997.6163    1169.1919   1421.3877
520.2   791.9673    869.2244873 1004.849    1174.6613   1439.3306
578.0   795.4939    875.8204346 1007.5755   1186.0571   1461.8612
635.8   796.4408    885.453064  1024.7347   1196.6367   1478.6123
];
%% Selection of input data for computation of D
% smallest matrix is rInt0(1:4,1:6)
[m0,n0]=size(rInt0);
rangeR=[3:18]';
rangeT=[11]';

%% Compute Diffusion Coefficient and Root Square Error
counter=0;
for k1=1:length(rangeR);
    for k2=1:length(rangeT);
        counter=counter+1;
```

```
        rInt=rInt0(1:rangeR(k1),1:rangeT(k2));
        %% Define time sequence
        [m,n]=size(rInt);
        tT=.5*[0:1:n-3]';
        [D,rse]=seekingD(rInt,tT);
        DC(k1,k2)=D;
        RSE(k1,k2)=rse;
        clear D rse
        display(['completed
',num2str(counter),'/',num2str(length(rangeR)*length(rangeT))]);
    end
end

%% Output to the Screen
figure; mesh(rInt0(1:m0,2:11));
DC*1e13
RSE
```

Function 1, `seekingD.m`

```
function [DC,RSE]=seekingD(rInt,tT)

%% Diffusion Coefficient in unit of m^2/sec
D=10.^[-14.0:.5:-7.0];
for k1=1:length(D);
    c(k1)=surf_fit(tT,rInt,D(k1),0);
    close;
end
[m,n]=min(c);
if n==1 || n==length(D); DC=D(n); RSE=1976; return; end

D1=[D(n-1):(D(n+1)-D(n-1))/10:D(n+1)];
for k1=1:length(D1);
    c1(k1)=surf_fit(tT,rInt,D1(k1),0);
    close;
end
[m1,n1]=min(c1);
if n1==1 || n1==length(D1); DC=D1(n1); RSE=1977; return; end

D2=[D1(n1-1):(D1(n1+1)-D1(n1-1))/10:D1(n1+1)];
for k1=1:length(D2);
    c2(k1)=surf_fit(tT,rInt,D2(k1),0);
    close;
end
[m2,n2]=min(c2);
if n1==1 || n1==length(D1); DC=D2(n2); RSE=c2(n2); return; end

if abs((D1(n1+1)-D1(n1-1))/10)>=0.01e-13;
    D2=[D2(n2-1):(D2(n2+1)-D2(n2-1))/10:D2(n2+1)];
    for k1=1:length(D2);
        c2(k1)=surf_fit(tT,rInt,D2(k1),0);
        close;
```

```
    end
end
[m2,n2]=min(c2);

DC=D2(n2);
RSE=c2(n2);
%['D=',num2str(D2(n2)*1e13),' E-13 m^2/sec']
%['c=',num2str(c2(n2))]
%% Plotting
%figure; semilogx(D,c,'.',D1,c1,'r.',D2,c2,'k.');
%xlabel('D (m^2/sec)'); ylabel('Root Square Error');
```

Function 2, `surf_fit.m`

```
function [cc]=surf_fit(tT,rInt,D,yesplot)

%% Data processing
tT(:,1)=round(tT(:,1)*10)/10;
time=[min(tT(:,1)):0.1:max(tT(:,1))]';
[m,n]=size(rInt);
% Background correction
rInt(:,2:n)=rInt(:,2:n)-rInt(:,2)*ones(1,n-1);
maxI=max(max(rInt(:,3:n)));
L=rInt(m,1)*1e-9; %Thickness of the layer
tau=time*D/L^2;
dx1=0.1; x1=[-1:dx1:1]'; J=length(x1); x=-1*x1(1:(J+1)/2)*L;
dt1=tau(2)-tau(1); t1=tau; I=length(t1);
F=dx1^2/dt1;
%% Initial Condition
BG=fliplr(rInt(:,2)'); BG(m:2*m-1)=rInt(:,2)'; %BG=(BG-400)/(maxI-400);
rBG=-1*fliplr(rInt(:,1)'); rBG(m:2*m-1)=rInt(:,1)'; rBG=rBG/rInt(m,1);
IC=interp1(rBG,BG,x1);
clear rBG BG
%% Boundary Condition
BC=ones(I,1);
BC=interp1(tT(:,1),rInt(m,3:n)',time);
BC=BC/maxI;
%BC=(BC-400)/(maxI-400);
%% Loading Matrix
% general loading
M1=zeros(I*J,I*J);
y=zeros(I*J,1);
for k1=2:I-1
    for k2=2:J-1
        M1((k1-1)*J+k2,(k1-2)*J+k2)=-.5*F;
        M1((k1-1)*J+k2,(k1-1)*J+k2-1:(k1-1)*J+k2+1)=[-1,2,-1];
        M1((k1-1)*J+k2,k1*J+k2)=.5*F;
    end
end

% i=I,j=2:J-1
for k2=2:J-1
```

```
    M1((I-1)*J+k2,(I-3)*J+k2)=.5*F;
    M1((I-1)*J+k2,(I-2)*J+k2)=-2*F;
    M1((I-1)*J+k2,(I-1)*J+k2-1:(I-1)*J+k2+1)=[-1,2+1.5*F,-1];
end

% i=1:I, j=1 or J
for k1=1:I
    M1((k1-1)*J+1,(k1-1)*J+1)=1;
    M1((k1-1)*J+J,(k1-1)*J+J)=1;
    y((k1-1)*J+1,1)=BC(k1);
    y((k1-1)*J+J,1)=BC(k1);
end

% i=1, j=2:J-1
for k2=2:J-1
    M1(k2,k2)=1;
end
y(1:J)=IC;
%% Solving
c=inv(M1)*y;
clear M1 y k*
%% Rearrange result
for k9=1:I; c2d(k9,1:J)=c((k9-1)*J+1:(k9-1)*J+J)'; end
c1=c2d(:,1:(J+1)/2);r1=x1(1:(J+1)/2)*-1;
clear k9 c2d
%% Calculate IVD
IVD=zeros(I,1);
IVD=(c1*[0;dx1*ones((J-1)/2,1)])./BC;
BT=1-IVD;
%% Calculate error
Int=rInt(:,3:n)';
%c=abs(sum(sum(c1))*dx1*dt1-
[0,diff(tT(:,1)'*D/L^2)]*(Int/maxI)*[0,diff(rInt(:,1)'/L/1e9)]');
c2=spline(time,c1',tT(:,1))';
c3=spline(r1,c2,rInt(:,1)/rInt(m,1));
difference=(Int/maxI-c3);
difference=difference./(Int/maxI);
weights=ones(size(difference));
cc=sqrt(sum(sum((difference.*weights).^2))/(m*(n-2)));
%% Plot
if yesplot ==1
    figure;
mesh(time*ones(1,length(x)),ones(length(time),1)*x'*1e9,c1);
    hold;
mesh(tT(:,1)*ones(1,m),ones(length(tT),1)*rInt(:,1)',Int/maxI);
    xlabel('Time (sec)'); ylabel('radius (nm)'); zlabel('Intensity');
    title(['D=',num2str(D*1e13),'x10^-^1^3 m^2/sec']);
end
```

Appendix E

Finite Difference Equations for FITC Bolus Dispersion

The followings are steps of generating the difference equations from the two governing differential equations, Equation 3 and 5, in computational simulation of FITC Transport inside the glycocalyx.

1. Conservation of momentum (Eq. 3)

$$\frac{\mu}{r}\frac{\partial}{\partial r}\left(r\frac{\partial u(r)}{\partial r}\right)=\frac{\partial P}{\partial x}+k_r\cdot u(r) \qquad \text{A1}$$

Dimensionless dimension variables are defined as:

$$\bar{u}=u/U_{bulk}$$

$$\bar{r}=r/R$$

Equation A1 can then be written as:

$$\frac{\partial^2(\bar{u})}{\partial(\bar{r})^2}+\frac{1}{\bar{r}}\frac{\partial(\bar{u})}{\partial(\bar{r})}=\frac{1}{8}f\,\mathrm{Re}+\varphi\cdot\bar{u} \qquad \text{A2}$$

Three dimensionless numbers in Eq. A2 are:

(1) $f=\dfrac{\partial P}{\partial x}\dfrac{(2R)}{\frac{1}{2}\rho U_{bulk}{}^2}$, the Darcy friction factor, representing the linear relationship between the bulk velocity and the pressure drop.

(2) $\mathrm{Re}=\dfrac{(2R)\rho U_{bulk}}{\mu}$ is the Reynolds number.

(3) $\varphi = \dfrac{k_r \cdot R^2}{\mu}$ is the ratio of energy loss due to porous flow to nonporous flow.

Boundary conditions are:

(1) At the centerline

$$\mu \frac{2}{\Delta r} \frac{\partial u}{\partial r} = \frac{dP}{dx} + k_r \cdot u \qquad \text{A3}$$

In dimensionless form

$$\frac{\partial(\bar{u})}{\partial(\bar{r})} = \frac{1}{16} f \,\mathrm{Re} + \frac{1}{2} \varphi \bar{u} \qquad \text{A4}$$

(2) non-slip boundary at EC surface

$$u_{r=R} = 0 \qquad \text{A5}$$

In dimensionless form

$$\bar{u} = 0 \qquad \text{A6}$$

Rewrite equations A2, and two boundary conditions A4 and A6 into difference equations by the following transfers:

$\bar{u} = u_j$ $(0 \le \bar{u} \le \dfrac{u_{\max}}{u_{bulk}})$, where $1 \le j \le J$

$\bar{r} = j / J$ $(0 \le \bar{r} \le 1)$ and $\Delta \bar{r} = 1/J$, where $1 \le j \le J$

$\dfrac{\partial \bar{u}}{\partial \bar{r}} = \dfrac{u_{j+1} - u_{j-1}}{2\Delta \bar{r}} = \dfrac{J}{2}\left(u_{j+1} - u_{j-1}\right)$ Particularly, $\left.\dfrac{\partial \bar{u}}{\partial \bar{r}}\right|_{r=0} = J\left(u_2 - u_1\right)$.

$\dfrac{\partial^2 \bar{u}}{\partial \bar{r}^2} = \dfrac{u_{j+1} + u_{j-1} - 2u_j}{\Delta \bar{r}^2} = J^2\left(u_{j+1} + u_{j-1} - 2u_j\right)$

The difference equations of the conservation of momentum, Eq. 3, is:

$$\left(2J^2+\varphi\right)\cdot u_j = J^2\left(u_{j+1}+u_{j-1}\right)+\frac{J^2}{2j}\left(u_{j+1}-u_{j-1}\right)-\frac{1}{8}f\ \mathrm{Re} \qquad \text{A7}$$

Boundary conditions:

$$\left(2J^2+\varphi\right)u_1 = 2J^2u_2-\frac{1}{8}f\ \mathrm{Re}\ \text{ for j=1} \qquad \text{A8}$$

$$u_J = 0\ \text{ for j=J} \qquad \text{A9}$$

Equations A5 to A7 were put in implicit scheme for computation:

$$u_j = \frac{\frac{1}{\Delta r^2}\left(u_{j+1}+u_{j-1}\right)+\frac{1}{2j\Delta r^2}\left(u_{j+1}-u_{j-1}\right)-\frac{1}{\mu}\frac{dP}{dx}}{\frac{2}{\Delta r^2}+\frac{K_j}{\mu}} \qquad \text{A10}$$

At the boundary,

$$u_1 = \frac{\frac{2}{\Delta r^2}u_2-\frac{1}{\mu}\frac{dP}{dx}}{\frac{2}{\Delta r^2}+\frac{K_1}{\mu}} \qquad \text{A11}$$

$$u_J=0 \qquad \text{A12}$$

2. Conservation of Mass (Eq. 5)

$$\frac{\partial c\left(x,r,t\right)}{\partial t}+u\left(r\right)\frac{\partial c\left(x,r,t\right)}{\partial x} = D_x\frac{\partial^2\left(c\left(x,r,t\right)\right)}{\partial x^2}+\frac{1}{r}D_r\frac{\partial}{\partial r}\left(r\frac{\partial c\left(x,r,t\right)}{\partial r}\right) \qquad \text{A13}$$

The difference equation for Eq. A13 is:

$$\begin{aligned} c_{i,j}^{k+1} &= c_{i,j}^{k}-\bar{u}\left(c_{i,j}^{k}-c_{i-1,j}^{k}\right)+\overline{D}_x\left(c_{i+1,j}^{k}+c_{i-1,j}^{k}-2c_{i,j}^{k}\right) \\ &+\overline{D}_r\left(c_{i,j+1}^{k}+c_{i,j-1}^{k}-2c_{i,j}^{k}\right)+\frac{\overline{D}_r}{j}\left(c_{i,j+1}^{k}-c_{i,j}^{k}\right) \end{aligned} \qquad \text{A14}$$

Where the dimensionless parameters were defined as: $\bar{u} = \frac{u(r)}{\Delta x / \Delta t}$, $\overline{D}_x = \frac{D_x}{\Delta x^2 / \Delta t}$ and $\overline{D}_r = \frac{D_r}{\Delta r^2 / \Delta t}$.

Boundary conditions are:

(1) Centerline (r = 0, or j = 1)

$$c_{i,1}^{k+1} = c_{i,1}^{k} - \overline{u_1}\left(c_{i,1}^{k} - c_{i-1,1}^{k}\right) + \overline{D}_x\left(c_{i+1,1}^{k} + c_{i-1,1}^{k} - 2c_{i,1}^{k}\right) + 2\overline{D}_r\left(c_{i,2}^{k} - c_{i,1}^{k}\right) \qquad \text{A15}$$

(2) EC wall (r = R, or j = J)

$$c_{i,J}^{k+1} = c_{i,J}^{k} - \overline{u_J}\left(c_{i,J}^{k} - c_{i-1,J}^{k}\right) + \overline{D}_x\left(c_{i+1,J}^{k} + c_{i-1,J}^{k} - 2c_{i,J}^{k}\right) - \left(1 - \frac{\Delta r}{R_c}\right)\overline{D}_r\left(c_{i,J}^{k} - c_{i,J-1}^{k}\right)$$

A16

(3) Entrance (x = 0, or i = 1)

$$c_{1,j}^{k+1} = c_{1,j}^{k} - \overline{u_j}\left(c_{i,j}^{k} - c^{k}{}_{init}\right) + \overline{D}_x\left(c_{2,j}^{k} - c_{1,j}^{k}\right) \qquad \text{A17}$$

The initial concentration C_{init}^{k} was taken from experimental measurements.

Appendix F

Finite Difference Equations for 1-D Diffusion Model

The governing equation for 1-D diffusion model of the FITC in the glycocalyx layer is denoted by $\frac{\partial\theta}{\partial\tau}=\frac{\partial^2\theta}{\partial\eta^2}$ (Eq. 6) with dimensionless parameters defined as $\theta=\frac{c}{c_m}$, $\eta=\frac{r}{\delta}$, and $\tau=\frac{t\cdot D}{\delta^2}$, where δ refers to the thickness of the glycocalyx. The finite difference equation is

$$\theta_{i,j}=\frac{1}{2}\theta_{i,j-1}+\frac{\Delta\eta^2}{4\cdot\Delta\tau}\theta_{i-1,j}-\frac{\Delta\eta^2}{4\cdot\Delta\tau}\theta_{i+1,j}+\frac{1}{2}\theta_{i,j+1}$$

To improve accuracy and reduce the numerical error, instead modeling the diffusion process in a brinkman layer with thickness of δ, from r = 0 to δ, a layer with thickness of 2 δ was used, spanning from r = - δ to δ. The modeled layer is symmetric along the centerline r = 0. By mirroring the layer, the boundary condition at r = 0 (EC surface) was automatically guaranteed as $\partial c/\partial r=0$. Hence, the only boundary condition that needed to be specified is $\theta_\delta=c_\delta/c_m$, where both c_δ and δ_m were obtained experimentally.

Appendix G

Error Analysis for Barrier Thickness Measurement

The barrier thickness was estimated by the difference between IP and EC wall. The uncertainty in the intensity measurement was assessed by the RMS error of measured intensity of known concentrations of FITC solution in glass channels, as in the following plot. The RMS error of the intensity against the linear regression is 9.1%, which represents the accuracy of the intensity reading for any given dye concentration.

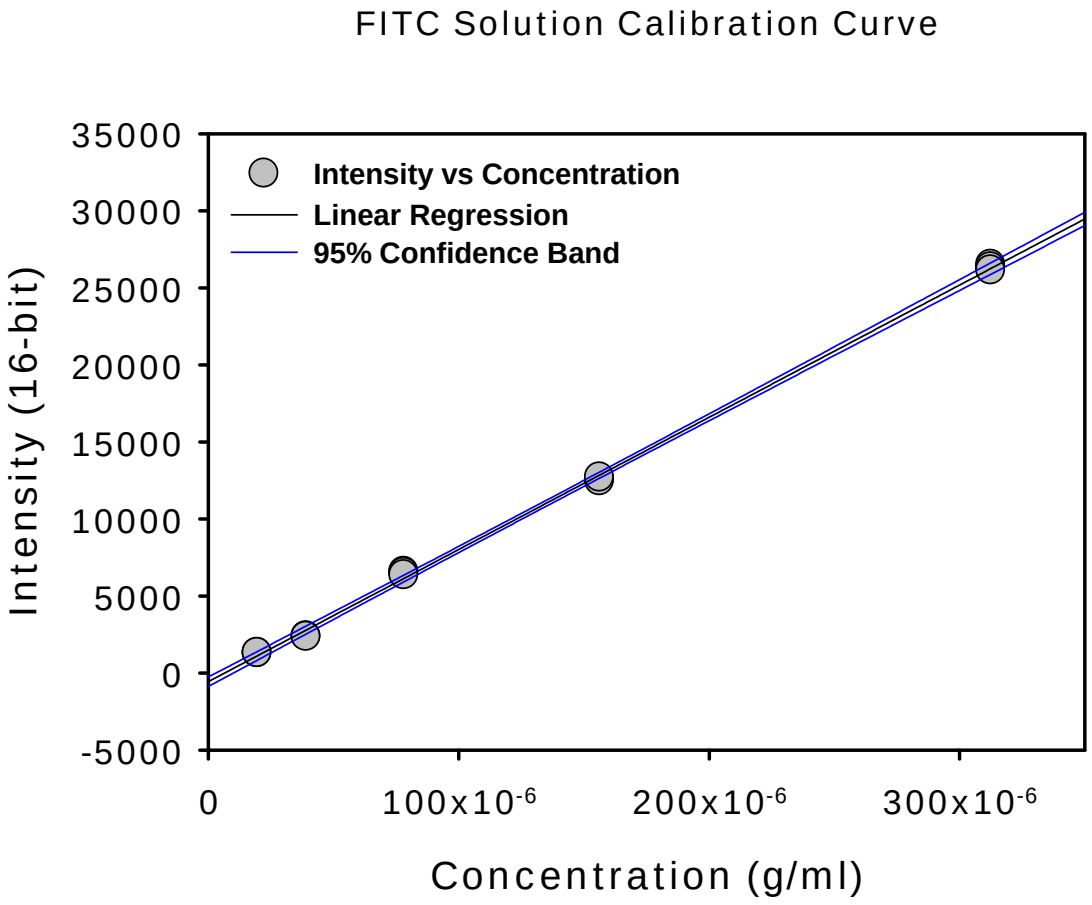

The 9.1% RMS error represents the error in the intensity measurements. Such error caused around 7 pixels in the IP determination, as shown in the following illustration. So the uncertainty of the location of IP is 7 pixels, or 404 nm.

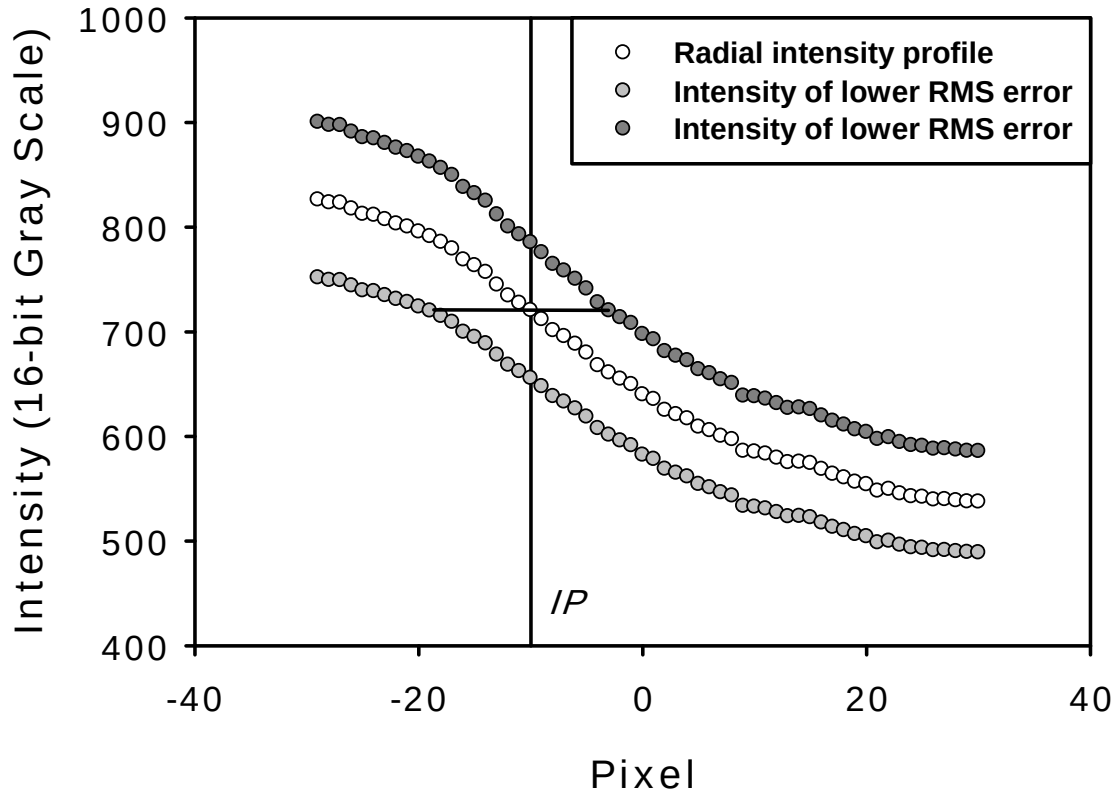

The slope at the IP of the sigmoidal curve fit is 11.1 pixel^{-1}. In other words, each unit variation in 14-bit gray scale will produce uncertainty of 0.36 pixel (20.8 nm) in IP. The uncertainty of EC wall from naked-eye observation is 1 pixel (57.7 nm). The over all 95% confidence interval for the barrier thickness is then:

$$| \delta t | = | \delta IP | + | \delta IP | + | \delta EC | = 404.0 + 20.8 + 57.7 = 482.5 \text{ nm}$$

Under control condition, this can be interpreted around 100% uncertainty.

Appendix H

Effect of Vessel Curvature on the Intensity Measurements

The following analysis is to address whether the variation in the curvature of the vessel wall has any significant impact on the measured fluorescent intensity that was used in computation of VTT, OP and IP. Intensity measured by the microscopic system is contributed by the fluorophore in the volume defined by EC wall, thickness of the glycocalyx and the depth of field, as illustrated by the blue area in the following plot. The intensity along the depth of the field exhibits a Gaussian curve where the maximum lies on the focal plane. However, even distribution was assumed in this analysis, which actually maximizes the effect of the depth of field, for simplicity.

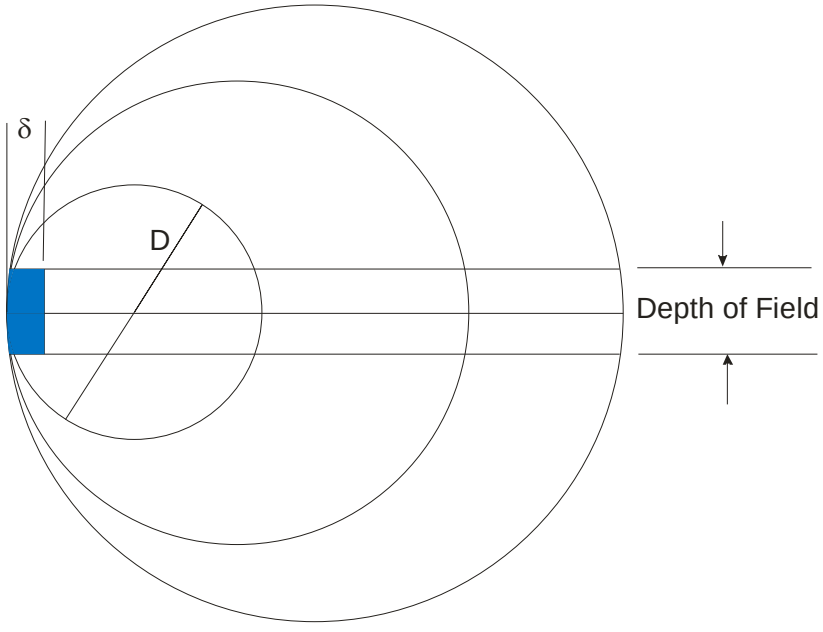

The depth of field for the Carl Zeiss 40x 0.75NA Water Immersion Objective can be estimated by $\lambda n/NA^2$, as 1.2 μm, where emission wavelength λ = 510 nm, refractive

index of water n = 1.33 and numerical aperture NA = 0.75. Two values of the glycocalyx thickness were evaluated, 500 nm and 1 μm. The range of the vessel diameter was from 10 to 60 μm. The volume of the FITC contributing to the intensity measurement was calculated and plotted against vessel diameter, as in the following plot. The volume increases with vessel diameter for both 500 nm and 1000 nm glycocalyx layer. However, such increases are trivial to induce any significant change in the volume and, in turn, the measured intensity. It is then safe to conclude that the curvature change due to the variation on the vessel diameter won't affect the fluorescent intensity measurements.

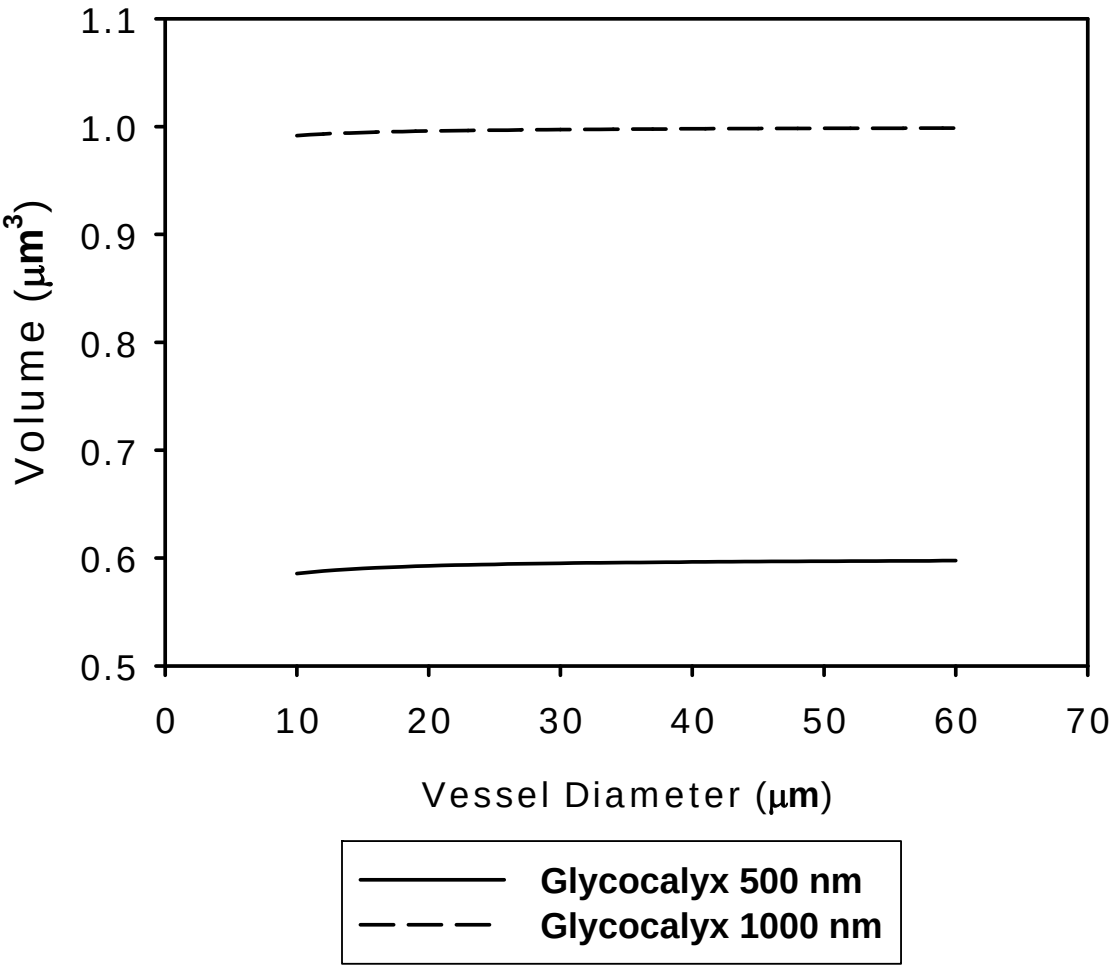

VITA

Lujia Gao

Lujia Gao was born in Shijiazhuang, Hebei Province, China, in 1976. He received his B. S. degree in Refrigeration and Cryogenics from Shanghai Jiao Tong University in 1998, and an M. S. degree in the same department in 2001. After a brief employment as a manufacturing engineer at Thermo King Transportation Refrigeration Co. Ltd., he joined the department of Mechanical Engineering at Louisiana State University and earned his M. S. degree in 2003.

He began his study in the Department of Bioengineering at the Pennsylvania State University in 2003. His initial area of focus, the venule-arteriolar pairing in diabetes, was ended immaturely after Dr. Norman Harris decided to leave the department. He then devoted his research in characterizing the barrier properties of the endothelial glycocalyx under physiological and inflammatory conditions.

He has published three papers as an author and coauthor in the field of Mechanical Engineering, and two papers as an author in the field of biomedical engineering.